Natalie Beck

1379

Band 327

Optical and electrical properties of hydrogenated amorphous and microcrystalline silicon for solar cell applications

UFO Atelier für Gestaltung & Verlag

Université de Neuchâtel

Institut de Microtechnique

Optical and electrical properties of hydrogenated amorphous and microcrystalline silicon for solar cell applications

Thése

Présentée à la Faculté de Sciences
pour obtenir le grade de docteur ès sciences
par

Natalie Beck

UFO Dissertation Band 327

Die Deutsche Bibliothek – CIP-Einheitsaufnahme

Beck, Natalie
Optical and electrical properties of hydrogenated amorphous and microcrystalline silicon for solar cell applications / Natalie Beck. – 1. Aufl. – Allensbach ; Stuttgart : UFO, Atelier für Gestaltung und Verl., 1997
(UFO-Dissertation ; Bd. 327)
Zugl.: Neuchâtel, Univ., Diss., 1997
ISBN 3-930803-26-7

Dissertation der Universität Neuchâtel
Datum der mündlichen Prüfung: 8. September 1997
Referenten: MM. A. Shah
H. Beck, P. Renaud
B. Rech
M. Vanecek, E. A. Schiff

UFO Atelier für Gestaltung & Verlag GbR
Allensbach
Maus Druck & Medien GmbH, Konstanz
Erste Auflage 1997
Alle Rechte beim Autor
ISBN 3-930803-26-7

IMPRIMATUR POUR LA THÈSE

Propriétés optiques et électriques du silicium amorphe et microcrystallin hydrogéné pour des applications photovoltaïques

de Mme Nathalie Beck

UNIVERSITÉ DE NEUCHÂTEL

FACULTÉ DES SCIENCES

La Faculté des sciences de l'Université de Neuchâtel sur le rapport des membres du jury,

MM. A. Shah (directeur de thèse),
H. Beck, P. Renaud (EPF Lausanne), B. Rech (Jülich),
M. Vanecek (Prague) et E.A. Schiff (Syracuse)

autorise l'impression de la présente thèse.

Neuchâtel, le 24 novembre 1997

Le doyen:

F. Stoeckli

TABLE OF CONTENTS

INTRODUCTION I

Outline of this work 2

1. TRANSPORT MEASUREMENT TECHNIQUES FOR a-Si:H 5

1.1. Relevant transport parameters for p-i-n solar cells 5

1.2. The standard model of density of states (DOS) for a-Si:H 7

1.3. Transport model for a-Si:H 8

1.3.1. The basic transport equations 8
1.3.2. a-Si:H in thermal equilibrium 9
1.3.3. a-Si:H under moderate steady-state illumination 11

1.4. The Time of Flight technique 12
1.4.1 The Time of Flight experiment 12
1.4.2. The mobility-lifetime products deduced from TOF 15

1.5. The steady-state photoconductivity and the steady-state photocarrier grating technique 16

1.6. The $\mu\tau$ problem 19
1.6.1. Experimental 19
1.6.2. Steady-state and transient $\mu\tau$ products in micro-doped a-Si:H 20
1.6.3. How important is thermal emission from dangling bonds? 20
1.6.4. Solving the $\mu\tau$ problem 22

2. $\mu^o\tau^o$ PRODUCTS - A TOOL FOR CORRELATING a-Si:H FILM PROPERTIES AND SOLAR CELL PERFORMANCES 23

2.1. $\mu^o\tau^o$ products as a correlation parameter 23

2.2. The evaluation of the product $\mu^o\tau^o$ from SSPC and SSPG measurements 25
2.2.1. Evaluation of $\mu^o\tau^o$ products: from transient or steady-state measurements? 25
2.2.2. Evaluation procedure for $\mu^o\tau^o$ 26
2.2.3. Estimation of the ratio of the capture cross sections 29
2.2.4. The role of $\mu^o\tau^o$ products in a-Si:H solar cells 33
2.2.5. Validity of the method and its limitations 33

2.3. Correlation between $\mu^o\tau^o$ of a-Si:H layers and solar cell performances 34
2.3.1. Experiment 34
2.3.2. The annealed state 35
2.3.3. The light soaked state 38
2.3.4. Correlation between layer properties and cell performances 38

2.4. Conclusions 40

3. THIN FILM MICROCRYSTALLINE SILICON: A SHORT INTRODUCTION 41

3.1. Properties of hydrogenated microcrystalline silicon 42

3.2. Microcrystalline silicon for solar cell applications 44

4. OPTICAL PROPERTIES OF HYDROGENATED MICROCRYSTALLINE SILICON 46

4.1. Optical absorption measurement techniques 47
4.1.1. Transmission and Reflection measurements (T/R) 47
4.1.2. Photothermal Deflection Spectroscopy (PDS) 48
4.1.3. The Constant Photocurrent Method (CPM) 48

4.2. The optical absorption in µc-Si:H 50
4.2.1. "Optical tuning" of µc-Si:H 51
4.2.2. Defect-connected absorption 53
4.2.3. Red shift of the indirect optical gap 54

4.3. Scattering effects in µc-Si:H 56
4.3.1. Diffuse reflection from µc-Si:H layers with rough surface 58
4.3.2. Scattering measured by CPM 61
4.3.3. Scattering measured by specular and diffuse T/R 64

4.4. Conclusions and outlook 67

5. ELECTRICAL PROPERTIES OF HYDROGENATED MICROCRYSTALLINE SILICON 69

5.1. Introduction 69

5.2. The dark conductivity of µc-Si:H 70
5.2.1. The grain boundary trapping model 73
5.2.2. Critical reflections about the grain boundary trapping model 75

5.3. Time of Flight measurements on µc-Si:H 77
5.3.1. Particularities of the TOF method applied to µc-Si:H 77
5.3.2. Drift mobilities in µc-Si:H 83
5.3.3. mt products in µc-Si:H from charge collection measurements 88
5.3.4. Density of states in µc-Si:H from post-transient TOF 91

5.5. Conclusions 93

FINAL CONCLUSION 95

ACKNOWLEDGEMENTS 96

REFERENCES 97

INTRODUCTION

Amorphous silicon was discovered "accidently" in the sixties by Chittik [Chittik 69]. Since that time, the two most important steps in the development of amorphous silicon towards an attractive thin film material for devices were the hydrogenation (passivation of dangling bonds) [LeComber 70] and the successful n-type (phosphine) and p-type (boron) doping [Spear 75]. Nowadays, the main application fields of hydrogenated amorphous silicon (a-Si:H) are thin film transistors (TFT) and low-cost (compared to crystalline silicon) thin film solar cells.

In the present work we will concentrate, however, on the application of a-Si:H to p-i-n solar cells. To further improve the performances of a-Si:H based solar cells, two approaches must be followed up simultaneously. First, each step in the production process of a p-i-n device (doped layers, thicknesses, interfaces, etc.) must be carefully optimised in order to minimise the related "structural" losses. Secondly, the quality of the photovoltaically active material itself, the intrinsic <i> layer in the cell, must be improved. Thereby, the standard way followed by most researchers during more than one decade was the careful study of optical and electrical properties of a-Si:H in the configuration of thin layers on glass. One of the main scopes was thereby the understanding of the degradation of material properties when exposed to prolonged illumination (Staebler-Wronski effect [Staebler 77]). However, the extensive knowledge about the physics of a-Si:H gained through this research in the field of material characterisation has, so far, not really succeeded in improving a-Si:H-based solar cells. On the contrary, a lack of correlation between the characteristics measured on a-Si:H films and the performances of solar cells made of these materials persisted [Lechner 89], [Wronski 93], [Schropp 93], [Yang 94].

It was, thus, the aim of the present thesis is to build a bridge between these two fields of research: from the material characterisation of layers on one side to the incorporation of these materials into solar cell devices on the other side. In other terms, we wanted to create a suitable **tool** for people working in technology to determine the quality of the a-Si:H material they produce. Thereby, this tool must not only allow to predict accurately, on the basis of material characterisation on layers, the highest solar cell performances which can be achieved using a certain material in a solar cell. In addition, it must also be "easy to use" and have a transparent physical meaning. The parameter satisfying these conditions and which will be introduced and developed in this work, is the $\mu^o\tau^o$ product.

In parallel to these efforts in the domain of a-Si:H towards higher and mainly more stable solar cells, a new silicon material appeared in the field of thin film solar cells: **hydrogenated microcrystalline silicon** (μc-Si:H). This heterogeneous material consists of small

crystallites (~200 Å) embedded in a more or less important amorphous matrix. Already discovered in 1968 by Vepřek et al. [Vepřek 68], µc-Si:H has not been considered to be of interest for thin film solar cells for many years. Only in 1990 Wang and Lucovsky [Wang 90] presented the first µc-Si:H-based solar cell. Some years later, the boom of µc-Si:H solar cells was initiated by a µc-Si:H solar cell with a stable efficiency of 3.8% [Flückiger 93]. Since that time the efficiency of µc-Si:H cells as well as the interest in this material steadily increased. Thereby, the probably most striking property of µc-Si:H accounting for its success is the stability against light-soaking and its extended optical absorption to the infrared.

Nowadays, µc-Si:H-based solar cells and µc-Si:H / a-Si:H stacked tandem cells work very well with efficiencies of 7.7% [Meier 96] and stabilised 10.4%, respectively [Keppner 96]. However, only very little is known so far about the physical processes which govern the optical and electrical properties of this material. In view of the actuality of this subject, we also included the characterisation of µc-Si:H to our work.

Outline of this work

We separated this works in five parts, where the first two will exclusively deal with a-Si:H and its characterisation for solar cell applications. In the third, fourth and fifth section we will present first approaches and results in the characterisation of µc-Si:H.

First section

We will introduce all the utilities necessary for the construction of a "correlation tool" for solar cells. Thereby, we will first start, yet without going to details, with the parameters which govern the collection in a p-i-n solar cell device. We then will pass on to the model for a-Si:H and have a look at the transport measurement techniques available for layer characterisation. We will select three of them which allow the determination of a mobility-lifetime product: the Time of Flight technique (TOF), the steady-state photoconductivity (SSPC) and the steady-state photocarrier grating (SSPG). Analysing them we will mainly focus on the exact physical meaning of the obtained results and their potential to be used as a relevant parameter to describe the performance of a p-i-n solar cell.

Finally, we will show how the so-called "$\mu\tau$-problem" can be solved. This problem has persisted for many years in the community of researchers in a-Si:H and describes the contradictory results of mobility-lifetime products obtained by the steady-state measurements and by the transient TOF technique.

Second section

Based on the arguments brought up in the previous section, we will now concentrate on the steady-state techniques SSPC and SSPG. The $\mu\tau$-products deduced from these measurements

are a function of the prevailing dangling bond occupation in the film and, thus, are **not** a measure of material quality. We will introduce the product $\mu^o\tau^o$, which is independent of dangling bond charge and which monitors material quality in terms of band mobility μ^o and capture time τ^o, the latter being, in its turn, inversely proportional to dangling bond density. We will develop a simple evaluation procedure to deduce $\mu^o\tau^o$ from simultaneously performed SSPC and SSPG measurements. The validity as well as the limits of the method will also be discussed.

We will then apply our method first to different series of a-Si:H layers and thereafter to two series of undoped a-Si:H layers of variable quality, the latter being modified by changing the deposition temperature and by degrading the material. We thereby compare the $\mu^o\tau^o$ products evaluated on these films with the performances of standard p-i-n solar cells which incorporate the "same" undoped material as an active, intrinsic <i> layer.

Third section

In this section a brief introduction to thin film polycrystalline silicon materials in general and to hydrogenated microcrystalline silicon (µc-Si:H) produced by the Very High Frequency Glow Discharge (VHF-GD) in particular will be given. We will relate the problems which prevented the development of µc-Si:H solar cells over more than two decades and explain the main reasons why µc-Si:H material produced by the VHF-GD became nowadays a promising candidate for µc-Si:H thin film solar cell applications.

Fourth section

The µc-Si:H materials prepared by the VHF-GD have been shown to have a remarkably high optical absorption which even exceeds that of crystalline silicon over the whole spectral range. As such high absorption is rather unusual and strongly favourable for thin film solar cell applications we will focus in this section on the **optical properties** of µc-Si:H in order to understand more about the physical processes which determine the absorption behaviour in our VHF-GD µc-Si:H material.

We will measure the optical absorption by the Constant Photocurrent Method (CPM), the Photothermal Deflection Spectroscopy (PDS) and by Transmission/Reflection (T/R) measurements on different VHF-GD µc-Si:H materials. We will thereby point out that the optical absorption is not only enhanced, but that the absorption edge (given by the crystalline phase in the material) is also shifted to the infrared by about 0.1 eV. Furthermore, we will demonstrate that the very low defect-connected absorption observed in VHF-GD µc-Si:H is due to an excellent passivation of the grain boundary defects.

Due to the heterogeneity and to the rough growth surface of µc-Si:H layers scattering effect will have to be taken into consideration as they can enhance the measured apparent absorption and, thus, mask the "true" optical absorption given by the µc-Si:H material properties (band

structure, bandgap etc.). To determine the scattering coefficient in our VHF-GD µc-Si:H material we will develop and apply different experimental techniques which will allow us to show that scattering in µc-Si:H is indeed clearly enhanced compared to a-Si:H and that both, bulk and surface scattering can be present.

Different possible explanations for the observed enhanced optical absorption in the region of visible light and the red-shifted absorption edge will be given and discussed. However, some open questions will remain here.

Fifth section

In the last section of this thesis work we will approach the problem of the **electrical transport** in µc-Si:H. On one side, the excellent carrier collection even in several micron thick solar cells proofs that the carrier transport in µc-Si:H is good, on the other side a more precise concept of the electrical transport in µc-Si:H is still lacking.

We will study the electrical transport in µc-Si:H in the dark, starting with dark conductivity measurements which will serve as a monitor of the impurity contamination in our µc-Si:H materials. For the first time we will then apply the Time of Flight (TOF) technique to µc-Si:H layers and cells; this technique allows the measurement of electron and hole transport individually in the direction parallel to growth. First results obtained by TOF show a concentration of the electric field in a µc-Si:H pin cell to a small region around the grain boundaries only. Furthermore, we will determine the drift mobilities and mobility-lifetime products of electrons and holes and the "gap" of µc-Si:H will be "scanned" for deep traps by the posttransient TOF technique.

1. TRANSPORT MEASUREMENT TECHNIQUES FOR a-Si:H

A short introduction to the operation of a p-i-n solar cell and to model used to describe a-Si:H material will be given. Then we will present an analysis of three selected transport measurement techniques used in this work: the Time of Flight technique, the steady-state photoconductivity and the steady-state photocarrier grating. Finally, we will use our reflections about these measurement techniques to outline a solution of the so-called "$\mu\tau$-problem" (discrepancy between the $\mu\tau$ products deduced from transient and steady-state transport measurements).

1.1. Relevant transport parameters for p-i-n solar cells

The structure of a p-i-n solar cell is schematically drawn in fig. 1.1: the thin n- and p-type doped layers on both sides of the cell build up the internal field in the cell and act as collecting contacts, whereas the thick, undoped i-layer has the task to absorb the sunlight. Thereby the denomination p-i-n also represents the sequence of the layer deposition, here starting with the p-layer. As a p-i-n cell is illuminated through the glass, the front-contact is formed by a transparent conductive oxide (TCO) layer whereas the back contact is made of TCO (zinc oxide or ITO) plus silver in order to reflect back to the cell the fraction of sunlight not absorbed. The TCO contact is textured to improve the light scattering within the solar cell.

The basic operation mechanism of such a p-i-n cell is the following: if a photon from sunlight is absorbed in the intrinsic layer, a free electron and a free hole are created. They are separated by the internal field and travel to the n-side and p-side respectively, where they are collected by the doped layers and give rise to a current in the external circuit. The "motor" for the carrier transport is the electric field which ideally extends through the whole intrinsic layer and which transports the photogenerated electrons and holes by drift in opposite directions towards the collecting contacts.

For a good performance of such p-i-n device, different requirements must be fulfilled by the semiconducting material or by a-Si:H in particular. On one side, optical properties of the material must correspond to the application, e.g. the yield of the solar spectrum must be maximised. However, this optical part of the problem will not be addressed in this work. We will rather concentrate ourselves on the processes which take place **after** the generation of carriers by light, namely the transport of these carriers by drift (or to a much lesser extent by diffusion) through the thick intrinsic layer and their possible loss by recombination. The corresponding parameters which are involved are the **mobility** μ (representing the speed of an electron or hole in a given electric field) and the **recombination time** τ (representing the time

during which a free carrier is "travelling" before being lost by recombination). A precise definition of these quantities and related parameters will be given in chapter 1.3 to 1.5.

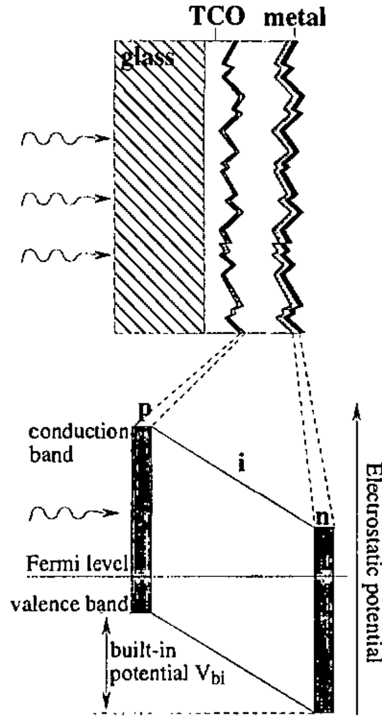

Fig. 1.1. Sketch of the structure of an a-Si:H p-i-n solar cell. The bottom part of the figure shows the ideal band diagram of such a device.

It is today still problematic to measure experimentally characteristic mobilities and times individually. Experimentally, it is more convenient to access the product of μ and τ, the **$\mu\tau$ product**, which describes the "transport & loss" mechanism without resolving between the two contributions "transport" and "loss". A simple picture of the physical meaning of the $\mu\tau$ product is the following (fig. 1.2): for a given electric field E, the $\mu\tau$ product represents the distance which is covered by an electron or hole before being lost by recombination. This distance d is called "Schubweg" and is given by:

$$d = \mu\tau \cdot E \tag{1.1}$$

Coming back to the operation of a p-i-n solar cell, this characteristic distance can directly be related to the maximal possible thickness of the i-layer (taking into account the built-in potential

in the cell) which still allows an accurate collection of the photogenerated carriers. Therefore, it is known also as a "collection length".

Even though conceptually simple, the measurement and interpretation of $\mu\tau$ products in practice is more complicated, as it will be shown in the following (ch. 1.4. 1.5, 1.6).

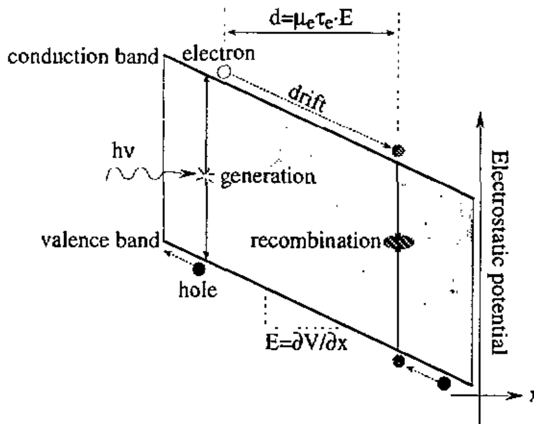

Fig. 1.2. Schematical picture illustrating the physical meaning of $\mu\tau$ products: photogenerated carriers drift over a distance d (for a given electric field E) before they are lost by recombination with a carrier of opposite sign.

1.2. The standard model of density of states (DOS) for a-Si:H

One characteristic of amorphous silicon is the continues density of states in the "gap". This is in sharp contrast with crystalline silicon (c-Si), where the gap is populated only by a certain number of more or less discrete states due to defects and impurities. As drawn in figure 1.3 there are three main types of gap states which are generally considered in the model of a-Si:H: the conduction and valance bandtails, the dangling bonds and acceptor and/or donor states.

It has been shown by several authors (i.e. [Anderson 58], [Mott 79]), that one consequence of the disorder in amorphous material are the presence of localised states in the gap, which give rise to **bandtail states** extending into the gap from the conduction and valence band edge. In the same context, the concept of the mobility edge [Mott 79] was introduced: it separates localised states in the mobility gap with $\mu = 0$ (at $T = 0$ K) from non-localised states in the bands ($\mu \neq 0$).

Another consequence of the disorder in a material like a-Si:H, are silicon-silicon covalent bonds which are distorted or even broken. These broken bonds create additional states in the

gaps, the **dangling bond states**. Even though most of these dangling bonds can be passivated by hydrogen, the remaining ones act as efficient recombination centres, as it will be extensively discussed in the following. Dangling bonds can either be empty (positively charged D^+), occupied by one electron (neutral D^o) or by two electrons of opposite spin (negatively charged D^-). The necessary energy to populate a singly occupied dangling bond by a second electron of opposite spin is called correlation energy U.

Finally, a-Si:H can be doped, introducing additional **donor and acceptor states** near the conduction band and valence band respectively.

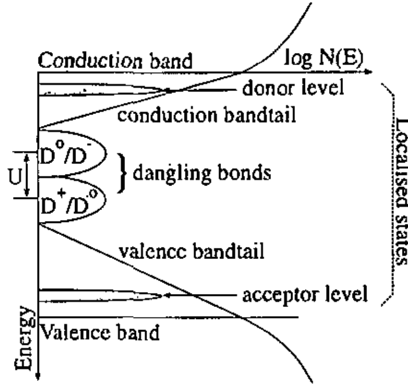

Fig. 1.3. a-Si:H is characterised by an important density of states in the gap. The three main types of states which are considered in the model of a-Si:H are bandtail states, dangling bonds and eventual acceptor or donor levels.

1.3. Transport model for a-Si:H

1.3.1. The basic transport equations

The free carrier transport in a-Si:H can be described by the five basic transport equations: the Poisson equation, two equations for the electron and hole current densities and the two continuity equations:

$$\frac{dE(x)}{dx} = \frac{e}{\varepsilon_{Si}} \cdot \left(p_f(x) - n_f(x) + Q_{loc}(x)\right) \tag{1.2}$$

$$\frac{1}{e} \cdot j_n(x) = \mu_n^0 n_f(x) E(x) + D_n^0 \frac{dn_f(x)}{dx} \tag{1.3}$$

$$\frac{1}{e} \cdot j_p(x) = \mu_p^0 p_f(x) E(x) - D_p^0 \frac{dp_f(x)}{dx} \tag{1.4}$$

$$0 = G_n(x) - R_n(x) + \frac{1}{e} \cdot \frac{d}{dx} j_n(x) \qquad (1.5)$$

$$0 = G_p(x) - R_p(x) - \frac{1}{e} \cdot \frac{d}{dx} j_p(x) \qquad (1.6)$$

The Poisson equation (1.2) relates the derivative of the electric field to the total local charge, the latter being constituted by the free carriers $n_f(x)$ and $p_f(x)$ on one side and by localised charges on the other side. The total localised charge $Q_{loc}(x)$, generally dominant in a-Si:H, is composed of trapped carriers, charged dangling bonds and eventual ionised dopants.

The two equations (1.3) (for electrons) and (1.4) (for holes) express the current densities, combining the contributions of the two driving forces of transport, **drift** and **diffusion**. Thereby, μ_n^o and μ_p^o are the band mobilities of electrons and holes and D_n and D_p are the diffusion constants given by Einstein relation:

$$D_n^0 = \frac{kT}{e} \cdot \mu_n^0 \qquad D_p^0 = \frac{kT}{e} \cdot \mu_p^0 \qquad (1.7)$$

The continuity equations (1.5) and (1.6) explicit the conservation of charge in the material. G(x) represents thereby all generation processes of free carriers (absorption of light, thermal emission from localised states) whereas R(x) is the recombination term, taking into account all possible loss mechanisms of free carriers (trapping and recombination).

1.3.2. a-Si:H in thermal equilibrium

In thermal equilibrium where no carriers are photogenerated nor injected, the continuity equations (1.5) and (1.6) reduce to R(x) = G(x), and the generation term is due to thermal emissions from localised states only. The possible transitions in thermal equilibrium are shown in fig. 1.4.

To evaluate the occupation function of the dangling bonds in thermal equilibrium we apply the principle of detailed balance where each dangling bond state is in equilibrium with the band states: $r_{cn}^+ = r_{en}^o$, $r_{cn}^o = r_{en}^-$, $r_{cp}^o = r_{ep}^+$, $r_{cp}^- = r_{ep}^o$. As a result one obtains [Vaillant 86]:

$$f_o^+ = \frac{exp[(E_D - E_F)/kT]}{2 + exp[(E_D - E_F)/kT] + exp[(E_F - E_D - U)/kT]} \qquad (1.8)$$

$$f_o^- = \frac{exp[(E_F - E_D - U)/kT]}{2 + exp[(E_D - E_F)/kT] + exp[(E_F - E_D - U)/kT]} \qquad (1.9)$$

$$f_o^0 = \frac{2}{2 + exp[(E_D - E_F)/kT] + exp[(E_F - E_D - U)/kT]} \qquad (1.10)$$

where the subscript o denominates thermal equilibrium values. The variation of f_o^0, f_o^+ and f_o^- with the Fermi level position E_F according to these expressions is represented in fig. 1.5.

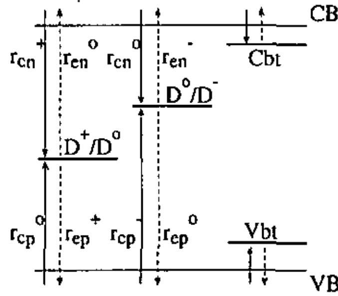

Fig. 1.4. Allowed transitions in thermal equilibrium between localised states and conduction- and valence bands respectively. The transitions from the valence bandtail (Vbt) to the conduction band (CB) and from the conduction bandtail (Cbt) to the valence band (VB) are not shown here, as they have small probabilities to occur. Full arrows represent trapping of free carriers on localised states, dashed arrows the thermal emissions from the latter. The energetical distribution of the localised states is replaced in this representation for the sake of simplicity, hy discrete levels.

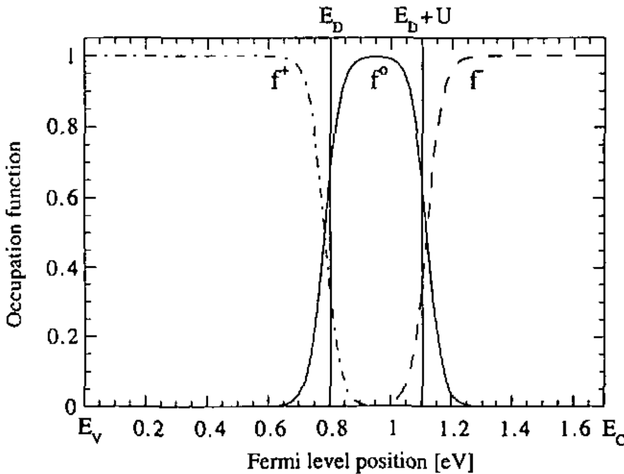

Fig. 1.5. Calculated dangling bond occupations as a function of the Fermi level position. For the evaluation, the dangling bonds were assumed to be discrete levels at energy positions $E_{D+/Do}$ = 0.8 eV and $E_{Do/D-}$ = 1.1 eV (U = 0.3 eV) above the valence band edge.

1.3.3. a-Si:H under moderate steady-state illumination

If the a-Si:H is continuously illuminated, the material reaches a new steady-state equilibrium and the photogeneration adds a generation term in the continuity equations (1.5) and (1.6). Furthermore, the Fermi level E_F splits in two quasi-Fermi levels E_{Fn} and E_{Fp}. These levels were introduced to describe the free carrier density under illumination in analogy to the thermal equilibrium:

$$n_f = N_C\, exp\left(-\frac{(E_C - E_{Fn})}{kT}\right) \tag{1.11}$$

$$p_f = N_V\, exp\left(-\frac{(E_{Fp} - E_V)}{kT}\right) \tag{1.12}$$

When free carrier recombination through bandtails is neglected, these quasi-Fermi levels become identical with the demarcation levels E_{tn} and E_{tp} introduced by Taylor and Simmons [Taylor 1972]. The latter are defined as being the energy levels where recombination (to these levels) and thermal emission (from these levels) are equally probable; E_{tn} and E_{tp} thus separate the trap states from deep states which act as recombination centres. The transitions between extended and localised states under illumination are represented in fig. 1.6.

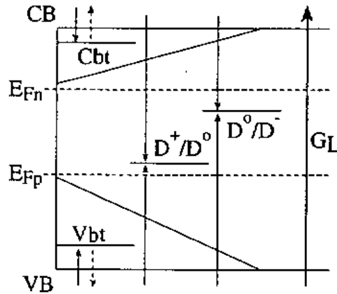

Fig. 1.6. Model of the transitions in a-Si:H in steady-state equilibrium where the photogeneration (G_L) becomes the dominant creation mechanism of free carriers. The quasi-Fermi level thereby separates shallow trap states from recombination centres: the conduction bandtail states (Cbt) and valence bandtail states (Vbt) act as traps, the dangling bonds are mainly recombination centres. The localised states are represented again as discrete energy levels.

For our further analysis, we will consider a-Si:H material under steady-state illumination which is high enough (but not too high) for that thermal emissions from dangling bonds and recombination by bandtail states can be neglected (see fig. 1.6). This means that almost all

dangling bonds are comprised within the two quasi-Fermi levels E_{Fn} and E_{Fp}. In this domain, the model of monomolecular recombination through dangling bonds ([Vaillant 86], [Hubin 92]) is a valid approximation. In this model free carriers only recombine through the dangling bond states and the corresponding characteristic recombination times τ_n^R and τ_p^R then simply become:

$$\tau_n^R = \frac{1}{v_{th} N_{db} \sigma_n^0 f^0 + v_{th} N_{db} \sigma_n^+ f^+} \tag{1.13}$$

$$\tau_p^R = \frac{1}{v_{th} N_{db} \sigma_p^0 f^0 + v_{th} N_{db} \sigma_p^- f^-} \tag{1.14}$$

where f^+, f^- and f^0 are the dangling bond occupation functions under illumination.

Consequently, the charge state of dangling bonds will be governed exclusively by the recombination kinetics of electrons and holes. This fact is directly reflected in the occupation functions of the dangling bonds which depend on the free carrier densities n_f and p_f only ([Vaillant 86], [Hubin 92]):

$$f^+ = \frac{(p_f/n_f)(\sigma_p^o/\sigma_n^+)}{(p_f/n_f)(\sigma_p^o/\sigma_n^+) + 1 + (n_f/p_f)(\sigma_n^o/\sigma_p^-)} \tag{1.15}$$

$$f^- = \frac{(n_f/p_f)(\sigma_n^o/\sigma_p^-)}{(p_f/n_f)(\sigma_p^o/\sigma_n^+) + 1 + (n_f/p_f)(\sigma_n^o/\sigma_p^-)} \tag{1.16}$$

$$f^0 = \frac{1}{(p_f/n_f)(\sigma_p^o/\sigma_n^+) + 1 + (n_f/p_f)(\sigma_n^o/\sigma_p^-)} \tag{1.17}$$

1.4. The Time of Flight technique

1.4.1 The Time of Flight experiment

The transient Time of Flight (TOF) technique was introduced for a-Si:H by Spear [Spear 69]. It monitors the transit of a package of excess carriers though the film in direction of growth (sandwich configuration) and allows the separate determination of the mobility-lifetime products of electrons and holes. Thereby, the type of carrier to be measured can be selected simply by changing the polarity of the applied voltage.

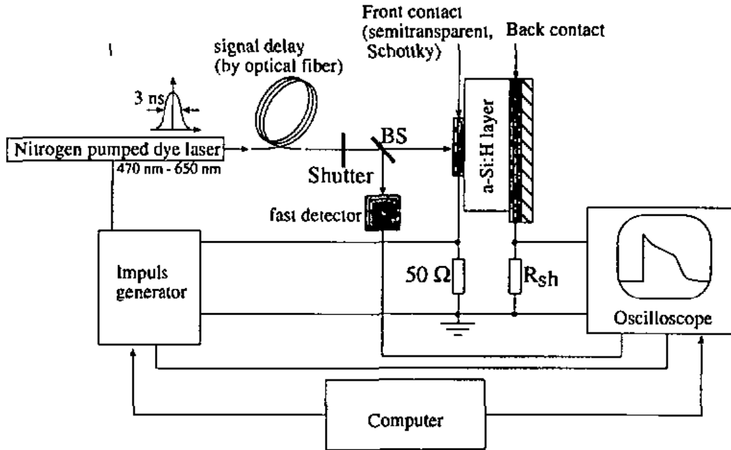

Fig. 1.7. Set-up of the Time-of-Flight experiment. The shunt resistor R_{sh} is chosen 50 Ω for the measurements in current mode. The light pulse is delayed by a 200 m long optical fibre in order to get rid of the electrical noise from pulse generation. For details refer to [Wyrsch 92].

The principle of the measurement is the following (see fig. 1.7): a "sheet" of charges Q_o (electrons & holes) is created at time 0, by a strongly absorbed and extremely short (3 ns) light pulse, close to the surface of the sample. By the effect of an external applied field, the charges are separated: one type of carrier is immediately collected by the nearby top contact whereas the carrier with opposite sign travels across the sample thickness, giving rise to a displacement current in the external circuit. When this carrier package reaches the opposite back contact, the carriers are extracted and the observed current drops down. The time needed by the carriers to cross the sample is called transit time (t_T) and allows the determination of the drift mobility μ_D. The latter is given by (where d is the sample thickness):

$$\mu_D = \frac{d}{t_T E} \tag{1.18}$$

and reflects the drift velocity v of the photogenerated carrier package in a given electric field E ($v = \mu_D \cdot E$), including shallow trapping events (see also fig. 1.8).

By integration of the current transient, one obtains the total collected charge and thereby an information about the carrier losses during transit. Increasing the applied voltage the transit time t_T becomes shorter and the probability for free carriers to fall into deep traps is reduced. The collected charge will, thus, increase with the applied voltage and finally reach a saturation value Q_o given the total photogenerated charge. The shape of this collection curve, described by Hecht's formula [Hecht 32], depends on the carrier mobility-lifetime

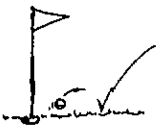

product $\mu\tau$ (assumed to be constant during transit):

$$Q = \frac{Q_0}{d}\mu\tau E \cdot \left[1 - exp\left(-\frac{d}{\mu\tau E}\right)\right] \quad (1.19)$$

To deduce the $\mu\tau$ product for electrons and holes the carrier collection curves are measured individually and subsequently fitted by equation 1.19.

A more complete expression, taking into account a (constant) internal electrical field (in p-i-n cells or close to Schottky contacts), improves the fitting of experimental curves at low applied voltages [Karg 86]:

$$Q = \frac{Q_0}{d}\mu\tau \cdot \left[(E + E_i)\cdot\left(1 - exp\left(-\frac{d_i}{\mu\tau(E+E_i)}\right)\right) + E \cdot exp\left(-\frac{d_i}{\mu\tau(E+E_i)}\right)\cdot\left(1 - exp\left(\frac{d_i - d}{\mu\tau E}\right)\right)\right]$$

where d_i denotes the zone in the sample with internal field and E_i the internal field strength. We will use this expression for the evaluation of $\mu\tau$ products (assumed constant over the whole thickness).

Even though the principle of the TOF measurement is conceptually straightforward, on the practical level there exist a number of different modes and additional conditions which need to be considered. Without going in the detail, let us mention here the most important ones.

The transit and dielectrical relaxation time

The applied electric field must be constant and uniform during the whole TOF experiment. However, as a-Si:H material is slightly conductive, it relaxes and the applied field is screened within a time τ_{diel}, the dielectrical relaxation time, which is given by the dielectric constant ε_{Si} and the conductivity of the material σ_d. In order to assure a correct measurement of the transit time τ_T, the voltage must be applied to the sample only very short time before the light pulse and τ_T must be clearly shorter than τ_{diel}:

$$t_T < \tau_{diel} = \frac{\varepsilon_{Si}}{\sigma_d} \quad (1.21)$$

The current and integral mode

TOF measurements can be performed either in current mode or in integral mode. In the standard current mode, the RC constant of the external circuit is short and the charge on the sample capacitor is constantly replenished: the charge on the C_{sample} is constant during the whole experiment. In the integral mode, the RC constant of the external circuit is high (i.e. high shunt resistor) and the detected signal is the accumulation of charge on the sample capacitor.

Small signal and SCLC mode

In the classical TOF experiment (small signal TOF) the photogenerated charge is much smaller than the charge on the electrodes of the sample. This guarantees that the electrical field in the sample is not distorted by the moving charges; this is a necessary condition for the evaluation by Hecht's formula. However, TOF measurements may also be performed in the Space Charge Limited Current mode (SCLC) [Kočka 91-1] where the photogenerated charge is comparable or higher than the charge on the sample capacitor. In this case, the internal electric field is strongly screened by the photogenerated charges and the carriers are extracted in small portions. The advantages of the SCLC mode are high signal amplitudes and a longer residual time of carriers in the sample (enhancing thus loss processes), but on the other side the interpretation of the results is less straight forward.

Post transient TOF

Whereas the short-time TOF experiment monitors the transit of the photogenerated carrier package through the layer, the extension of the TOF experiment to a much longer time scale (up to seconds) can give information about the density of states in the gap. Thereby, electrons and holes which were deep-trapped during transit are thermally reemitted at longer times and their collection becomes a direct fingerprint of the DOS ([Seynhave 89], [Kočka 94]).

All TOF measurements on a-Si:H presented in this work were performed by small signal TOF in current mode at room temperature. Some particularities appeared, however, when applying the TOF technique to μc-Si:H as will be discussed in section 5.

1.4.2. The mobility-lifetime products deduced from TOF

The photogenerated carriers travel through the a-Si:H material at room temperature by a multiple trapping process ([Tiedje 81], [Orenstein 81]) and is finally either collected by the opposite contact or lost by deep trapping on a defect (see fig. 1.8). If we assume that deep traps are mainly dangling bonds and that no thermal emissions from these defects occur during transit, the evaluated $\mu\tau$ product is a drift mobility × deep-trapping time product ($\mu^D\tau^D$) which can be identified with the **band mobility × free carrier deep-trapping time product** $\mu^o\tau$ [Kočka 91-2]. The free carrier deep-trapping times are then of the form:

$$\tau_n = \frac{1}{v_{th}N_{db}\sigma_n^0 f_o^0 + v_{th}N_{db}\sigma_n^+ f_o^+} \tag{1.22}$$

$$\tau_p = \frac{1}{v_{th}N_{db}\sigma_p^0 f_o^0 + v_{th}N_{db}\sigma_p^- f_o^-} \tag{1.23}$$

where f_o^0, f_o^+, f_o^- are the dangling bond occupations at thermal equilibrium, v_{th} is the thermal velocity (assumed to be equal for both types of carriers), N_{db} the deep defect density and σ_n^o, σ_p^o, σ_n^+, σ_p^- are the capture cross-sections of the dangling bonds.

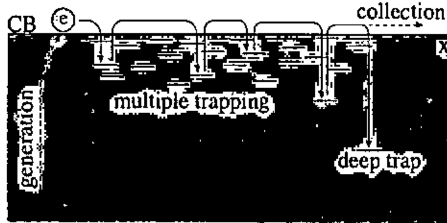

Fig. 1.8. Schematical picture of the multiple trapping process with final collection or deep trapping as it is observed in the TOF experiment.

1.5. The steady-state photoconductivity and the steady-state photocarrier grating technique

In the Steady-State Photoconductivity (SSPC) and the Steady-state Photocarrier Grating (SSPG) measurements, a steady-state situation between carrier generation and recombination is established. Thus, the characteristic times involved in these experimental methods are the **recombination times of free carriers τ_n^R and τ_p^R** defined as:

$$G = R = \frac{n_f}{\tau_n^R} = \frac{p_f}{\tau_p^R} \tag{1.24}$$

The steady-state photoconductivity SSPC

In the steady-state photoconductivity measurements (see i.e. [Crandall 84]), a technique which is extensively used for the characterisation of all kinds of photosensitive materials, the sample is continuously illuminated with a weakly absorbed light which homogeneously generates a constant number of free carriers in the material. The photocurrent, which is carried by the free electrons and free holes between two ohmic contacts, is measured and the photoconductivity can be deduced:

$$\sigma_{ph} = e \cdot \left(\mu_n^o n_f + \mu_p^o p_f\right) \tag{1.25}$$

When the material has an extrinsic character, e.g. when the role of majority and minority carriers can be clearly assigned to the one or the other type of carrier, the photoconductivity directly monitors the properties of the **majority carriers** in the material.

The steady-state photocarrier grating technique SSPG

The SSPG measurement technique, as it is used in this work, was introduced for a-Si:H by Ritter et al. [Ritter 86] and allows the determination of the ambipolar diffusion length L_{amb} in a-Si:H. The sample is thereby illuminated by two coherent light beams which form interference fringes in the sample. As the light is absorbed, this light pattern translates into a carrier fringe pattern in the material, creating "light" zones with a high carrier concentrations and "dark" zones with low carrier concentrations. The concentration gradients between "light" and "dark" zones give rise to diffusion currents which tend to erase this carrier pattern. Thereby, the constraints of the basic transport equations (1.2) - (1.6) determine the diffusion process of carriers: the electrons and holes do not move independently but as neutral pairs, coupled by an internal field (ambipolar diffusion), and in permanent interaction with the huge reservoir of carriers in the bandtails. Furthermore, the diffusion process is limited here by the less numerous carrier and thus, the SSPG technique measures the **minority carriers** transport properties in a-Si:H material.

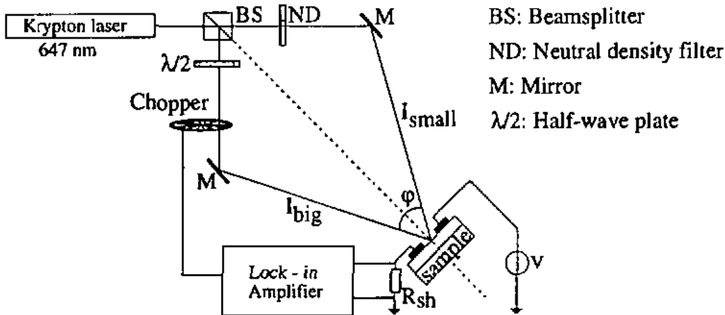

Fig. 1.9. Experimental interferometer set-up of the SSPG measurement. For the measurement, the sample position is moved stepwise along the dashed line, varying thereby the angle φ and the grating constant Λ. For each position σ_{ph} with and without interference fringes is measured by lock-in technique. For details about the experimental set-up see [Sauvain 92].

The experimental set-up of the SSPG measurement is drawn in fig. 1.9. For the measurement, a weak light beam is coherently superimposed to a strong bias light, creating an interference pattern of low contrast and giving rise to a perturbation of the photoconductivity. By detecting this perturbation by lock-in technique for different grating constants of the interference fringes L_{amb} can be deduced. However, as shown by Ritter et al. ([Ritter 88]) and Sauvain ([Sauvain 92]), two important conditions must be fulfilled to extract the proper

ambipolar diffusion length. First, the a-Si:H must be a **"lifetime material"**, e.g. the lifetime of the electron-hole pair must be longer than the characteristic time which is necessary for its creation (relaxation time). And secondly, the spatially extension of this neutral pair (L_{diel}) must be smaller than the distance over which it diffuses (L_{amb}). This second condition is called **ambipolar or quasi-neutrality condition.**

The theoretical background of the SSPG measurement was first presented by Ritter et al. [Ritter 87], [Ritter 88] who neglected, however, the contribution of ionised dangling bonds to the total charge which turned out to the wrong approach for the case of a-Si:H. More recent and detailed studies by Sauvain [Sauvain 92] and Shah et al. [Shah 97] which include dangling bond charges found, that both conditions mentioned above are generally satisfied in a-Si:H (see also [Shah 96]). The evaluated ambipolar diffusion length can then be related to the mobility - recombination time products by the following expression [Sbah 97]:

$$L_{amb}^2 = \frac{kT}{e} \frac{\mu_n^0 \tau_n^R \cdot \mu_p^0 \tau_p^R}{\mu_n^0 \tau_n^R + \mu_p^0 \tau_p^R} \cdot C \tag{1.26}$$

where C is a constant which represents the influence of the localised charges and has a value between 1 and 2 [Shah 97]. From (1.26) it becomes evident, that the ambipolar diffusion process is limited by the carrier with the smaller $\mu^o\tau^R$ product and thus SSPG measures the **minority carriers** transport properties in a-Si:H material. By this fact, the SSPG technique perfectly complements the SSPC measurement: together they show a complete picture of the transport properties (of electrons and holes) in a-Si:H under illumination.

The parameter b

The ratio of electrons and hole $\mu^o\tau^R$ products is called b and reflects the position of the two quasi-Fermi levels E_{Fn} and E_{Fp} with respect to midgap. Thus, the magnitude of b can be used as a monitor for the n-type or p-type character of the material for a given steady-state illumination. b was first introduced by Ritter [Ritter 87]; it is, according to [Shah 97] more usefully defined as:

$$b = \frac{\mu_n^0 n_f}{\mu_p^0 p_f} = \frac{\mu_n^0 \tau_n^R}{\mu_p^0 \tau_p^R} \tag{1.27}$$

The parameter b can, thus, be deduced from σ_{ph} and L_{amb} measurements, using either the above definition (1.27) or, in the case of intrinsic or degraded a-Si:H, using the following expression which can easily be found by combining the definition of the photoconductivity (1.25) and the formula for the ambipolar diffusion length (1.26).

$$\frac{b}{(b+1)^2} = \frac{L_{amb}^2 e^2 G}{kT\sigma_{ph} C} \tag{1.28}$$

1.6. The $\mu\tau$ problem

For a long time it has been controversial, why in a-Si:H the transient $\mu\tau$ product determined by TOF measurements was about two order of magnitudes lower than the steady-state $\mu\tau$ products obtained by SSPC. A number of authors investigated in this subject which became known under the name "$\mu\tau$ problem". As TOF measurements are performed in sandwich configuration, whereas in SSPC the transport is detected in coplanar direction, the discrepancy between the steady-state and transient $\mu\tau$ products was first attributed to a strong anisotropy in a-Si:H [Schiff 86]. However, Kočka et al. demonstrated with the help of a very particular peeled off sample, that in a-Si:H no such anisotropy exists [Kočka 91-2]. He then proposed, in a similar way to Antoniadis et al. [Antoniadis 90], that in steady-state measurements a deep-trapped carrier undergoes many thermal emission and capture events before it recombines, leading, thus, to a prolonged recombination time. On the other side, Zhu et al. [Zhu 86], Mackenzie et al. [Mackenzie 87] and Crandall et al. [Crandall 91] correctly pointed out, that the characteristic times in TOF experiments (deep-trapping time) and SSPC measurements (recombination time) are different quantities. They argue, that deep-trapping as observed by TOF is a one-carrier process, whereas the recombination process involves two carriers, and thus it is evident that the latter requires a longer time.

Here we will show (after checking that thermal emission cannot explain the $\mu\tau$ problem) that even though deep-trapping time and recombination time are indeed different quantities, this is not the direct origin of the $\mu\tau$ problem. Rather than that, we will focus on the differences in experimental conditions between transient and steady-state experiments, namely on the fact that TOF measurements are performed at thermal equilibrium (i.e. in the dark) whereas SSPC (and SSPG) are measured under illumination. Thereby, we will base our argumentation on transient and steady-state $\mu\tau$ measurements we performed on a series of undoped and micro-doped a-Si:H samples. For the interpretation of our measurements we will make use of the theoretical considerations as introduced in ch. 1.3. and 1.4.

1.6.1. Experimental

We deposited by the VHF-GD technique [Curtins 87] a series a-Si:H layers on glass (Corning 7059) and on Cr-coated glass substrate. The volumic gas concentrations were thereby varied between 0.2 ppm and 1 ppm of PH_3 and 0.5 ppm and 10 ppm of B_2H_6 in pure silane. The thicknesses of the deposited films ranged from 2.2 μm to 5 μm.

For TOF measurements, the layers, deposited on Cr-coated glass, were provided by semitransparent Cr contacts to form a double Schottky diode sandwich structure (Cr(1500 Å) / a-Si:H / Cr(150 Å)). For the steady-state experiments two coplanar aluminium contacts separated by a gap of 0.5 mm were evaporated on the layers deposited on glass substrate.

1.6.2. Steady-state and transient $\mu\tau$ products in micro-doped a-Si:H

The steady-state ($(\mu\tau)_{ss}$) and transient ($(\mu\tau)_{tr}$) $\mu\tau$ measurements as a function of the Fermi level position in the dark (evaluated from dark conductivity measurements) are plotted in fig. 1.10. They show a surprising result: the $\mu\tau$ problem is a majority carrier problem only. Whereas for majority carriers the typical difference of about 100 is observed, the $\mu\tau$ products of minority carriers have - within experimental errors - comparable values [Beck 93].

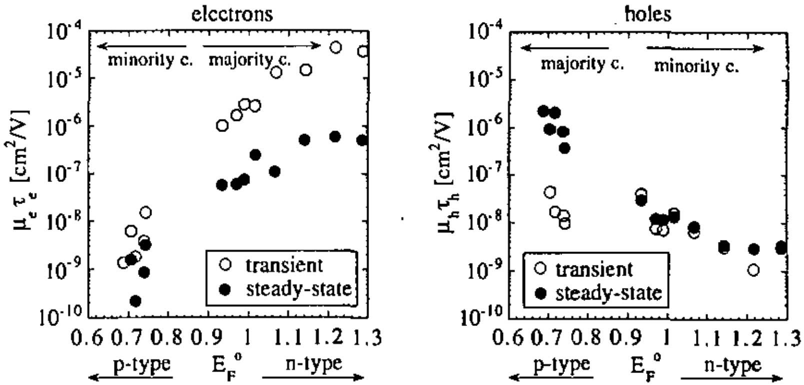

Fig. 1.10. Comparison of steady-state $(\mu\tau)_{ss}$ and transient $(\mu\tau)_{tr}$ of electrons and holes as a function of the dark Fermi level position. A remarkable difference in $(\mu\tau)_{ss}$ and $(\mu\tau)_{tr}$ is only observed for majority carriers.

1.6.3. How important is thermal emission from dangling bonds?

To answer the question if thermal emission is important enough to eventually explain the $\mu\tau$ problem (as proposed by [Antoniadis 90], [Kočka 91-2]) we estimated the thermal emission rates in our a-Si:H material by the following method:

In thermal equilibrium where the free carrier capture rates are equilibrated by thermal emissions (see also fig. 1.4):

$$r_{cn}^0 = r_{en}^-; \quad r_{cn}^+ = r_{en}^0; \quad r_{cp}^0 = r_{ep}^+; \quad r_{cp}^- = r_{ep}^0 \tag{1.29}$$

Let us now consider i.e. an n-type material where negatively charged dangling bonds (D^-) prevail. In this case, the electrons in the transient TOF experiment are captured on D^0 states (as $D^+ \ll D^0$) and we can write:

$$\left(\mu_n^0 \tau_n\right)_{tr} = \frac{\mu_n^0}{v_{th} N_{db} \sigma_n^0 f^0} = \mu_n^0 \frac{n_f^0}{r_{cn}^0} \underset{(1.29)}{\uparrow=} \mu_n^0 \frac{n_f^0}{r_{en}^-} \tag{1.30}$$

Combining (1.30) with the dark conductivity of n-type material $\sigma_d = \mu_n^0 n_f^0 e$, we obtain a simple expression to estimate the thermal emission rate of electrons from negatively charged dangling bonds to the conduction band:

$$r_{en}^- = \frac{\sigma_d}{\left(\mu_n^0 \tau_n\right)_{tr} e} \tag{1.31}$$

Similar considerations can be done for p-type samples in order to estimate the hole thermal emission rate from D^+ states: r_{ep}^+.

The deduced **dark** thermal emission rates for majority carriers are represented in fig. 1.11 [Beck 93]. Even though these rates were deduced for the thermal equilibrium, they are hardly changing with illumination since almost all dangling bonds remain charged in extrinsic material. A particular case may be undoped a-Si:H. We considered it to be a n-type material in the dark, but we put the obtained value in brackets as this assumption may be questioned.

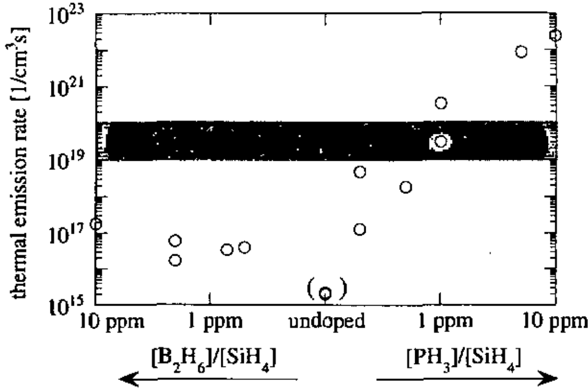

Fig. 1.11. Estimation of the majority carrier thermal emission rate from deep defects to bands in obscurity as a function of doping. For extrinsic material (where charged dangling bonds dominate) the thermal emission rate will hardly change with illumination. The value obtained for undoped a-Si:H is put in brackets as it was deduced using the same assumptions as for n-type a-Si:H.

The grey bar in fig. 1.11. indicates the usual generation rates ($1\cdot10^{19}$ - $1\cdot10^{20}$ $1/cm^3s$) used for our steady-state measurements. It clearly shows that thermal emission rates from deep defects are in general (much) lower than these generation rates (for moderately doped samples) and thus cannot account for the observed discrepancy between steady-state $(\mu\tau)_{ss}$ and transient $(\mu\tau)_{tr}$.

1.6.4. Solving the $\mu\tau$ problem

In the previous chapter we have shown that thermal emission can be ruled out to be at the origin of the observed discrepancy between $(\mu\tau)_{ss}$ and $(\mu\tau)_{tr}$. This result, however, motivated us to follow up another approach in order to explain the $\mu\tau$ problem: we directly compared the analytical expressions of the recombination times (1.13) and (1.14) (where thermal emission is neglected) and of the deep-trapping times (1.22) and (1.23) as given in the previous chapters. At first glance, these expressions for deep-trapping times and recombination times look the same. However, at a second sight, one realises that even though they are **analytically** identical, an important difference resides in the dangling bond occupation functions: whereas the occupation functions in the TOF experiment are given by the **thermal equilibrium** situation, those in SSPC and SSPG measurements are determined by the **steady-state equilibrium**. On one side, the thermal equilibrium the dangling bond occupation functions (1.8) - (1.10) are thus governed by the dark Fermi level position, the energetical position of the neutral dangling bond states and the correlation energy U. On the other side, under steady-state illumination, the dangling bond occupations (1.15) - (1.17) are governed by the capture rates of free carriers only and the relevant parameters here are the free carrier densities and the capture cross sections of neutral and charged dangling bonds. This signifies that the parameters which determine the deep-trapping time in transient measurements and the recombination time in steady-state measurements are fundamentally different and therefore steady-state $(\mu\tau)_{ss}$ and transient $(\mu\tau)_{tr}$ can a priori hardly be compared.

However, in most cases when one type of dangling bonds clearly prevails in thermal equilibrium as well as under illumination, the $\mu\tau$ products which are governed by these states become the same. This is what we observe for minority carriers which are captured on the predominant charged dangling bonds in extrinsic a-Si:H: holes are captured on D^- states in n-type a-Si:H, electrons on D^+ states in p-type material. In contrast to this the situation for majority carriers is very different as their $\mu\tau$ products are governed by the few remaining D^0 states. There is, in fact, no compelling reason why the density of these D^0 states should be the same in thermal equilibrium and under illumination. And, hence, there is also no reason why the majority carrier $\mu\tau$ products should be the same in the dark and under illumination. In other words, the observed difference between $(\mu\tau)_{ss}$ and $(\mu\tau)_{tr}$ of majority carriers can be attributed to a variation of the density of neutral dangling bonds with illumination.

To obtain a more quantitative solution of the $\mu\tau$ problem it would be necessary to perform numerical calculations. Nevertheless, considering the large number of parameters involved (where some of them are still quite controversial in a-Si:H), this approach was not followed up here.

2. $\mu^o\tau^o$ PRODUCTS - A TOOL FOR CORRELATING a-Si:H FILM PROPERTIES AND SOLAR CELL PERFORMANCES

The transport measurement techniques as introduced in section 1 serve to characterise thin layers of a-Si:H with the aim to incorporate the studied materials into p-i-n solar cells. However, the application of the results gained on layers to p-i-n solar cells is far from being straightforward, as will be shown hereafter. The issue was thus to find a way to extract from the parameters measured on layers the part of information which is also relevant for the solar cell operation. In other terms we searched for a parameter, measurable on a-Si:H layers, which can **correlate** the layer properties with cell performances.

The parameter we introduced to this end is the **$\mu^o\tau^o$ product**. We will define it in this chapter and explain why $\mu^o\tau^o$ has the potential to relate layer properties and solar cells made out of these materials. Thereafter we will show how $\mu^o\tau^o$ can be evaluated from transport measurements by simultaneously performing SSPC and SSPG measurements.

We then will apply our evaluation method of $\mu^o\tau^o$ to different series of a-Si:H layers and deduce from these measurements the ratio of capture cross sections of charged to neutral dangling bonds, a parameter which is necessary for the evaluation of $\mu^o\tau^o$. Finally, we apply our method to two series of layers and corresponding p-i-n cells, illustrating the application of $\mu^o\tau^o$ in a practical case and its successful correlation with cell efficiency.

2.1. $\mu^o\tau^o$ products as a correlation parameter

In the past, the approach followed up by many people to improve the efficiency and stability of a-Si:H solar cells was the optimisation of a-Si:H layer material. However, this way was not always successful in the way that a-Si:H layer materials which were judged to be "better" not necessarily resulted in higher or more stable efficiencies when incorporated in a p-i-n cell device. This lack of apparent correlation between the properties measured on layers and the corresponding cell performances was pointed out by several authors ([Lechner 89], [Wronski 93], [Schropp 93], [Yang 94]). Some of them even concluded from their observations that a-Si:H material should only be optimised in the device configuration directly. We don't share this opinion. As p-i-n cells are far more complex devices it is difficult to get reliable information about the i-layer material quality without being influenced by structural effects (interfaces, doped layers etc.). Therefore we would like to present in this work another approach based on the characterisation of a-Si:H material in layer configuration.

We first focused on the characteristic differences existing between a simple a-Si:H layer on glass (as used for material characterisation) and the i-layer as inserted in a p-i-n structure of a

solar cell. One of the main differences resides in the occupation of the dangling bond states. Whereas in a homogeneous a-Si:H film of sufficient thickness the dangling bond occupation can basically assumed to be constant, this does not apply for solar cells. In a p-i-n cell the charge state of the dangling bonds is given by the internal electric field which forms important space charge zones (see fig. 2.1), creating thereby a dangling bond charge profile across the i-layer. Recalling now to our mind the findings of ch. 1, namely the impact of the dangling bond occupation on the transport measurements, one realises, that the problem of missing correlation may reside in this difference.

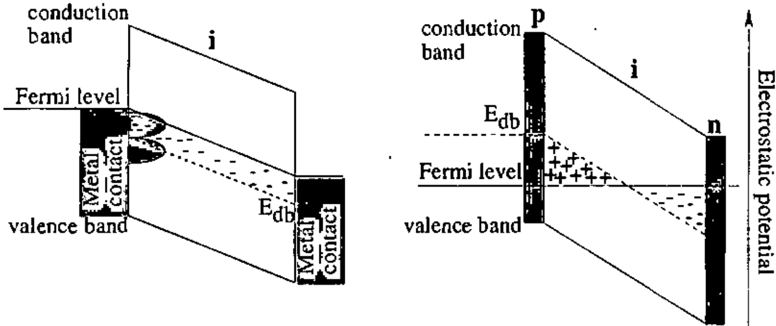

Fig. 2.1. Schematical representation of the dangling bond occupation (a) in a homogeneous layer with two ohmic metal contacts (i.e. aluminium) and (b) in a p-i-n cell in open circuit voltage. E_{db} indicates the position of the Fermi level in completely intrinsic a-Si:H (all dangling bonds are neutral). Whereas in case (a) the dangling bond occupation is determined by the a-Si:H material, in case (b) the doped p- and n-layers build up a large space charge zone which leads to a strongly inhomogeneous distribution of dangling bond charge in the i-layer.

We thus set out to find a parameter which is independent on the actual dangling bond occupation on one side, but which still contains the important information about the two crucial parameters for solar cell operation, namely about the band mobility μ^o and the deep defect density N_{db}, on the other side. The parameter we introduced for this purpose is a $\mu^o\tau^o$ product, at first two separate ones for electrons and holes, which we defined as:

$$\mu_n^o\tau_n^o = \mu_n^o\frac{1}{v_{th}N_{db}\sigma_n^o} \qquad \mu_p^o\tau_p^o = \mu_p^o\frac{1}{v_{th}N_{db}\sigma_p^o} \tag{2.1}$$

Physically, these new products of band mobility (μ^o) × capture time (τ^o) correspond to the value that the $\mu\tau$ product (measured in a-Si:H layer) would take if all defects in the material were neutral. These $\mu^o\tau^o$ products as defined above satisfy to our requirements: they are independent of the prevailing dangling bond occupation in the material but still represent the

band mobility and the defect density. They do also not suffer from the known drawbacks of deep defect density measurements, namely, the limitations in photothermal deflection spectroscopy (PDS) (residual absorption of the substrate in the region of defect absorption [Nonomura 94]) and constant photocurrent method (CPM) (incorrect determination of the defect density in p-type a-SiH [Mettler 94]). Furthermore, we will be show later on that these $\mu^o\tau^o$ products are closely related to the performances of a-Si:H solar cells, as far as the latter is controlled hy the quality of the intrinsic layer.

2.2. The evaluation of the product $\mu^o\tau^o$ from SSPC and SSPG measurements

2.2.1. Evaluation of $\mu^o\tau^o$ products: from transient or steady-state measurements?

To determine the $\mu^o\tau^o$ product we adopted the following approach: starting from the existing and well known $\mu\tau$ products (from TOF or SSPC/SSPG), we will first settle the role of the dangling bond charge on these $\mu\tau$ products and subsequently we will try to find a way how to eliminate this influence of dangling bond occupation. However, the $\mu\tau$ products deduced from TOF and SSPC/SSPG are not equally suited for this procedure as we will briefly discuss in this chapter.

In the TOF measurement, as we described in chapter 1.4.1, the dangling bond charge is given by the thermal equilibrium values (1.8) - (1.10). This means that if we intend to evaluate f_o^0, f_o^+ and f_o^- for this measurement technique, we need to know precisely the dark Fermi-level position E_{Fo} and the correlation energy U. Furthermore, in the dark, the energetical distribution of the dangling bond states also controls their occupation and therefore should be known. As the experimental determination of E_{Fo} is not evident [Overhof 89] and the value of U is controversial (U may lie somewhere between 0.1 eV and 0.3 eV [Jackson 82-2], [Stutzmann 87]), an estimation of the dangling bond occupation in TOF experiments, as would be necessary to deduce $\mu^o\tau^o$, becomes, in general, a difficult task.

In SSPC and SSPG measurements the situation is quite different. For high enough illumination, where thermal emissions from deep defects as well as recombination by band-tail states can be neglected (see ch. 2.2.3), almost all dangling bonds are comprised between the two quasi-Fermi levels. They act as recombination centres and their energetical distribution has virtually no influence any more. The recombination model introduced in ch. 1.3.3 is then a valid approximation: free carriers recombine through these dangling bond states and the dangling bond occupation functions become exclusively governed by the recombination traffic of free electrons and holes as given by the expressions (1.15) - (1.17). As SSPC and SSPG

measurements also directly monitor these free carrier densities (see (1.25) and (1.26)), we dispose of an additional advantage: we can evaluate the dangling bond charge within the same experimental framework without the need of any additional experimental methods.

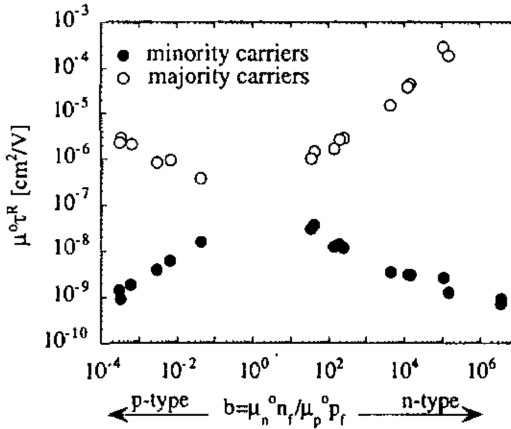

Fig. 2.2. Anticorrelated change of majority and minority carrier $\mu^o\tau^R$ products with micro-doping as measured by SSPC and SSPG.

In other terms this means that SSPC and SSPG are not two independent measurements. Thereby, the majority and minority carrier $\mu^o\tau^R$ products evaluated are closely related to each other by their common recombination centres, the dangling bonds. Experimentally, this fact becomes apparent as an anticorrelated behaviour of electron and hole $\mu^o\tau^R$ products as shown in fig. 2.2. A similar behaviour has also been reported by Yang et al. [Yang 89]. As this correlation between SSPC and SSPG can also be expressed analytically, we finally give preference to steady-state measurements over TOF. We will thus use for the evaluation of $\mu^o\tau^o$ SSPC and SSPG and take advantage of their correlated behaviour.

2.2.2. Evaluation procedure for $\mu^o\tau^o$

As a first step in our evaluation of $\mu^o\tau^o$, we will make an important simplification, namely:

$$\mu_n^0\tau_n^0 = \mu_p^0\tau_p^0 = \mu^0\tau^0 \qquad (2.2)$$

This simplification can be justified on the base of TOF measurements on compensated (midgap) and degraded a-Si:H samples ([Beck 92], [Beck 93]). In these samples we can assume that almost all dangling bonds in the material are neutral becoming thus the main deep trapping centres for both, electrons and holes. Consequently, the measured $\mu^o\tau$ products approach the "dangling bond charge independent" $\mu_n^o\tau_n^o$ and $\mu_p^o\tau_p^o$ products as $\tau_n \approx \tau_n^o$ and

$\tau_p \approx \tau_p^o$. The TOF measurements on these samples are represented in a in fig. 2.3 where we plotted the $\mu_p^o\tau_p$ product of holes as a function of $\mu_n^o\tau_n$ of electrons. These strongly degraded and midgap samples lie on a straight line with slope 1, representing (in this double-logarithmic plot) a constant ratio of $\mu_n^o\tau_n^o/\mu_p^o\tau_p^o \approx 1.2$. Note that this value is not in contradiction with earlier results presented by Street et al. [Street 83] who found on undoped a-Si:H material a ratio of $\mu_n^o\tau_n/\mu_p^o\tau_p \approx 10$. As the samples studied by Street were undoped (i.e. not compensated, having the usual slightly n-type character), this n-type character will sensitively affect the measured $\mu\tau$ products (via the corresponding dangling bond charge states), and this should be considered the reason for this discrepancy.

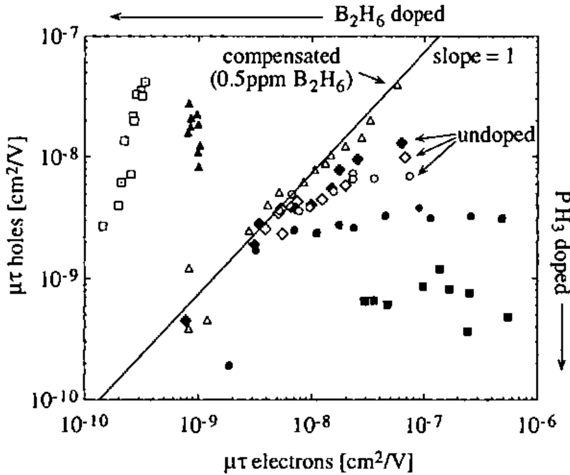

Fig. 2.3. Mutual change of electron and hole $\mu^o\tau$ products obtained by TOF measurements during degradation: the majority carrier $\mu^o\tau$ product starts by dropping and the $\mu^o\tau$ products on all samples show the tendency to join at approximately equal values before degrading further with equal rates. The line with slope 1 indicates the ratio of $\mu_n^o\tau_n^o/\mu_p^o\tau_p^o$ when almost all dangling bonds have become neutral.

The second step is to accurately combine the elements we already have. The most important element is hereby the dangling bond recombination model presented in 1.3.3 which will be assumed to be valid here (see also ch. 2.2.3). It allows an analytical formulation of the dangling bond occupation functions (1.15) - (1.17) and we can substitute them in the expressions for the recombination times (1.13) and (1.14). Mathematical reshaping with the help of the simplification (2.2) and the definition of the b parameter (1.27) finally yields to:

$$\mu_n^0\tau_n^R = \mu^0\tau^0\frac{b}{b+1}\left(\frac{\sigma_n^0}{\sigma_n^+}\frac{1}{b}+1+\frac{\sigma_p^0}{\sigma_p^-}b\right) \tag{2.3}$$

$$\mu_p^0\tau_p^R = \mu^0\tau^0\frac{1}{b+1}\left(\frac{\sigma_n^0}{\sigma_n^+}\frac{1}{b}+1+\frac{\sigma_p^0}{\sigma_p^-}b\right) \tag{2.4}$$

where $\mu_n^o\tau_n^R$ and $\mu_p^o\tau_p^R$ are the experimentally measured $\mu\tau$ product and $\mu^o\tau^o$ the quality related $\mu\tau$ products. Looking at this result it becomes also evident that the measured $\mu^o\tau^R$ products are in general different from the quality related $\mu^o\tau^o$ product. We here need to correct our experimental $\mu^o\tau^R$ values by a certain correction factor which is a function of b and is therefore influenced by doping (also low-level, non-intentional doping).

However, there is at this stage one problem when evaluating $\mu^o\tau^o$ from (2.3) and (2.4): these expressions cannot be applied to "truly" intrinsic material where the role of majority and minority carrier cannot be clearly attributed to electrons or holes. In that case both carriers contribute to photoconductivity and to the ambipolar diffusion length. To prevent this problem, it is more convenient to rewrite the expression of the photoconductivity (1.25) by substituting (2.3) and (2.4). One then obtains:

$$\mu^0\tau^0 = \frac{\sigma_{ph}}{eG}\frac{1}{z}, \qquad z = \frac{1}{f^0} = \left(\frac{\sigma_n^0}{\sigma_n^+}\frac{1}{b}+1+\frac{\sigma_p^0}{\sigma_p^-}b\right) \tag{2.5}$$

This final formula is now valid for all types of a-Si:H materials. It is thereby not necessary to know the individual contributions of electrons and holes to the photoconductivity. If we further assume σ_n^+/σ_n^o and σ_p^-/σ_p^o to be equal (which will be shown in ch. 2.2.1 to be an acceptable approximation), we even do not have to know if the material is n-type or p-type. This can be an advantage when evaluating a-Si:H with non-identified contaminant contents.

To illustrate that such correction is not only a matter of small adjustment but can also be rather large, we calculated hereafter the magnitude of this correction factor z (as a function of doping). The result is plotted in fig. 2.4 for different ratios of charged to neutral capture cross sections. It clearly shows that the $\mu^o\tau^R$, when directly evaluated from SSPC only correctly monitors the material quality in a very restrictive range of intrinsic (midgap) a-Si:H materials (i.e. degraded or "compensated" a-Si:H). In all other materials which have an extrinsic character (b substantially different from 1), $\mu^o\tau^R$ from SSPC does no longer monitor the material quality and needs to be corrected by the factor 1/z. The undoped, but slightly n-type a-Si:H material deposited by the VHF-GD typically fits (in the annealed state) in this category. For extrinsic a-Si:H materials, one can however show that the $\mu^o\tau^o$ product becomes proportional to L_{amb}^2 as deduced from SSPG. This means, that when optimising undoped and slightly n-type (undegraded) a-Si:H for solar cell applications, one should seek to improve L_{amb} rather than σ_{ph}. Li et al. [Li 93] indeed came to the same conclusion and attributed his observations to the shorter drift length of holes compared to electrons.

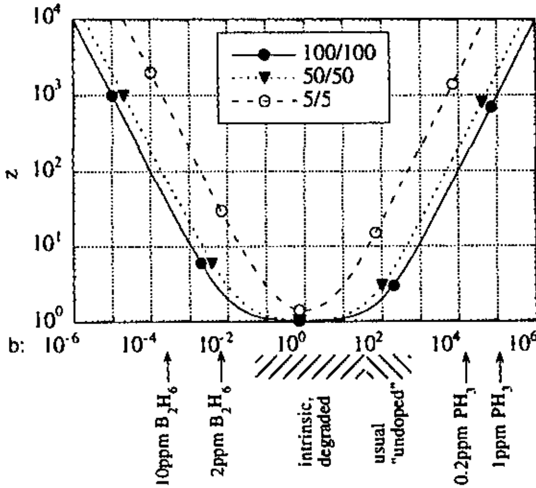

Fig. 2.4. shows the calculated magnitude of the correction factor z os o function of the parameter b. In order to obtain the quality related $\mu^o\tau^o$ product, the $\mu^o\tau^R$ deduced from photoconductivity has to he devided by z (see 2.5). We also indicated typical experimental b values as obtained for undoped, degraded and micro-doped a-Si:H. The numbers in the box indicate the ratio of charged to neutral capture cross sections used for calculation.

Note finally, that the ratio of charged to neutral capture cross sections σ_n^+/σ_n^o and σ_p^-/σ_p^o compared to the parameter b marks the limit between intrinsic and extrinsic a-Si:H and thus plays an important role. This subject will be addressed in more detail in the following chapter.

Expression (2.5) may also be used to gain information about the relative stability of an a-Si:H material under light-soaking. For the given hypothesis that μ^o is *not* changing with degradation [Wyrsch 91-1], the measure of $\mu^o\tau^o$ in the annealed as well as in the degraded state can be used as a measure for the increase in deep defect density:

$$\frac{\left(\mu^0\tau^0\right)_{initial}}{\left(\mu^0\tau^0\right)_{degraded}} = \frac{\left(N_{db}\right)_{degraded}}{\left(N_{db}\right)_{initial}} \tag{2.6}$$

2.2.3. Estimation of the ratio of the capture cross sections

For the evaluation of $\mu^o\tau^o$ from measured quantities according to (2.5) we have to know the ratios of capture cross sections σ_n^+/σ_n^o and σ_p^-/σ_p^o. As the values these ratios are not very well known for a-Si:H (data published in literature range from 1.8 [Hattori 91] to 4 [Street 83] and values ≥ 100 [Wyrsch 91-2], [Günes 94]) we will dedicate here a chapter to the evaluation of σ_n^+/σ_n^o and σ_p^-/σ_p^o before applying our method to a-Si:H materials.

To gain more information about σ_n^+/σ_n^o and σ_p^-/σ_p^o we performed two different experiments: we measured the change of $\mu^o\tau^o$ with light soaking and micro-doping. If we assume that $\mu^o\tau^o$ is proportional to $1/N_{db}$, e.g. that the band mobility is not substantially changed by light-soaking or by micro-doping [Wyrsch 91-1], we can deduce from these experiments an approximate ratio of the capture cross sections. The samples used for these measurements were the same as in ch. 1.6.

Microdoping

It is a well-documented fact that doping with boron or phosphine introduces additional dangling bonds in a-Si:H [Stutzmann 87], [Street 91]. As an empirical law they found that the density of deep defects N_{db} is proportional to $1/\sqrt{[dopant]/[SiH_4]}$. Taking into account the assumptions made above, the $\mu^o\tau^o$ product should thus reproduce this $\sqrt{[dopant]/[SiH_4]}$ law for a correctly chosen ratio of capture cross sections.

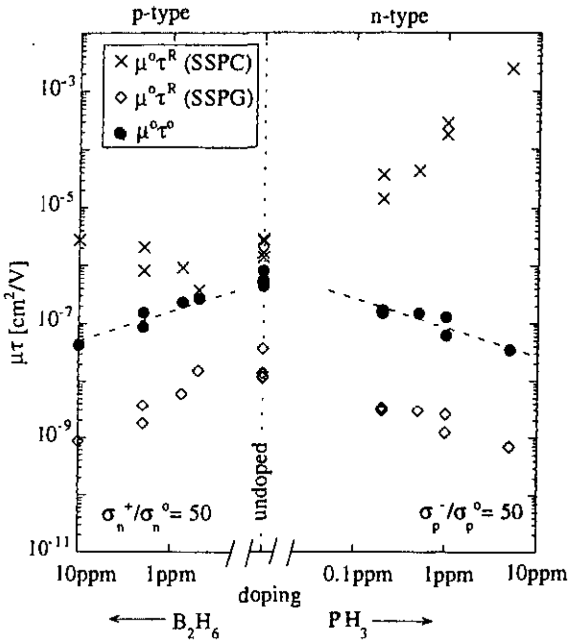

Fig. 2.5. Variation of the experimental $\mu^o\tau^R$ products and of the deduced $\mu^o\tau^o$ with boron and phosphine doping. For a ratio of capture cross sections $\sigma_n^+/\sigma_n^o = \sigma_p^-/\sigma_p^o \approx 50$ we find a $1/\sqrt{[dopant]/[SiH_4]}$ dependency as indicated by the dotted line.

As represented in fig. 2.5 we indeed can obtain a $1/\sqrt{[dopant]/[SiH_4]}$ dependency of $\mu^0\tau^0$ for $\sigma_n^+/\sigma_n^0 = \sigma_p^-/\sigma_p^0 = 50$ as indicated by the dotted lines. However, we have to add a comment here. For n-type doping, even low phosphine incorporation already pushes the Fermi level far to the conduction band and almost all defects in the material become negatively charged. Consequently the σ_p^-/σ_p^0 is not a critical parameter for the evaluation of $\mu^0\tau^0$ here and no information can be gained about it. For p-type doping the situation is more helpful as doping with boron is much less efficient. Here, a $1/\sqrt{[dopant]/[SiH_4]}$ can only be reproduced when the ratio σ_n^+/σ_n^0 is adjusted to about 50 (with a tolerance of about a factor of 2).

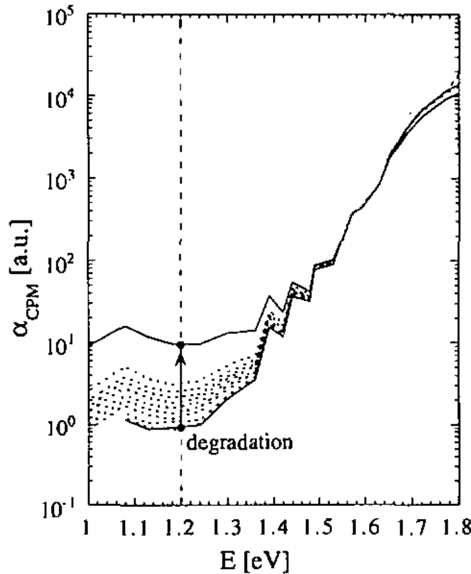

Fig. 2.6. Increase of the subbandgap absorption connected to increasing dangling bond density measured by CPM. The initial part of degradation, accompanied by a decrease of the dark conductivity, is not drawn in the plot; the calibration of the CPM curve was made by PDS measurements for the initial state and then adjusted at E = 1.6 eV during the degradation. The absorption at the shoulder (1.2 eV) was then used as a measure of the dangling hond density.

Light-soaking

For the degradation experiment we chose a typical undoped, slightly n-type a-Si:H layer with a thickness of 2.4 µm. This layer was stepwise degraded with a Krypton laser (λ=647 nm) at a power density of about 100 mW/cm^2. After each step we measured SSPC,

SSPG and CPM spectra. The very initial part of degradation which was accompanied by a decrease of dark conductivity, was omitted as it was shown that CPM may not measure correctly the absorption spectra in this case [Brandt 91], [Mettler 94]. While degrading further, the dark conductivity remained constant and the absorption at 1.2 eV was used as a monitor for the deep defect density (see fig. 2.6). Then, the mutual change of $\mu^o\tau^R$ products deduced from SSPC and SSPG was fitted with different values of capture cross sections σ_p^-/σ_p^o as indicated in fig. 2.7. The best fit was obtained for $\sigma_p^-/\sigma_p^o \approx 50$ (tolerance of about a factor of 2). For this value, we plotted (also in fig. 2.7) the resulting $\mu^o\tau^o$, which decreases as expected proportionally to $1/\alpha_{CPM}$ (1.2 eV).

As previous work [Mettler 94] has shown that CPM may not correctly measure the absorption spectra for slightly p-type samples, no similar experiments were carried out for such samples (in order to find σ_n^+/σ_n^o).

Summarising this chapter, we have found, by the two experiments of light-soaking and micro-doping, a value of the ratio of capture cross sections of $\sigma_n^+/\sigma_n^o = \sigma_p^-/\sigma_p^o \approx$ **50** (with a tolerance of about a factor of 2); this value will be used throughout this work.

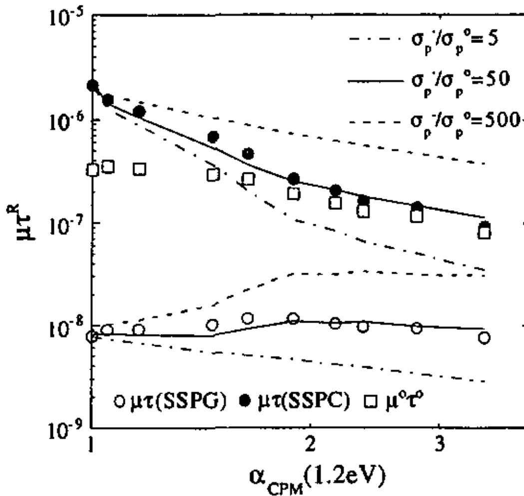

Fig. 2.7. Variation of the experimental $\mu^o\tau^R$ products for an undoped but initially slightly n-type a-Si:H layer as a function of the increasing deep defect density as evaluated from CPM spectra. The best fit was obtained using a ratio of capture cross sections $\sigma_p^-/\sigma_p^o = 50$ which results in a $\mu^o\tau^o$ product which is almost proportional to $1/\alpha_{CPM}$ (1.2 eV).

2.2.4. The role of $\mu^o\tau^o$ products in a-Si:H solar cells

It is conceptually quite obvious that in the ideal case a monotonous relation between $\mu^o\tau^o$ products and the corresponding solar cell performances exists, e.g. that a material with high band mobility and low defect density leads to good collection of the photogenerated carriers in the cell. On the other side, to find a quantitative relation between $\mu^o\tau^o$ and the solar cell operation is rather difficult due to the complexity of the p-i-n device and the fact that in the transport equations used to describe the operation of the p-i-n solar cell, the parameters μ and τ generally do not appear as product. However, in a very simplified situation (constant electric field, majority of defects are neutral) a direct relationship between the $\mu^o\tau^o$ product and the collection χ in the solar cell could be established analytically [Hubin 92].

Another points which should be addressed here are the other factors influencing the collection in a p-i-n solar cells. The quality of the interfaces, the optical absorption, the i-layer thickness or reflection properties are all contributory factors to the overall solar cell efficiency. They can, however, change from one cell to the other and are by no means taken into consideration in the evaluation of the $\mu^o\tau^o$ parameter. The $\mu^o\tau^o$ parameter can thus relate layer properties and cell performances only when the latter is limited by the quality of the intrinsic layer. However, for any given cell, the $\mu^o\tau^o$ product can always help to distinguish between problems related to the quality of the i-layer material and other structural problems.

2.2.5. Validity of the method and its limitations

Before stepping to the correlation between layer and cell properties, let us conclude the chapter 2.2 with a brief discussion about the validity of the method of $\mu^o\tau^o$ products presented here. The simplicity and the transparency of the evaluation procedure (2.5), achieved by strict approximations and hypothesis, have their price: the method has a well limited range of validity, as will be discussed hereafter. However, if we are able pinpoint this range, $\mu^o\tau^o$ can be used efficaciously within this frame.

The basic assumption of the $\mu^o\tau^o$ evaluation method is the dangling bond recombination model (see ch. 1.3.3). Thus, the validity of our method is in principle given by the range of experimental conditions where the dangling bond recombination model is a valid approximation. As the validity of the latter has been discussed theoretically by several authors (i.e. [Vaillant 86], [Hubin 92], [Zhou 92]) in detail, we will not repeat it here. We therefore would like just to stress the importance of choosing the appropriate experimental conditions; e.g. the use of homogeneously absorbed light (in our case a krypton laser with $\lambda = 647$ nm) and an illumination level which allows a correct measurement of SSPC and SSPG. Furthermore the illumination should be sufficient to include almost all dangling bonds between the two quasi-Fermi levels E_{Fn} and E_{Fp} (because only these dangling bonds can be seen by steady-state experiments), but not too high, so that the recombination by band tail states can be neglected

(see fig.1.6). If this second condition is not fulfilled and bandtail states become involved in the recombination process, the evaluated apparent $\mu^o\tau^o$ product is reduced. However, for our measurements, we worked - if not mentioned differently - at generation rates between 10^{19} and 10^{20} 1/cm^3. For such medium high illumination levels, it has been shown by Zhou et al. [Zhou 94], that the dangling bonds are indeed the main recombination centres.

The generally observed non-linear dependency of the photoconductivity on the generation rate (for undoped, but slightly n-type a-Si:H) is not fully understood yet and cannot be explained by the dangling bond recombination model. Connected to this, the evaluated $\mu^o\tau^o$ product in certain cases also exhibits a slight dependency on the illumination intensity (power-law exponent between 0 and -0.3).

The ratio of capture cross sections determined in ch. 2.2.1 is a rough estimation and was considered to be constant in all samples. This ratio fixes the limit between intrinsic and extrinsic a-Si:H and it also determines the absolute value of $\mu^o\tau^o$ in extrinsic samples. It thus plays an important role in the evaluation of $\mu^o\tau^o$ products and a more precise knowledge of its value would be desirable.

On the other side, the assumption of $\mu_n^0\tau_n^0 = \mu_p^0\tau_p^0 = \mu^0\tau^0$ was introduced in ch. 2.2 to gain physical insight and is not a necessary condition. Omitting this simplification would lead to an additional constant in the final result but would not change in any way the physics.

2.3. Correlation between $\mu^o\tau^o$ of a-Si:H layers and solar cell performances

---

In this chapter we will experimentally compare the $\mu^o\tau^o$ products of a-Si:H layers with the efficiencies of p-i-n solar cells incorporating the "same" material (produced using the same deposition parameters) in the i-layer. Our aim is thereby to experimentally confirm that a correlation between $\mu^o\tau^o$ and cells indeed exists. For our experiments we changed the quality of the a-Si:H material by varying the deposition temperature which is known to strongly influence the properties of the material.

2.3.1. Experiment

Two series of pairs, each of them consisting of an a-Si:H layer and a thin p-i-n cell, were produced by the VHF-GD deposition technique [Curtins 87]; thereby, the deposition temperature was varied from 120°C to 200°C (low temperature series) and from 150°C to 320°C (high temperature series). In this context, first an approximately 2.5 µm thick, undoped a-Si:H film was deposited on a glass substrate and provided with two coplanar, ohmic aluminium contacts. Subsequently, using the same deposition parameters, this a-Si:H material was incorporated as an i-layer (thickness ≈ 0.6 µm) in a standard p-i-n solar cell on glass coated

by transparent conductive oxide (TCO) (Asahi type U). Both cells and layers were then annealed for 2 h at 180°C.

The layers were characterised by SSPG and SSPC, by PDS and CPM as described already in previous chapters. Furthermore, the dark conductivity and the optical band gap (from Tauc's plot) were determined. For the cells, the conversion efficiency η, the open-circuit voltage V_{oc}, the short-circuit current density j_{sc}, and the fill factor (FF) were evaluated using a two-source solar simulator (Wacom WXS-140S-10).

The layers were light soaked during 4 weeks by a 6 sun high-pressure sodium lamp (spectral maximum at 590 nm with a full width at half-maximum (FWHM) of around 40 nm) at 46°C. The cells were degraded during 3 weeks by an AM1.5 light source of 100 mW/cm^2 (array of Philips PL-L 24W/95/4P lamps) at 47°C.

2.3.2. The annealed state

The results obtained in the annealed state are listed in table I (layers) and table II (cells) and plotted in fig. 2.10. As a general tendency, the increasing deposition temperature improves the quality of the layer - monitored by the $\mu^o\tau^o$ product - as well as the cell efficiency . This behaviour is observed for both series even though the individual variations of efficiencies and $\mu^o\tau^o$ within one series are quite different.

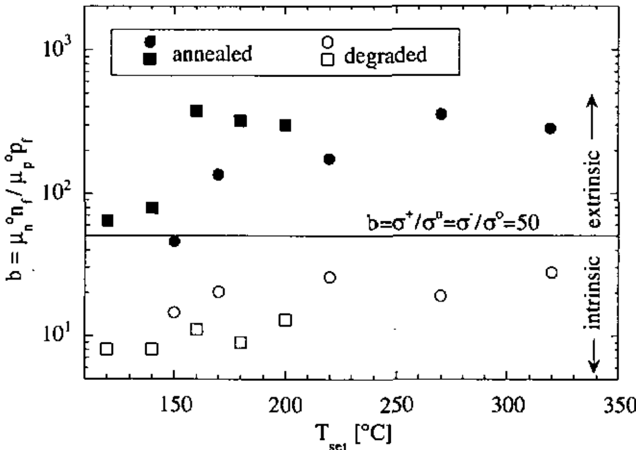

Fig. 2.9. Variation of the value of the parameter b with light-induced degradation for the two temperature series (circles for the high temperature series and squares for the low temperature series) of undoped layers: while in the annealed state almost all materials are shown to have the typical slightly extrinsic character, they all become truly intrinsic (midgap) with light soaking. The limit between extrinsic and intrinsic is given by $\sigma_n^+/\sigma_n^o = \sigma_p^-/\sigma_p^o \approx 50$.

a) T_{set}	b	$\mu^o\tau^o$ [cm^2/V]	α_{CPM}(1.2eV)
120°C	64 (8)	$5.7\cdot10^{-8}$ ($2.4\cdot10^{-9}$)	0.9 (24)
140°C	80 (8)	$8.9\cdot10^{-8}$ ($3.1\cdot10^{-9}$)	1.0 (16)
150°C	**46 (15)**	**$4.2\cdot10^{-8}$ ($6.1\cdot10^{-9}$)**	**1.4 (6)**
160°C	376 (11)	$1.2\cdot10^{-7}$ ($7.7\cdot10^{-9}$)	0.3 (12)
170°C	**136 (20)**	**$1.9\cdot10^{-7}$ ($1.6\cdot10^{-8}$)**	**0.9 (6.5)**
180°C	320 (9)	$1.7\cdot10^{-7}$ ($8.3\cdot10^{-9}$)	0.4 (10)
200°C	303 (13)	$2.6\cdot10^{-7}$ ($1.8\cdot10^{-8}$)	0.2 (12)
220°C	**175 (26)**	**$3.5\cdot10^{-7}$ ($3.6\cdot10^{-8}$)**	**0.4 (4)**
270°C	**355 (19)**	**$3.5\cdot10^{-7}$ ($4.8\cdot10^{-8}$)**	**0.4 (3.5)**
320°C	**283 (28)**	**$3.6\cdot10^{-7}$ ($4.8\cdot10^{-8}$)**	**0.4 (4)**

a) T_{set} indicates the setpoint temperate. Actual substrate temperature is about 20°C (T_{set}=150°C) to 60°C (T_{set}=320°C) lower than the setpoint temperature.

Table I. Temperature series: Properties of 2.5 μm thick a-Si:H layers in the annealed state and in the degraded state (latter in brackets). Samples in bold correspond to the "high temperature series".

*) T_{set} of i-layer	η [%]	FF	jsc [mA/cm^2]	V_{OC} [V]
120°C	6.9 (1.1)	0.60 (0.30)	13.5 (4.9)	0.850 (0.786)
140°C	7.2 (2.3)	0.65 (0.35)	13.4 (8.1)	0.825 (0.796)
150°C	**7.1 (3.2)**	**0.55 (0.37)**	**16.2 (11.2)**	**0.788 (0.787)**
160°C	8.9 (3.1)	0.66 (0.38)	15.6 (10.2)	0.859 (0.816)
170°C	**9.6 (4.9)**	**0.65 (0.46)**	**16.5 (12.7)**	**0.852 (0.828)**
180°C	9.1 (3.7)	0.69 (0.41)	15.4 (11.0)	0.855 (0.830)
200°C	9.7 (5.4)	0.71 (0.48)	16.0 (13.5)	0.851 (0.826)
220°C	**10.3 (6.5)**	**0.67 (0.52)**	**18.0 (15.1)**	**0.848 (0.835)**
270°C	**9.5 (6.7)**	**0.65 (0.54)**	**18.0 (15.2)**	**0.827 (0.821)**
320°C	**8.3 (6.5)**	**0.60 (0.52)**	**17.6 (15.9)**	**0.781 (0.785)**

Table II. Temperature series: solar cell performances in the annealed state and in the degraded state (latter in brackets). The cells in bold correspond to the "high temperature series".

If we look at the layers first and we plot the b value as a function of the deposition temperature (fig. 2.9) we obtain the usual picture of undoped and annealed a-Si:H, namely a slight n-type behaviour indicated by b values around 200, where the limit between intrinsic and extrinsic material is given by the ratio of capture cross sections $\sigma_n^+/\sigma_n^o = \sigma_p^-/\sigma_p^o \approx 50$ (see

ch. 2.2.1). Only the samples deposited at very low temperatures turn out to be truly midgap with b values around 50, a fact which can be explained by the high dangling bond density in such material (as seen by CPM) which "pull" the Fermi level towards midgap.

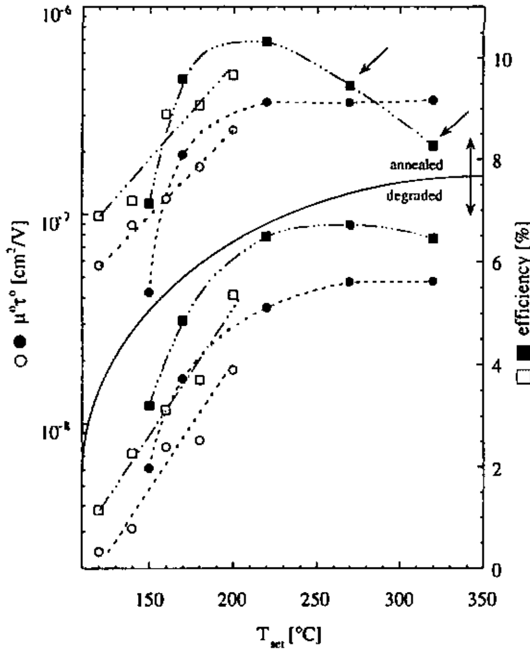

Fig. 2.10. Correlation between the $\mu^o\tau^o$ products evaluated on two series of 2.5 µm thick, undoped layers, on one side, and efficiencies of solar cells incorporating the "same" material as an i-layer on the other side; results are given for both the annealed and the degraded state. The two cell efficiencies for high-temperature deposition (as marked by arrows) are presumably reduced due to interdiffusion problems.

The quality of the layers, as shown by $\mu^o\tau^o$, is almost constant at temperatures above 220°C whereas it strongly falls off for temperatures below. Such behaviour is also reproduced in CPM measurements which indicates an enhancement of deep defect density for low-temperature samples. If we look now at the high temperature series (bold in values in table II), this effect observed by CPM is, however, much weaker than the measured deterioration of the film quality seen by the $\mu^o\tau^o$ product. From this discrepancy between CPM and $\mu^o\tau^o$ we deduce that the band mobility (seen by $\mu^o\tau^o$ but not by CPM) is considerably inferior (2-3 times) in low-temperature material compared to a-Si:H deposited above 220°C. Additional support of this

suggestion is also given by the characteristic energy E_0 of the Urbach edge, in a-Si:H generally associated to the disorder in the material [i.e. Cody 92], which increases from 49 meV (270°C) to 56 meV (150°C). Goerlitzer et al. [Goerlitzer 95] came to the same results from the analysis of transient photoconductivity data measured on the same series of samples.

For the cells a similar deterioration of the performances with decreasing temperatures is observed. On the other side also the performances of cells deposited at high temperatures are lowered even though the a-Si:H material was shown to be of good quality. Nevertheless, at these high temperatures, interdiffusion problems may become important and even dominate the overall efficiency of the solar cell. In accordance with this hypothesis, the j_{sc} which remains high even for high deposition temperatures, does not indicate any deterioration of the intrinsic layer material.

2.3.3. The light soaked state

The results obtained on layers and cells in the degraded state are listed in brackets in table I and II respectively; the same data is represented graphically in fig. 2.10.

In the degraded state for all a-Si:H layers the b values are strongly reduced by light soaking and all the samples are now, according to our definition given above, truly intrinsic (midgap) with b values < 50 (see fig. 2.9). In other terms, following the guidelines given in 2.2, the quality of all the a-Si:H layers of these two series is simply given by the photoconductivity in the light-soaked state. CPM measurements performed after degradation show, here again, a less pronounced increase at low temperatures compared to the deterioration of $\mu^o\tau^o$ products.

The conversion efficiencies η of the corresponding cells were strongly reduced by light-soaking. One particularity, which is worth to be mentioned here, is once more the behaviour of the high temperature cells. They degrade much less (only about 20%) than the other cells which may lead to the **wrong** conclusion that the a-Si:H material used for these cells is more stable than a-Si:H deposited at lower temperatures. In fact, the $\mu^o\tau^o$ products determined on the corresponding layers clearly show that a-Si:H materials deposited at more than 270°C are actually not more stable as a-Si:H deposited at e.g. 220°C. The reason for the apparent higher stability of these two cells lies in their structural deficiencies; the interdiffusion problems "artificially" reduce the cell efficiencies in the annealed state but they become insignificant in the light soaked state, where the cell performances are then limited by the degraded, defect rich i-layer.

2.3.4. Correlation between layer properties and cell performances

The $\mu^o\tau^o$ products measured on layers and the corresponding solar cell conversion efficiencies η of both series are plotted as a function of each other in fig. 2.11 in order to visualise the correlation between the two. In the same graph we also represented the data obtained in the light-soaked state, even though cells and layers were degraded differently. The

fig. 2.11 must therefore be interpreted as two independent graphs which show an incidental agreement.

The correlation obtained between $\mu^o\tau^o$ products of the layers and the corresponding solar cell efficiencies is very good and even exceeded our expectations. Especially in the degraded state the correlation is excellent: the structural deficiencies of the cells have lost their relative importance and the cell performances are exclusively governed by the strong recombination losses in the i-layer here. On the other hand, for high quality a-Si:H material ($\mu^o\tau^o > 1\cdot 10^{-7}$ cm^2/V) the correlation with cell performances is less evident as other loss mechanisms related to the cell structure (e.g., interdiffusion at high temperature, see ch. 2.3.2 and 2.3.3) gain relative importance and can even determine the overall cell conversion efficiency.

Looking at fig. 2.11 one can conceptually also imagine a curve (upper limit) which would indicate the maximum conversion efficiency η achievable with a-Si:H material of a given quality. First, this curve would help to immediately estimate the potential of any a-Si:H material, to be incorporated in a p-i-n device. And second, for any produced p-i-n cell with known i-layer material properties, one could easily discriminate between material related losses and an imperfect cell structure (assuming $\sigma^{\pm}/\sigma^{o}$ to be constant in all a-Si:H materials).

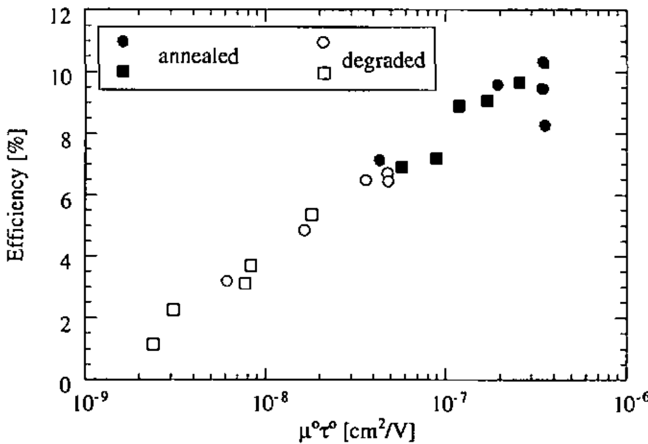

Fig. 2.11. Correlation between $\mu^o\tau^o$ products evaluated on two series (squares and circles) of layers and the corresponding solar cell efficiencies in the annealed and in the degraded state. Note that the cells and layers were degraded differently and thus the graph must be considered to be composed of two independent parts: annealed state (full symbols) and degraded state (open symbols).

2.4. Conclusions

The quest for a suitable correlation parameter lead us to the creation of a new parameter, the $\mu^0\tau^0$ product. This $\mu^0\tau^0$ product unites all the desired properties of a correlating tool: On one side, $\mu^0\tau^0$ contains the important informations about band mobility and deep defect density, both crucial parameters for the operation of p-i-n devices; on the other side it is independent on the prevailing dangling bond occupation in the a-Si:H material. We could show that $\mu^0\tau^0$ can indeed be deduced from experimental $\mu\tau$ products measured by steady-state methods (SSPC and SSPG). We proposed a procedure, which allows an easy evaluation of $\mu^0\tau^0$ from SSPC and SSPG measurements using a single equation (2.5). Thereby, the evaluation of $\mu^0\tau^0$ from experimental data becomes particularly simple in most cases [Beck 94]: if the a-Si:H material has an extrinsic character, the quality of the material is monitored by the ambipolar diffusion length and the measurement of photoconductivity in this case does not supply any relevant information about the material quality. Undoped, but slightly n-type a-Si:H typically fits in the annealed state in this category. The opposite is true, however, for clearly intrinsic (midgap) a-Si:H material, i.e. for degraded a-Si:H. Here, the photoconductivity alone is sufficient to accurately describe the material properties. The measure of the parameter b is thereby always a good way to determine if an a-Si:H material is intrinsic or extrinsic.

The application of our "correlation tool" to two series of a-Si:H layers and corresponding p-i-n solar cells lead to promising results: the correlation obtained between the $\mu^0\tau^0$ products on a-Si:H films (and evaluated in the manner described here), on one side, and the performances of the solar cells incorporating the same material as an active i-layer, on the other side, is very good [Beck 96-1].

However, one should always keep in mind the complexity of a solar cell device which includes doped layers, contacts, interfaces etc. The $\mu^0\tau^0$ products presented here exclusively takes into account the properties of the intrinsic i-layer and the related losses by recombination. It may thus only be used to optimise solar cell performances as far as the intrinsic layer is concerned.

3. THIN FILM MICROCRYSTALLINE SILICON: A SHORT INTRODUCTION

Microcrystalline silicon is a thin film material which consists of small crystalline grains (typically between 50 Å and 1000 Å) embedded in an amorphous matrix as illustrated in fig. 3.1. The first microcrystalline silicon layer was deposited by Vepřek and Mareček in 1968 [Vepřek 68], using chemical vapour transport in a hydrogen plasma at 600°C. In the following years Vepřek and his co-workers improved their deposition technique and performed pioneering work in the investigation of this new material.

Later on also many other research groups joined the field of thin film microcrystalline silicon, exploring thereby the entire arsenal of growth methods. As "The diversity of growth methods available represents a real flowering of the ingenuity of scientists and engineers." (Citation [Fahrenbruch 83]), a large variety of thin film silicon materials of very different morphologies and qualities was the result.

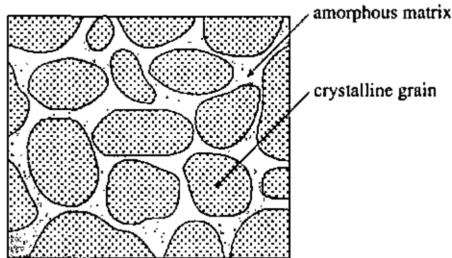

Fig. 3.1. Illustration of microcrystalline silicon: the material is composed of small crystallites which are embedded in an amorphous matrix. Typical grain sizes range from 50 Å - 1000 Å.

The most commonly used method to produce microcrystalline silicon is, however, the Chemical Vapour Deposition (CVD) process at both, low and high temperatures. Thereby, the process temperature plays an important role. In the high-temperature and low pressure CVD (used e.g. by [Jackson 83], [Seto 75], [Podbielski 84]) the process gases are decomposed thermally at about 650°C, whereas at low temperatures (~200°C) the gas decomposition is driven by a plasma discharge (PE-CVD, GD). Silicon layers produced by high-temperature CVD contain practically no hydrogen; they are usually referred to in the literature as "polycrystalline silicon" [Jackson 83], [Seto 75]. On the other side, low-temperature PE-CVD material contains substantial quantities of hydrogen and are in literature often denominated as

"hydrogenated microcrystalline silicon" (µc-Si:H), although sometimes the term "nanocrystalline silicon" is also used [Konuma 87]. This nomenclature has mainly historic reasons. In fact, high-temperature CVD "polycrystalline" silicon does not necessarily have larger grains than low-temperature µc-Si:H. We will use this terminology throughout this work even though recently a new terminology, based on the size of the crystalline grains rather than on the deposition technique, was proposed to the photovoltaic community [Basore 94].

3.1. Properties of hydrogenated microcrystalline silicon

A "typical" poly- or microcristalline material does not exist. If one has to attribute to this material a characteristic feature, it is probably the fact that its morphology and its properties can be tuned in a wide range, either by the choice of the deposition method or, for a given method, by simply changing the deposition parameters. For instance, the transition from amorphous to µc-Si:H material, which is usually achieved by highly diluting silane into hydrogen (e.g. [Wang 90], [Beck 96-3]), can also be induced e.g. by applying a substrate bias [Konuma 87], by increasing the deposition temperature [Wang 90], or by rising the input power [Torres 97].

Variations on the crystalline volume fraction, on orientations and forms of crystallites and different average densities of impurity atoms (e.g. oxygen), defects and porosity makes it, thus, very difficult to compare poly- and microcrystalline materials obtained by different deposition techniques. In this work we will therefore concentrate on hydrogenated microcrystalline silicon and, therein, on µc-Si:H materials deposited by the Very High Frequency Glow Discharge (VHF-GD) [Curtins 87] as this method has been shown to have some advantages over other deposition techniques (e.g. lower radical energies and higher deposition rates [Keppner 96]).

A cross-sectional TEM picture showing the structure of a typical µc-Si:H layer deposited on glass by the VHF-GD technique at 110 MHz [Meier 94] is represented in fig. 3.2. One can discern elongated grains parallel to growth direction. An indication for the "cigar-like" shape of the crystallites is also given by the X-ray diffraction spectroscopy measurements; they show a strongly enhanced <220> X-ray diffraction peak (when compared to a silicon powder sample) (see fig. 3.3.), indicating, thus, preferential growth in the <220> direction [Keppner 96]. The crystalline volume fraction X_c, deduced from Raman spectroscopy, exceeds 90% in high-quality material and indicates that actual no amorphous tissue is present in these layers. The grain sizes as evaluated from X-ray diffraction by Scherrer's formula are about 200 Å; however the precise meaning of this value is not clear yet, because of the elongated form of the grains (Scherrer's formula is based on a model that assumes spherical grains). The hydrogen content can be estimated from IR absorption measurements and is typically about 6 % which will be shown to be far enough to efficiently passivate the defects at the grain boundaries (see ch. 4.2.2).

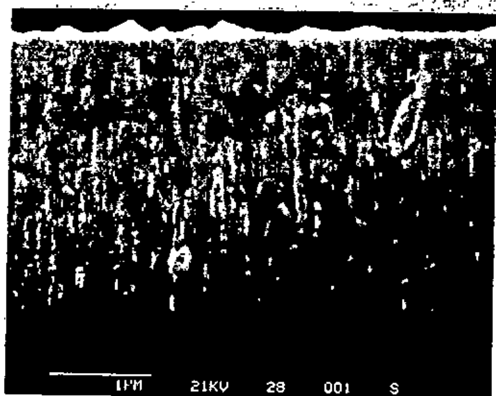

Fig. 3.2. Cross-sectional TEM picture of a μc-Si:H layer deposited on a glass substrate by the VHF-GD technique: preferential growth is obtained, leading to elongated grains and a very high crystalline volume fraction.

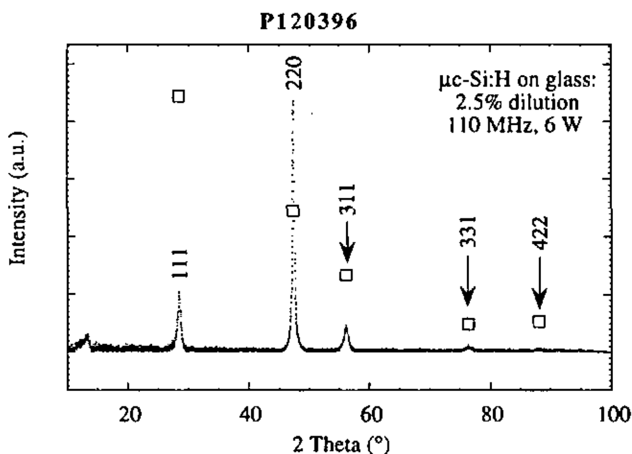

Fig. 3.3. X-ray diffraction pattern of an undoped μc-Si:H layer deposited on glass. For comparison the five most important refraction peaks of a c-Si powder sample are plotted in arbitrary units (o). In the μc-Si:H layer the <220> reflection peak is clearly enhanced, this indicates a preferential growth of the crystallites in the <220> orientation.

Even though it seems that we are able to give a rather precise picture of µc-Si:H material as obtained by VHF-GD, this holds only for the "standard" high quality µc-Si:H produced in our lab (IMT, Uni Neuchâtel). Even slight variations in the deposition parameters, e.g. an increase of the plasma excitation frequency, variations in the dilution ratio of silane into hydrogen or in the power density often immediately lead to substantial changes in the structure of the deposited layer. This fact makes the characterisation of µc-Si:H an even more difficult task as it will be extensively discussed in the following two chapters.

3.2. Microcrystalline silicon for solar cell applications

Even though microcrystalline silicon has been discovered approximately at the same time as a-Si:H, more than twenty years passed by until this material was for the first time incorporated into a solar cell and the result published [Wang 90].

On one side, the preconceived idea of a very small-grained µc-Si:H silicon material containing a huge amount of defect-rich grain boundary regions may have hindered the development of µc-Si:H based solar cells for a long time. In fact, by different characterisation methods, defect densities as high as 10^{17} - 5×10^{18} cm^{-3} were measured in µc-Si:H materials ([LeComber 83], [Amato 92], [Liu 93]), defects which were supposed to favour the carrier recombination losses in the material.

On the other side, also a number of other technological problems had to be solved in order to clear the way to operating µc-Si:H solar cells:

1) As-grown µc-Si:H has a pronounced n-type character due to oxygen contamination and, thus, cannot directly be used as an active intrinsic i-layer in a µc-Si:H p-i-n solar cell. First attempts to solve this problem were made by Lucovsky et al. [Lucovsky 93] who added small traces of diborane to the gas phase in order to compensate the native n-type behaviour of the µc-Si:H material. Refined by Meier et al. [Meier 94], this delicate process of microdoping was, however, recently replaced by a purifying technique of the feed gas, reducing thereby the oxygen contamination to an insignificant level [Torres 96].

2) The development of doped microcrystalline layers, initiated by [Usui 79], leaded to n- and p-contact layers whose quality nowadays exceeds that of doped a-Si:H layers as far as the conductivity is concerned [Prasad 91], [Flückiger 93].

3) The problem of defect-rich grain boundary regions is closely related to the deposition technique and the process parameters used. In fact, this problem has two aspects: first, broken Si - Si bonds can be created during growth when the µc-Si:H tissue is constructed. However, and this is the other aspect, broken bonds can also be passivated by hydrogen, either during or after growth. A deposition technique suited to produce low-defect "solar grade" µc-Si:H material must therefore not only allow a

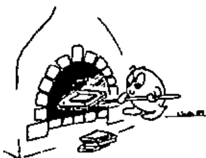

"careful" construction of the μc-Si:H tissue during growth, but also involve enough hydrogen to passivate the remaining defects.

It has been shown that the Very High Frequency Glow Discharge (VHF-GD) technique at 70 MHz is particularly favourable for the growth of μc-Si:H material [Finger 94]. In fact, compared to the conventional 13.56 MHz GD, the ion bombardment energies (supposed to introduce defects in the growing layer) are lower in the VHF-GD process [Heintze 96] and the atomic hydrogen flux to the surface of the growing layer (which is supposed to be important for defect passivation) is enhanced [Heintze 96].

These reasons may be responsible for the important role played today by the VHF-GD method in the field of μc-Si:H solar cells. After some isolated approaches presented in the past ([Wang 90], [Faraji 92]), Flückiger et al. [Flückiger 92] published the first μc-Si:H p-i-n cell produced by VHF-GD with 1.7 % conversion efficiency. Since then the μc-Si:H solar cells were steadily improved. They presently reach a conversion efficiency of 7.7 % [Meier 96] and considerable potential to increase this efficiency unquestionably exists. In combination with a thin a-Si:H top cell ("micromorph tandem cell") a stable efficiency of 10.7 % has been achieved so far [Keppner 96].

4. OPTICAL PROPERTIES OF HYDROGENATED MICROCRYSTALLINE SILICON

From the optical point of view, the main reason why μc-Si:H became an interesting material for thin film solar cells is its enhanced optical absorption, when compared to a-Si:H, in the region of near infrared light (between 1.1 eV and 1.7 eV). Related to the crystalline phase in the material (with optical gap ~ 1.1 eV), this high infrared absorption is a common feature of all μc-Si:H and predestinates it to be used as a low-gap material for solar cell applications.

More particular are the optical absorption properties of μc-Si:H prepared by the VHF-GD. The optical absorption in these materials is further enhanced and exceeds that of c-Si over the whole spectral range. This fact attracted large interest as the observed 2 to 4 times higher absorption (compared to c-Si) immediately allows the reduction of the cell thickness by the same factor while still absorbing the same amount of sunlight. The physical processes which lead to such high absorption were, however, initially unclear and motivated us to investigate in this problem.

Another important aspect which was also included in our investigations is the sub-bandgap absorption (below 1 eV), the latter being an indicator for the defect density. Normally high in μc-Si:H, the defect-connected absorption has for a long time prevented scientists to implement their μc-Si:H materials into p-i-n solar cells. In contrast to this the VHF-GD μc-Si:H (which lead to solar cells with high efficiencies) often shows an extremely low defect-connected absorption. As such a low defect density is strongly favourable for solar cell applications, we, thus, paid special attention to this part of the absorption spectrum.

Starting with the measurement of the optical absorption properties of different VHF-GD μc-Si:H materials, we then suggest several possible explanations which can account for the observed behaviour and we checked them - if possible - experimentally. We thereby realised that scattering (bulk and surface) in μc-Si:H layers is clearly enhanced compared to a-Si:H and can mask in certain cases the "true" absorption given by the material properties. In the following we, thus, developed different experimental techniques which allow a quantitative determination of the scattering coefficient in our μc-Si:H materials over several orders of magnitude and to separate scattering effects from the "true" optical absorption. The "tools" being now prepared, a re-examination of the absorption spectra on a larger variety of μc-Si:H materials should, however, be considered in future as some open questions still remain.

4.1. Optical absorption measurement techniques

We measured the optical absorption of μc-Si:H by the three different techniques: by Transmission / Reflection measurements (T/R), by the Photothermal Deflection Spectroscopy (PDS) and by the Constant Photocurrent Method (CPM). Combining these three techniques, we were able to obtain an almost complete picture of the optical absorption in our μc-Si:H material.

4.1.1. Transmission and Reflection measurements (T/R)

In T/R measurements the transmittance T and the reflectance R of the layer-substrate system as a function of wavelength are measured by a spectrometer. By further using an integrating sphere (Ulbricht sphere), one can discern between **specular** and **diffuse** transmission and reflection respectively. In contrast to a-Si:H, the detection of the diffuse signal can become important in the μc-Si:H material as it will be shown in ch.4.3.

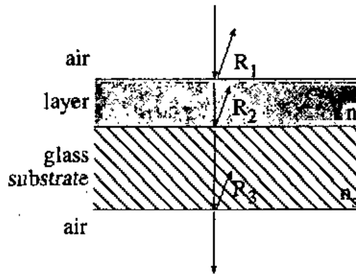

Fig. 4.1. The optical system "flat μc-Si:H layer on glass substrate" as used for transmission and reflection measurements. For an incident light beam hitting perpendicularly the surface, the surface and interface reflections R_1, R_2 and R_3 are given by the indexes of refraction of the layer n, the substrate n_s and the air (n = 1).

The measured transmittance is determined for a given layer-glass substrate system (fig. 4.1) by:

$$T = \frac{(1-R_1)(1-R_2)(1-R_3)\exp(-\alpha d)}{1-R_1R_2\exp(-2\alpha d)} \tag{4.1}$$

and therefrom the absorption coefficient α can be evaluated:

$$\alpha = -\frac{1}{d}\ln\left[\frac{-B \pm \sqrt{B^2-4AC}}{2A}\right] \tag{4.2}$$

where

$$A = R_1 R_2 T$$
$$B = (1 - R_1)(1 - R_2)(1 - R_3) \tag{4.3}$$
$$C = -T$$
$$d = layer\ thickness$$

The reflection coefficient R_3 (air-glass interface) is about 4% for the for visible light, the reflection coefficients R_1 can be measured directly and R_2 can be estimated by measuring the reflectance R_{glass} from the glass side (in the region of strong absorption):

$$R_2 \approx \frac{R_{glass} - R_3}{(1 - R_3)^2} \tag{4.4}$$

By such T/R measurements the absorption coefficient α of the μc-Si:H material can be determined in the range free of interference fringes and of strong absorption.

4.1.2. Photothermal Deflection Spectroscopy (PDS)

For the PDS measurement [Jackson 82-2] the sample is immersed in a non-absorbing liquid (CCl_4) with an index of refraction which strongly depends on the temperature. The sample is then illuminated by monochromatic light and the absorption by the μc-Si:H material is traduced into a local heating of the CCl_4. The change of index of refraction of the CCl_4 due to the local temperature increase can be read out by the deflection of a HeNe laser beam which travels through the CCl_4 close to the surface of the sample. The deflection signal of the laser beam is proportional to the absorption coefficient α for homogeneously absorbed light and can be used as a relative measure of α. To put the absorption spectrum to absolute scale, the PDS measurement is self-calibrated in the region of strongly absorbed light (or by T/R measurements).

The PDS technique, in contrast to CPM measurements, is sensitive to all optical transitions. Furthermore it is somehow less sensitive to scattering effects as the read-out zone, determined by the width of the laser beam, is very restricted. On the other side, the PDS technique has the disadvantage to be limited in the low absorption region by residual absorption of the glass substrate ([Amato 91], [Nonomura 94]). For μc-Si:H layers with thicknesses of about 2 μm the PDS detection limit is about $\alpha \approx 1\ cm^{-1}$.

4.1.3. The Constant Photocurrent Method (CPM)

The CPM method has been introduced to a-Si:H by Vaněček et al. [Vaněček 81] and allows the determination of very small absorption coefficients. The technique is based on the photoconductivity σ_{ph} which is in a-Si:H as well as in μc-Si:H related to the generation rate by a power law ([Rose 63], [Goerlitzer 96]):

$$\sigma_{ph} \propto G^{\gamma} \tag{4.5}$$

For uniform absorption ($\alpha d \ll 1$) the generation rate G is approximately proportional to $\alpha\Phi_0$ where Φ_0 is the incident light flux and one can write:

$$\sigma_{ph} \propto (\alpha\Phi_0)^{\gamma} \tag{4.6}$$

Keeping now during the measurement the photocurrent constant by adjusting the light intensity one can determine a **relative** absorption spectra according to:

$$\sigma_{ph} = const. \qquad \Rightarrow \qquad \alpha \propto \frac{1}{\Phi_0} \tag{4.7}$$

However, for that this simple approach is valid, several conditions, such as $\mu\tau$ products and γ factor independent of wavelength, must be fulfilled. These conditions were studied in detail by Mettler [Mettler 94] for a-Si:H, but no similar studies were made so far for μc-Si:H. This is the reason why we applied the CPM technique to μc-Si:H only in combination with PDS in order to dispose of a more reliable picture of the absorption behaviour.

Another important point are the optical transitions detected by the CPM technique. The measured signal in CPM is a photocurrent which is carried by the majority carriers. In the subbandgap absorption region CPM is thus only sensitive to transitions from localised states to the band of majority carriers (conduction band in n-type material and valence band in p-type material) as illustrated in fig.4.2 for an n-type material.

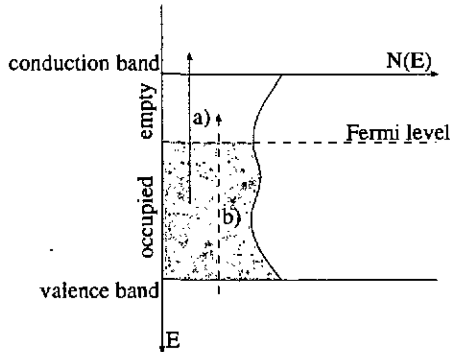

Fig. 4.2. Optical transitions as detected by the CPM and PDS technique: whereas PDS is sensitive to all optical transitions, CPM only "sees" transitions from localised states to the band of majority carriers (transition (a) in an n-type material), but is in this case "blind" for the transition (b). Possible transitions between localised states are not represented here.

The absorption spectra measured by CPM is **relative** and must be calibrated by another technique such as PDS or T/R to obtain the absolute absorption spectra. However, recently the "absolute CPM" method (A-CPM) has been introduced by Vaněček et al. [Vaněček 95]. By measuring simultaneously standard CPM as well as the transmission spectra of the sample one can evaluate the **absolute** absorption spectra of thin layers without involving further calibration measurements. An additional credit point of this method is the suppression of interference fringes in the absorption spectra which can be a problem in thin samples ($d \leq 1$ μm). A detailed description of the method is given elsewhere [Vaněček 95]. If not mentioned differently, the CPM spectra presented in this section are determined by this "absolute CPM" (A-CPM) method.

4.2. The optical absorption in μc-Si:H

The typical absorption spectra of different silicon-based materials are represented for comparison in fig. 4.3. The absorption spectra of c-Si [Green 95] shows a parabolic shape related to the indirect nature of the fundamental optical gap at 1.12 eV. The poly-silicon material (p-type wafer with grain sizes ~ 5 mm) basically has the same absorption behaviour as c-Si, but a detrimental amount of defects appear in the gap due to unpassivated grain boundaries. Contrary to this, the optical gap of a-Si:H is enlarged to around 1.7 eV (Tauc gap) due to the disorder in this material. Its absorption in the region of visible light is strongly enhanced compared to the other materials as the k-selection rule (contribution of a phonon with a certain energy to the absorption process) is relaxed.

The shape of the absorption spectra of a high-quality μc-Si:H layer deposited by the VHF-GD, in its turn, follows the shape of c-Si over a wide range of energy, but is shifted to lower energies and higher absorption values. Both, the enhancement and the shift of the absorption edge are important advantages for the application of μc-Si:H material in p-i-n solar cells. In fact, the shift of the absorption edge makes it possible to absorb infrared light of even lower energies, and, furthermore, the overall enhancement of the absorption coefficient allows one to make considerably thinner cells which still absorb the same quantity of light.

The reasons for this absorption behaviour can be manifold [Beck 96-2]. On one side, a residual amorphous phase in the μc-Si:H material may increase the absorption in the region of visible light, but it cannot account for the enhanced absorption below 2 eV. On the other side, a distortion of the band structure of the crystalline phase, e.g. due to internal stress or quantum confinement (small crystallites), may lead to a shift of the optical gap. Furthermore, also the "grainy" structure of the material and a rough surface may lead to scattering effects which can distort the measured absorption spectra. We will address all these possible effects in the following chapters, paying thereby particular attention to the problem of scattering in VHF-GD μc-Si:H (ch. 4.3).

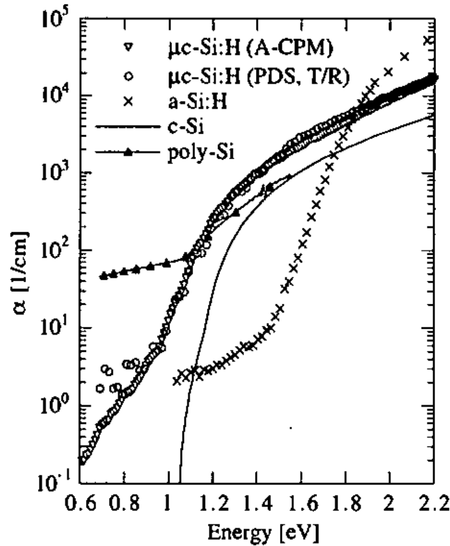

Fig. 4.3. Absorption coefficient of VHF-GD μc-Si:H compared to c-Si [Green 95], a-Si:H and a p-type poly-silicon wafer. The absorption of μc-Si:H has almost the same shape as c-Si, but is shifted to higher values and lower energies.

The defect-connected absorption in the μc-Si:H produced by the VHF-GD is usually very low and suggests an efficient passivation of the grain boundary defects by hydrogen. We fully confirmed this presumption experimentally for our μc-Si:H material; the result will be presented hereafter.

4.2.1. "Optical tuning" of μc-Si:H

Before stepping further we would like, however, to remind that no "standard" absorption spectrum for μc-Si:H exists, but that the optical absorption properties of μc-Si:H critically depend on the deposition conditions used. To illustrate to what extent the absorption properties of μc-Si:H can be tuned by varying the deposition parameters, we measured by PDS, A-CPM and T/R the absorption spectra of a series of μc-Si:H layers, all deposited at 110 MHz (deposition temperature 220°C, HF-power 7 W, pressure 0.8 mbar, using a gas purifier). The only variable parameter was the ratio of silane flow over total gas flow $[SiH_4]/[SiH_4+H_2]$ which was increased from 1.25% to 7.5%. High dilution thereby means little silane is left in hydrogen (1.25%) whereas in low-dilution samples the silane content in the total gas flow is increased (7.5%). The obtained layers had thicknesses between 1 μm and 3.1 μm which

corresponds to deposition rates between 0.44 Å/s and 3.5 Å/s. The measured absorption spectra are plotted in fig. 4.4.

As already shown by Kroll et al. [Kroll 96], the transition from μc-Si:H to a-Si:H is abrupt and typically takes place at around 7.5% for the deposition conditions used here. In the series presented here, the 7.5% sample is clearly amorphous whereas all the other layers are microcrystalline. Thereby, three distinct effects can be observed:

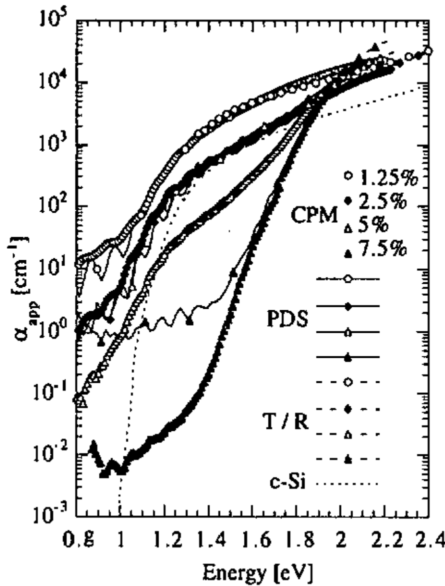

Fig.4.4. Apparent optical absorption coefficient α_{app} measured on the 110 MHz dilution series by PDS, A-CPM and T/R. The transition from amorphous to microcrystalline silicon takes place at around 7.5% dilution. Crystalline silicon data [Green 95] is plotted for comparison. The absorption of the highly diluted sample (1.25%) is enhanced by scattering.

First, the most drastic phenomenon is of course the transition from a-Si:H with a Tauc gap of around 1.7 eV to μc-Si:H, showing the characteristic indirect gap transition of crystalline silicon at about 1.1 eV. There are, however, also significant changes in the absorption curve within the microcrystalline range of deposition conditions.

As a second effect, for the sample with the highest dilution (1.25%), further enhancement of optical absorption by scattering is observed. As scattering events at the surface or in the bulk of the layer result in a longer effective optical path of the photons, the apparent absorption is enhanced. The problem of scattering in μc-Si:H will be addressed in more detail in ch. 4.3.

Third, the layer produced with 5% dilution is a mixed phase material, containing a non-negligible amorphous fraction. This is reflected as an important difference between A-CPM and PDS data. Whereas PDS measures the true optical absorption, the CPM technique fails here as the photosensitivities and $\mu\tau$ products of the amorphous tissue and the crystalline grains are not the same and thus one of the basic conditions for CPM is not fulfilled.

4.2.2. Defect-connected absorption

A high defect-density, as observed for most μc-Si:H ([LeComber 83], [Amato 92], [Liu 93]) and polycrystalline silicon [Jackson 83] materials, was for many years the main argument why this material was not incorporated into solar cells. The situation has turned out to be more advantageous, however, for μc-Si:H deposited by the VHF-GD. As shown in fig. 4.5, the defect-connected absorption in high-quality μc-Si:H materials deposited by the VHF-GD is very low and reaches values of about $\alpha = 1\ cm^{-1}$ on the shoulder (0.8 eV). Applying the procedure (commonly used for a-Si:H) proposed by Jackson et al. [Jackson 83], who compared the integrated defect-connected absorption with the spin density (determined by ESR) in his polycrystalline material, this low absorption observed in VHF-GD μc-Si:H corresponds to a defect density of about $5 \times 10^{15}\ cm^{-3}$ only.

The most obvious assumption to explain the low defect density in our μc-Si:H is that the VHF-GD technique allows a very **efficient passivation of the grain boundary defects by hydrogen**. This situation is in clear contrast to polycrystalline silicon produced by high temperature CVD where the defect-connected absorption is very pronounced as high process temperatures render a passivation of the grain boundary defects impossible. Note, however, that post-deposition hydrogenation is possible in these materials as has been shown e.g. by Jackson et al. [Jackson 83] who annealed CVD polycrystalline silicon in atomic hydrogen.

To demonstrate experimentally this important role for passivation played by the ~6 % of hydrogen in our μc-Si:H material we performed an experiment opposite to the post-deposition annealing done by Jackson et al. We stepwise annealed an as-grown midgap μc-Si:H layer in an ultra pure molecular hydrogen atmosphere for 2 hours at temperatures between 300°C and 500°C. The hydrogen, which initially saturated the defects at the grain boundaries, was by this treatment evolved out of the μc-Si:H film and the grain boundary defects - now unpassivated - appear as a prominent shoulder in the region of subbandgap absorption (see fig. 4.5). In addition, also a slight but measurable increase of the absorption in the region of visible light is observed when the hydrogen content is reduced as shown in the inset of fig. 4.5. The origin of this enhancement is still not clear but indicates that the absorption in this spectral region is indeed somehow connected to the grain boundary region.

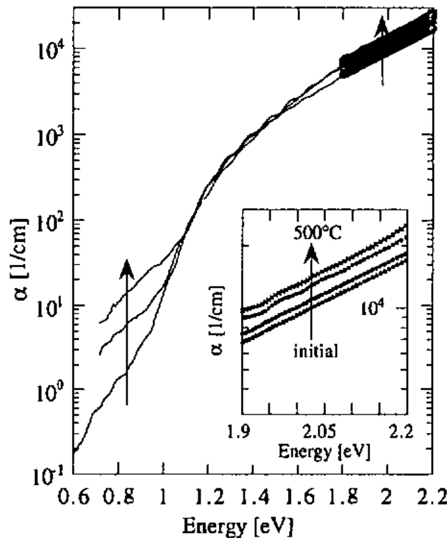

Fig. 4.5. Evolving the hydrogen out of the μc-Si:H layer by stepwise annealing in ultra pure molecular hydrogen up to 500°C leads to a prominent increase of the defect connected absorption and to a slight, but measurable increase of the absorption in the region of visible light (shown in the inset).

4.2.3. Red shift of the indirect optical gap

Thanks to the very low subbandgap absorption in our μc-Si:H material, the shape of the absorption edge becomes clearly visible: α(E) follows a square root dependence on photon energy E which is characteristic also for monocrystalline silicon [Green 95] (Fig. 4.6). Hence, we attribute this absorption edge in μc-Si:H to the indirect optical transition from the top of the valence band ($\Gamma_{25',V}$) to the minimum of conduction band ($\Delta_{1,C}$) with the assistance of phonons, as for crystalline silicon. This hypothesis is further supported by the unchanged absorption edge between 1.1 and 1.4 eV with hydrogen evolution (see fig. 4.6). Representing $\sqrt{\alpha}$ as a function of energy, a straight line as for c-Si is obtained and an indirect gap, E_g, of about 1.02 eV for this sample can be deduced. Compared to the indirect gap of 1.12 eV in c-Si, the gap in VHF-GD μc-Si:H material is, thus, shifted by about 0.1 eV to the infrared. The origin of this red shift is not clarified yet, but different effects may be involved such as scattering, quantum confinement and stress.

As our μc-Si:H material is constituted of crystallites of small dimensions, a possible quantum confinement effect should be taken into consideration. However, it has been shown by

several authors who investigated in porous silicon (PS) that quantum confinement leads to a blue shift of the absorption edge ([Sagnes 93]) rather than to a red shift. Furthermore, quantum confinement was observed so far only for crystalline structures smaller than about 50 Å [Sagnes 93]. The crystallites in our μc-Si:H material (~200 Å) are, thus, too large for that quantum confinement effects could be expected.

On the other side, X-ray diffraction experiments with a $CuK_{\alpha 1}$ source on VHF-GD μc-Si:H revealed and enhanced interatomic Si-Si spacing of 5.46 Å in μc-Si:H compared to the lattice constant of 5.43088 Å in c-Si. This fact indicates important tensile strain within the crystallites which leads to a distortion of the band structure. Studies about the effect of pressure on c-Si indeed found measurable changes in the band gap minima [Paul 61] and data on non-stress relieved monocrystalline silicon shows a shift of α(E) towards the infrared compared to stress relieved c-Si [Saritas 87]. More recent theoretical investigations on strained silicon grown on Si_xGe_{1-x} substrates [Tserbak 95] came also to the conclusion that tensile strain splits up the usually degenerated valence band maxima as well as the conduction band minima, leading thereby to a red shift of the fundamental indirect absorption edge. However, more experimental evidence will be necessary here to corroborate this hypothesis.

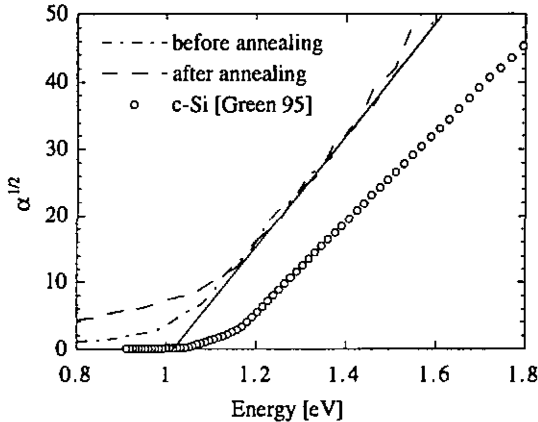

Fig. 4.6. Square root dependence of the absorption coefficient of μc-Si:H in comparison with crystalline silicon. The optical gap of μc-Si:H is red-shifted by about 0.1 eV and does not depend on the hydrogen content in the layer.

In a heterogeneous material such as μc-Si:H scattering effects must unquestionably be considered. The enhancement of the optical path by scattering events results in an increase of the apparent absorption which could manifest itself also by a red shift of the evaluated optical

gap. Scattering in solids being a complex problem, it will be examined in some detail hereafter. We will show that scattering is indeed much more important in μc-Si:H than in a-Si:H and certainly contributes to a certain extent to the observed gap shift. However, its influence varies from one sample to the other and at present it is premature to draw a clear picture of the influence of scattering on the absorption edge of high quality μc-Si:H materials with little defects.

4.3. Scattering effects in μc-Si:H

As scattering effects in μc-Si:H can distort the measured absorption spectrum and, thus, mask the "true" absorption properties of μc-Si:H materials, the problem of scattering will be addressed in more detail in this chapter.

Scattering in solids can be due to **surface roughness** and local variations of the index of refraction in the bulk. Both influence the optical path of the light and introduce a perturbation to the phase of the light wave. If the size of the scattering elements A is small compared to the wavelength ($A \leq \lambda/10$), Rayleigh scattering which is characterised by a $1/\lambda^4$ dependency of the scattered intensity, can be observed. For bigger scatterers ($A \approx \lambda$), Mie scattering dominates and the variation of the scattered intensity with the wavelength is lower. The scattered intensity is thereby determined by the size of the scatterers, by their number and by the relative index of refraction of the scatterer with respect to the surrounding medium [VandeHulst 57].

The contribution of scattering to the measured absorption of light can be quantified by the scattering coefficient α_{sc}. The latter forms, together with the optical absorption coefficent α, the extinction coefficient α_e:

$$\alpha_e = \alpha + \alpha_{sc} \tag{4.8}$$

α_e is deduced from T/R measurements (without integrating sphere) and contains both light loss mechanisms, absorption and scattering.

The other optical absorption measurement techniques used in this work (T/R with integrating sphere, PDS and A-CPM) all measure an **apparent absorption α_{app}(E)**. The apparent absorption contains, again, the contributions of both, absorbed **and** scattered light, but the influence of scattered light on the detected signal is more complicated in these cases as will be discussed later in this chapter.

It is, however, important to note here that the apparent absorption coefficient $\alpha_{app}(E)$ reflects the absorption properties of a μc-Si:H layer and gives, thus, direct information about the absorption behaviour of this material when incorporated into a solar cell. Hence, the experimentally measured apparent absorption $\alpha_{app}(E)$ is of direct practical importance for the optimisation of μc-Si:H material for solar cells.

On the other side $\alpha_{app}(E)$ corresponds to the "true" optical absorption coefficient $\alpha_a(E)$ (given by the specific properties of the μc-Si:H material such as band structure, bandgap or defect states) **only** in the case when scattering effects are negligible over the whole spectral range. If scattering effects are important, additional experiments are necessary in order to evaluate the contribution of scattering to the measured $\alpha_{app}(E)$ and to deduce therefrom the "true" optical absorption of a given μc-Si:H material.

As μc-Si:H is a heterogeneous material scattering effects may a priori not be neglected. Scattering may be caused by the crystallites (size 50 - 200 Å) embedded in an amorphous-like surrounding as well as by vacancies, voids and cracks in the material. Furthermore, μc-Si:H can have a rough layer surface, depending on the deposition parameters and the film thickness [Iqbal 83], which also will scatter the light falling on the sample.

To estimate the influence of scattering on the measured absorption spectra $\alpha_{app}(E)$ we adopted the following strategy. Assuming a power law dependency on energy, the spectral dependence of the scattering coefficient $\alpha_{sc}(E)$ can be written as:

$$\alpha_{sc} = \alpha_0 \cdot E^{\zeta} \tag{4.9}$$

where α_0 is the scattering coefficient at 1 eV. In μc-Si:H materials with optically smooth growth surface the power law exponent ζ will achieve 4 (bulk scattering of Rayleigh type only [VandeHulst 57]), whereas for μc-Si:H films with rough surface the ζ will be reduced ($2 < \zeta < 4$) due to non-negligible surface scattering [Bass 95].

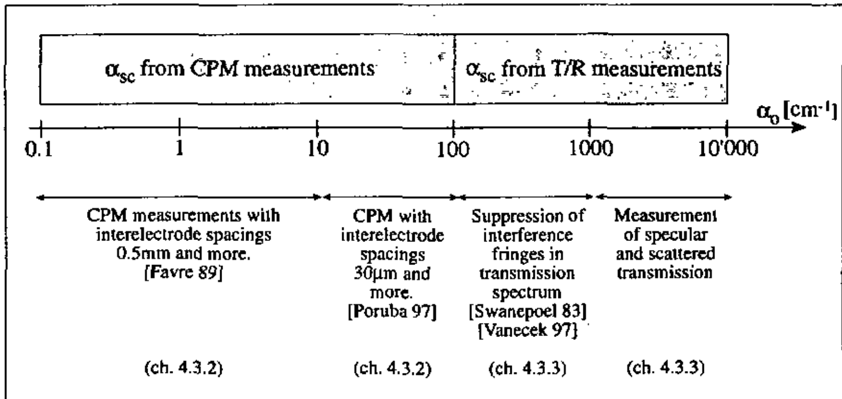

Fig. 4.7. Inventory of the experimental methods which can be used for the evaluation of scattering in μc-Si:H layers for different magnitudes of scattering coefficient α_0 (= α_{sc} at 1 eV).

We determined the power law exponent ζ by measuring the intensity of backscattered light in the region of visible and UV light as will be described in the following chapter 4.3.1. Once ζ is known, it is sufficient to determine α_{sc} at one energy point in order to evaluate $\alpha_{sc}(E)$ over the whole spectral region of interest. However, as scattering in μc-Si:H materials can vary over many orders of magnitude no experimental method is powerful and sensitive enough to determine scattering in all cases. We will, thus, propose hereafter four different techniques, each of them covering a certain range of scattering (see fig. 4.7), for the determination of α_{sc} in μc-Si:H.

4.3.1. Diffuse reflection from μc-Si:H layers with rough surface

In contrast to a-Si:H material, μc-Si:H layers sometimes look "milky" and always present important diffuse back-scattering in the region of visible and near ultraviolet light which is due to the surface roughness of our μc-Si:H layers. We thus measured the surface topology of different μc-Si:H films with a surface profiler (α-Step) and compared it to a-Si:H. The obtained results are represented in fig. 4.8 and clearly reveal the rugged character of the surfaces of certain VHF-GD μc-Si:H layers. μc-Si:H materials obtained under non-standard conditions (e.g. P200296 prepared at 130 MHz with very high dilutions of silane into hydrogen) tend, however, to have especially rough surfaces whereas the high quality μc-Si:H materials presently used in good μc-Si:H solar cells have usually a surface roughness similar to the layer P160296.

On the other side, the suppression of the specular reflectance for the benefit of the diffuse reflection due to a rough surface can also be calculated analytically. For a surface with a Gaussian roughness distribution, it has been shown by Filínski [Filínski 72] that the attenuation of the specular reflection is given by:

$$\frac{R_r}{R_s} = exp\left(-\Delta\phi_R^2\right) = exp\left[-\left(\frac{4\pi\sigma n_o}{\lambda}\right)^2\right] \tag{4.10}$$

where R_S is be the specular reflection that would have a perfectly flat surface (given by Fresnel's law) and where R_r is the specular part of reflection measured from the rough surface. $\Delta\Phi_R$ is the roughness induced phase shift of the reflected light beam, n_o the index of refraction of the medium where the reflection takes place ($n_o = 1$ for air) and σ is the r.m.s. value of the surface roughness.

The ratio between the measured specular part of reflection R_r and R_S (measured total reflection with integrating sphere) on the amorphous and microcrystalline layers of fig. 4.8 are shown in fig. 4.9 and fitted by expression 4.10. The values for the surface roughness σ thereby deduced correlate very well with the previously obtained surface profiles of fig. 4.8 and thus confirm a direct relationship between the back-scattered light intensity and the surface roughness.

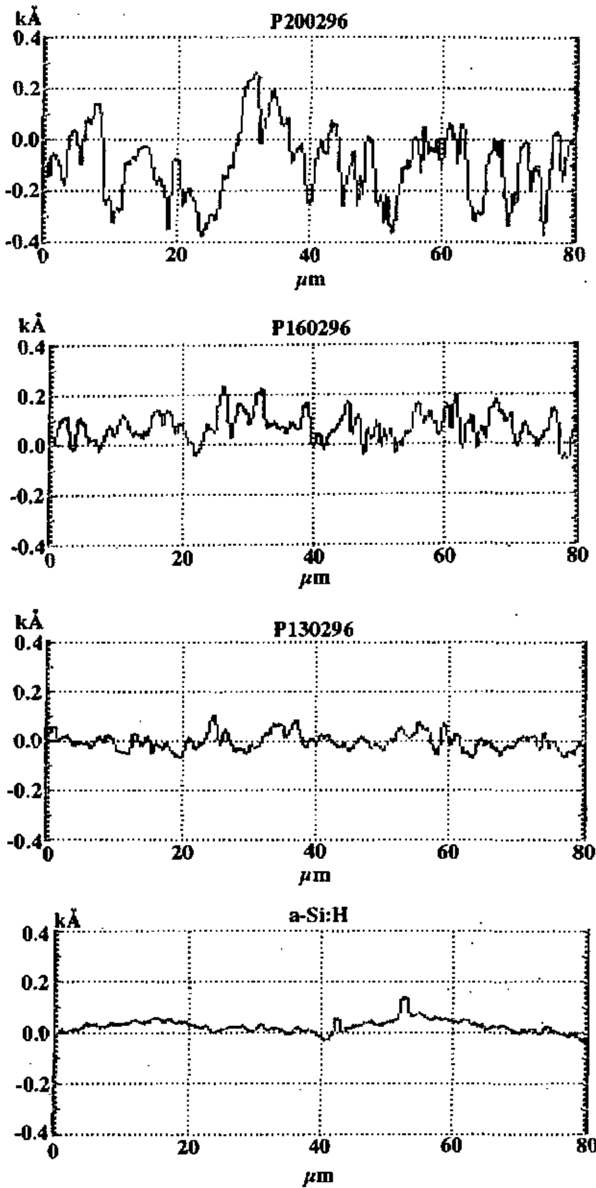

Fig. 4.8. Surface topology of three μc-Si:H and one a-Si:H film measured by an α-step surface profiler. Whereas the surface of a-Si:H is optically flat, the μc-Si:H layers show a more or less pronounced surface roughness, depending on the deposition conditions used.

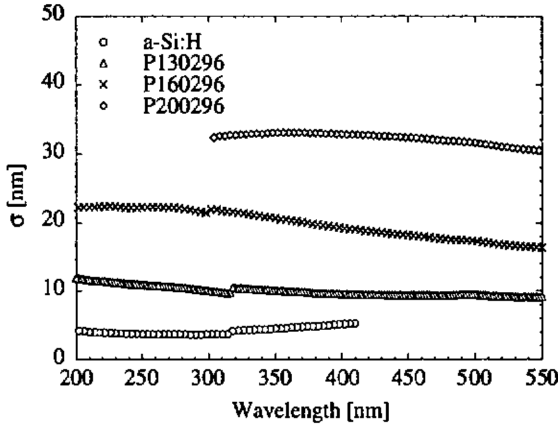

Fig. 4.9. Surface roughness σ deduced according to equation 4.10 from total reflectance (R_s) and the specular reflectance (R_r) measurements for the four samples from fig. 4.8.

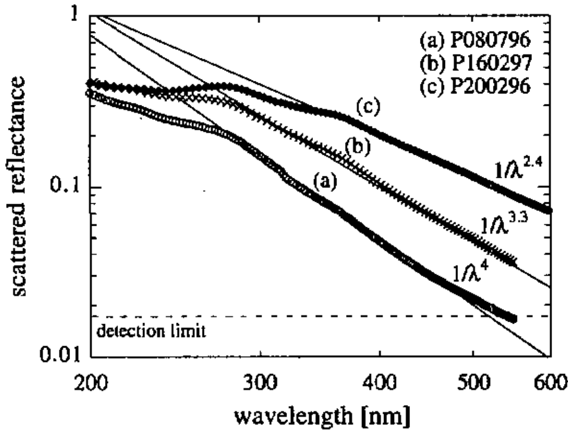

Fig. 4.10. Backscattered light intensity measured on a mirrorlike μc-Si:H layer (P080796) and on two μc-Si:H samples which look slightly "milky" to the eye (P160296 and P200296). The $1/\lambda^4$ dependency observed on the smooth sample indicates bulk scattering of Rayleigh type. The power law exponent of the "milky" samples is reduced as surface scattering becomes dominant.

The increase of the backscattered light intensity with wavelength is shown in fig. 4.10. Whereas the µc-Si:H layer P080796 is mirrorlike ($\sigma \approx 16$ nm), the other samples have an increasingly rough surface (see fig. 4.8) and a "milky" appearance. For the sample with optically smooth surface a $1/\lambda^4$ dependency of the diffuse reflection is observed, indicating, thus, that scattering in this sample is of Rayleigh type (small scatterers) and dominated by the bulk properties (small voids etc.). For the sample with very rugged surface (P200296) the diffuse backscattering is further enhanced by surface scattering and the power law exponent is reduced here to about $\zeta = 2.4$.

4.3.2. Scattering measured by CPM

For µc-Si:H materials with weak scattering ($\alpha_0 \leq 100$ cm^{-1}) the CPM can be used to determine the scattering coefficient in the region of low absorption. Developed by Favre et al. [Favre 89] for a-Si:H, the method consists of measuring the absorption spectrum by CPM using samples with different interelectrode spacings (fig. 4.8).

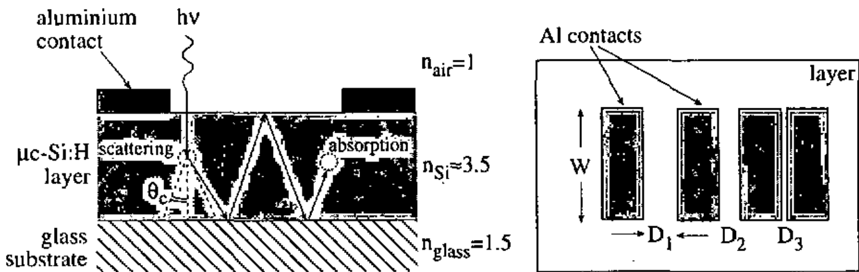

Fig. 4.11. Schematical picture of scattering in a thin µc-Si:H layer with waveguiding properties (left): a photon which is scattered into an angle > θ_c remains confined in the layer and is finally absorbed. If the photon is absorbed within the contacts it contributes to the photocurrent, otherwise it is not "seen" by the CPM technique. By varying the contact configuration (right picture) the contribution of scattered light to the CPM signal can be regulated and the scattering coefficient α_{sc} can be evaluated (see text).

Thereby, one part of the light penetrating into the layer is directly absorbed, but another part is scattered in the film. Due to the waveguiding properties of a silicon layer (index of refraction: $n_{Si} \approx 3.5$, $n_{glass} = 1.5$, $n_{air} = 1$), most of the scattered light will travel along the layer and will finally be absorbed. If the scattered photon is absorbed **within** the illuminated area between contacts (fig. 4.11), it will contribute to the photocurrent and enhance the

measured absorption. By changing the contact configuration, more or less of these scattered photons will be absorbed, allowing, thus, an evaluation of the contribution of scattered photons to the total absorption.

The theoretical calculations have already been presented elsewhere [Favre 89]. In order to be able to express the absorbed light intensity (including scattering) analytically, three *assumptions must be fulfilled:*

1) $\alpha_a D \leq 1,\ \alpha_a W \leq 1$
2) $\alpha_{sc} D \leq 1,\ \alpha_{sc} W \leq 1$
3) *scattering is isotropic*

These assumptions state that the scattering coefficients α_{sc} estimated by this method will only be valid for the spectral region of low absorption and low scattering (propagation distance between two scattering events larger than W and D).

The ratio of the absorbed light intensity I_a to the incident intensity I_0 can then be expressed as:

$$\frac{I_a}{I_0} = \underbrace{(1-\alpha_{sc}d)\alpha_a d}_{(1)} + \underbrace{\frac{\alpha_{sc}d}{WD}\int dF \int S(\Omega)\left[1-exp\left(-\alpha_a R(W,D,\Omega)\right)d\Omega\right]}_{(2)} \qquad (4.11)$$

where (1) is the part of light which is directly absorbed and (2) is the part which is only absorbed after being scattered once. By further simplifying the interface reflections and the quadratic term $\alpha_{sc}d\cdot\alpha_a\cdot d$ the following result is obtained [Favre 89]:

$$\alpha_{CPM} = \alpha_a + X(W,D)\alpha_{sc}\alpha_a \qquad (4.12)$$

$$X(W,D) = \frac{1}{\pi} ln\frac{1+cos\,\theta_c}{1-cos\,\theta_c}\cdot\left[\frac{D}{4} ln\frac{1+sin\,A}{1-sin\,A} + \frac{W}{2}\left(\frac{\pi}{2} - A\right)\right] \qquad (4.13)$$

where θ_c is the critical angle for total reflection (≈25° at 1 eV) and A=arctg(W/D).

This CPM technique as described here allows the evaluation of weak scattering in in the range of $0.1 < \alpha_0 < 10\ cm^{-1}$. Typical values of α_{sc} in a-Si:H prepared by the VHF-GD were found to be around $2\ cm^{-1}$ in the region of dangling bond absorption (1.2 eV) [Favre 89], [Vaněček 90].

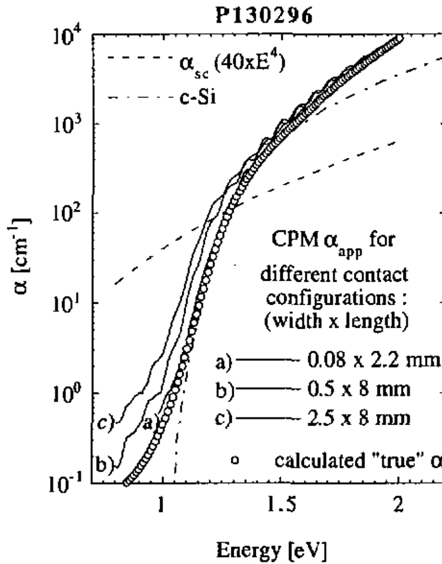

Fig. 4.12. Apparent absorption of a "mirror-like" µc-Si:H layer (P130296) measured by CPM with three different contact configurations [Poruba 97]. Whereas for the larger contacts (a) and (b) the apparent absorption is enhanced due to scattering, the measurement with contacts having a very narrow gap (c) corresponds almost to the "true" optical absorption. The curve referred as to calculated "true" absorption (open circles) is deduced according to an extended theory, taking also into account multiple scattering in the layer [Poruba 97].

The absorption spectra measured on µc-Si:H with different interelectrode spacings clearly show an influence of scattering on the measured defect absorption and indicate considerably enhanced scattering in this material as compared to a-Si:H [Beck 96-3]. However, a more precise determination of α_{sc} has been so far problematic as even for the usually smallest electrode configuration used (D=0.5 mm, W=8 mm) the assumption (2) was not fulfilled and all scattered light was absorbed within the contact area. Only recently the development of "microscopic" metal contacts (D=30 µm, W=2.2 mm) by Poruba and Vaněček [Poruba 97] allowed a quantitative measurement by CPM of α_{sc} in µc-Si:H with medium scattering in the range between **$10 < \alpha_o < 100$ cm^{-1}**. Furthermore, the simple theory presented above was completed by taking into account also multiple scattering events. First measurements on VHF-GD µc-Si:H material show that this improved CPM for the evaluation of scattering is especially suited for µc-Si:H layers with optically smooth surfaces where bulk scattering is

dominating. A bulk scattering coefficient of about $\alpha_0 = 40\ cm^{-1}$ was thereby determined in a μc-Si:H layer with smooth layer surfaces [Poruba 97] (fig. 4.12). However, in near future and with the help of this new technique, more measurements need to be performed on μc-Si:H materials in order to deduce the characterisitic features in the "true" absorption spectrum of μc-Si:H (free of scattering effects) and to answer the question about the observed red shift of the optical gap in VHF-GD material.

4.3.3. Scattering measured by specular and diffuse T/R

The easiest way to detect relatively strong scattering (**$\alpha_0 > 100\ cm^{-1}$**) in μc-Si:H material is to look at the interference fringes of the transmission spectra at wavelengths where the μc-Si:H is transparent. If scattering is weak or negligible, the maxima of the transmission curve are determined by the glass substrate only [Swanepoel 83]:

$$T_{max} = \frac{2n_s}{n_s^2 + 1} \tag{4.9}$$

where n_s is the index of refraction of the substrate and n that of the μc-Si:H layer. The transmission minima are given by the properties of both, the μc-Si:H layer and the glass substrate and can, thus, be used for the determination of the index of refraction of the μc-Si:H material [Swanepoel 83]:

$$T_{min} = \frac{4n^2 n_s}{n^4 + n^2(n_s^2 + 1) + n_s} \tag{4.10}$$

Assuming an index of refraction of about 1.5 for the glass substrate, the maxima should attain 92 % of transmission, the minima around 40 % (depending on the index of refraction of the μc-Si:H material). If, however, a non-negligible part of the light is scattered by the μc-Si:H layer the contrast of the interference fringes is reduced.

Note, that also thickness inhomogeneities can also lead to a similar reduction of the amplitude of the interference fringes [Swanepoel 84]; the influence of the latter can, however, be reduced by illuminating a small spot of the layer surface only.

In fig. 4.13 we plotted the transmission spectra measured on two of our μc-Si:H layers. For the layer (a) which has been shown to have smooth surface (see fig. 4.8) the transmission extrema reach the values predicted by theory. This means that in this μc-Si:H film scattering is far too weak ($\alpha_0 < 100\ cm^{-1}$) in order to be detected by this method. On the other side, for the μc-Si:H sample (b) the modulation of the interference fringes is clearly reduced due to important scattering. Hence, for this sample the scattering coefficient α_{sc} can be calculated in the region where μc-Si:H is transparent (below 1.1 eV) from the geometric mean $T_{geom} = \sqrt{T_{max} \cdot T_{min}}$ of the transmission spectrum [Swanepoel 83], taking into account the spectral variation of the

index of refraction n_{Si}. A scattering coefficientof about 250 cm^{-1} (at 1 eV) was deduced for the sample P160296 [Poruba 97].

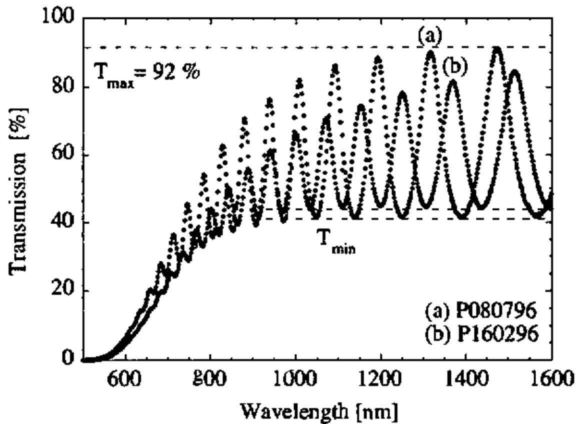

Fig. 4.13. Measured transmission of two μc-Si:H layers of comparable thickness. Layer (a) looks mirrorlike to the eye and shows almost perfect interference fringes, whereas layer (b) has a "milky" aspect and exhibits reduced interference fringes due to scattering.

For μc-Si:H layers with extremly rough growth surface, surface scattering can become very important, resulting in scattering coefficients α_0 **> 1000 cm^{-1}** ($= \alpha_{sc} > 5000$ cm^{-1} at 2 eV). For such rather unusual μc-Si:H materials scattering can be detected quite simply by measuring the the **specular** and **scattered** transmission spectrum of such μc-Si:H layers.

To measure the specular transmission we placed the radiation detector at some distance behind the sample in the axis of the incident light beam and recorded its attenuation by the layer (fig. 4.14). The transmission signal T_{spec} is given by the part of penetrating light which is **not** scattered and **not** absorbed and can be expressed as:

$$T_{spec} = (1-R_1)(1-R_2)(1-R_3)exp(-\alpha d)exp(-\alpha_{sc} d) \qquad (4.14)$$

where R_1, R_2 and R_3 are the reflection coefficient of the surfaces and interfaces (see fig. 4.1), α the absorption coefficient, α_{sc} the scattering coefficient and d the μc-Si:H layer thickness.

In a second run an integrating sphere (Ulbricht sphere) is placed directly behind the sample in order to collect both, the specular **and** scattered transmitted light intensity T_{tot} (fig. 4.14). Deducting therefrom the specular part of transmission T_{spec}, the scattered transmission T_{scat} is obtained. T_{scat} is composed of the part of the light which is scattered into a small angle which does not allow total reflection ($\theta < \theta_c = 23°$) and which is not absorbed:

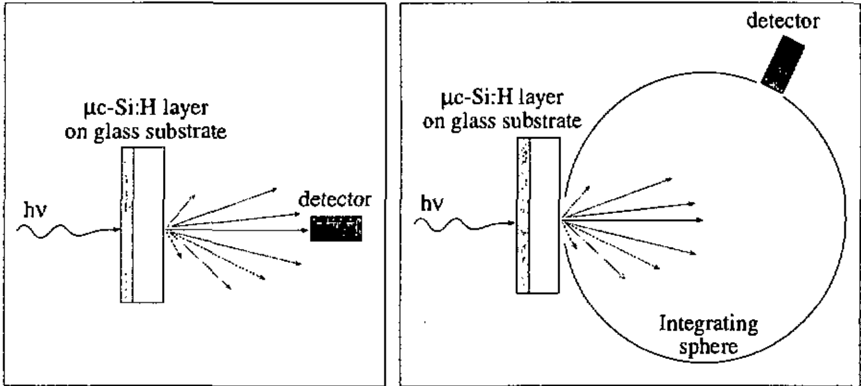

Fig. 4.14. Experimental set-up for specular transmission (a) and total transmission measurements (b).

$$T_{scat} = (1-R_1)(1-R_2)(1-R_3)\exp(-\alpha d_{eff})[1-\exp(-\alpha_{sc} d)]C_\theta \qquad (4.15)$$

where $d_{eff} = d/\cos\theta \approx d$ for scattering angles smaller than θ_c. C_θ is given by $(1 - \cos\theta_c)$ and represents the fraction of space, delimited by the cone of the total reflection angle θ_c, which does not allow the scattered photon to be totally reflected and absorbed. Assuming $n_{Si} \approx 3.9$ (at 2 eV) in this spectral region, C_θ is about 0.08 (for the escape cone given by the silicon - glass interface). Note, however, that C_θ strongly depends on the index of refraction of μc-Si:H (and its variation with energy). As so far we have no precise knowledge about n(μc-Si:H), the latter will limit the precision of this method.

Combining both equations 4.14 and 4.15, the scattering coefficient α_{sc} can be deduced:

$$\frac{T_{scat}}{T_{spec}} \approx C_\theta[\exp(+\alpha_{sc} d) - 1] \qquad (4.16)$$

In fig. 4.15 the transmission spectra of a μc-Si:H layer with high surface roughness (see fig. 4.8) measured with and without integrating sphere are shown. The difference between T_{tot} and T_{spec} in the region free of interference fringes was then used to calculate α_{sc} according to equation 4.16 and the result is plotted in the same figure. In agreement with diffuse reflection measurements (see fig. 4.10) a spectral dependency of the scattering coefficient $\alpha_{sc} \sim E^{2.5}$ is obtained and an α_0 value of 1600 cm^{-1} is deduced. In this region of strong absorption the absorption coefficient and scattering coefficient add linearly ($\alpha_{app} = \alpha + \alpha_{sc}$) and therefore scattering will influence in this particularly hazy μc-Si:H sample (produced by highly diluting silane in hydrogen) the apparent absorption in the whole energy region represented here.

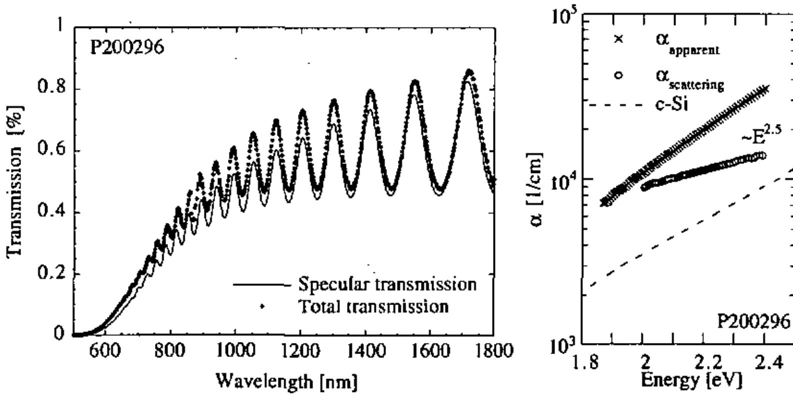

Fig. 4.15. Specular transmission and total transmission measured on a highly diluted μc-Si:H sample which shows strong scattering (P200296). The scattering coefficients α_{sc} deduced from these measurements are shown in the picture on the right side in comparison to the measured apparent absorption coefficient α_{app}.

4.4. Conclusions and outlook

We have measured the optical absorption properties in VHF-GD μc-Si:H materials with the help of the Constant Photocurrent Method, the Photothermal Deflection Spectroscopy and Transmission/Reflection measurements between 0.6 eV and 2.5 eV. We thereby observed enhanced optical absorption, compared to crystalline silicon, over the whole spectral range together with a shift of the absorption edge to the infrared by about 0.1 eV. Furthermore, our measurements confirm a very low defect-connected absorption in our high quality VHF-GD material (less than 1 cm^{-1} at the shoulder at 0.8 eV) which was demonstrated to be the result of an almost perfect passivation of the grain boundaries by hydrogen. Note, that this value can be considered as an upper limit as the influence of scattering is most important in this spectral region of very low absorption.

The enhanced and extended absorption of light combined with a very low defect density in our high quality VHF-GD material is strongly favourable for solar cell applications as it allows an important reduction of the cell thickness while still absorbing a major part of the sunlight. The physical processes governing these rather uncommon absorption properties of VHF-GD μc-Si:H material turned out, to be manifold and at the present stage of the knowledge not all of them can be explained. As scattering effects in μc-Si:H layers are clearly enhanced (compared to a-Si:H) and therefore may mask the "true" material-related optical absorption properties (given by band structure, band gap etc.) a foregoing study of scattering in μc-Si:H became necessary.

Four experimental techniques were developed which allow a quantitative evaluation of the scattering coefficient in μc-Si:H layers. We thereby found that both, the rough growth surface as well as the μc-Si:H bulk material (voids) can give rise to measurable scattering. Depending on the deposition conditions used, the evaluated scattering coefficient can vary in a wide range (α_{sc}(1 eV) ≈ 50 - 2000 cm^{-1}).

The influence of scattering on the measured absorption spectra is still subject of investigation. However, some trends can already be drawn from our measurements:

Scattering contributes at least partially to the observed red shift of the optical gap although other reasons such as important internal strain could not be excluded so far. The enhancement of the optical absorption in the region of visible light can neither be explained by the remaining amorphous fraction (usually ≤ 10%) in the μc-Si:H material nor by scattering. Further work will be necessary here in order to clarify if a relaxation of the k-selection rule for silicon atoms situated on the grain surfaces can account for this effect.

5. ELECTRICAL PROPERTIES OF HYDROGENATED MICROCRYSTALLINE SILICON

This last section will be devoted to the study of the transport properties in μc-Si:H. As for μc-Si:H we cannot at present have recourse to established characterisation methods nor transport models (as is the case for the more extensively studied a-Si:H); our approach here will be, however, more basic. Furthermore, in order to keep the complexity within a reasonable limits, we will restrict ourselves in this work to the study of electrical transport in **dark** conditions.

We will start with some characteristics of the dark conductivity of μc-Si:H material and present the grain boundary trapping model which is widely used to describe the electrical transport in polycrystalline silicon.

We will then for the first time apply the Time of Flight (TOF) technique to μc-Si:H material in order to monitor the carrier transport parallel to the growth direction. However, as μc-Si:H is a new material, a foregoing re-examination of the experimental conditions was necessary. We will then present first measurements of drift mobilities and $\mu\tau$ products on μc-Si:H layers and cells by TOF; we will furthermore "scan" the "gap" of μc-Si:H for defects by post-transient TOF. The preliminary results obtained so far demonstrate the potential of the TOF technique for the characterisation of μc-Si:H.

5.1. Introduction

Several researchers have already investigated the electrical transport properties in poly- and microcrystalline silicon. They studied the variation of the dark conductivity (and of the Hall mobility) with the incorporation of dopants (phosphine or diborane) in polycrystalline silicon with unpassivated grain boundaries [Seto 75], [Podbielski 84] and in μc-Si:H, where the use of low-temperature deposition processes allows for a more efficient passivation of the grain boundary defects by hydrogen ([LeComber 83], [Konuma 87], [Lucovsky 93], [Flückiger 95]). Even though the studied materials had various structures and qualities, their electrical transport exhibits a similar characteristic behaviour which was explained by the **grain boundary trapping model**, introduced by Seto [Seto 75].

However, the dark conductivity and Hall measurements draw in our opinion only an uncomplete picture of the electrical transport properties in μc-Si:H. They do not give any information about the carrier lifetimes even though these are of paramount importance for the operation of a p-i-n solar cell. Furthermore, the measurement of the Hall mobility in midgap μc-Si:H with low dark conductivity (the material which is of interest for solar cell applications)

is still problematic, and its interpretation, also, is not at all straightforward. In fact, the Hall mobility is, for the sake of simplicity, usually identified with the band mobility. This may be a valid approximation for extrinsic materials, but it becomes questionable in the case of intrinsic μc-Si:H where no type of carrier clearly prevails.

In this work we followed up a somehow different approach. We used the rather standard determination of the dark conductivity as an estimate of the contamination level in the studied μc-Si:H materials, but above all we performed mainly Time of Flight (TOF) measurements. TOF has the advantage to monitor the carrier transport parallel to the growth direction and, furthermore, TOF can be performed directly on solar cell devices. It can give precious information about the drift mobility and the mobility-lifetime product of electrons and holes, information which is lacking from dark conductivity measurements. Furthermore, the extension of the TOF experiment to longer times (posttransient TOF) allowed us to trace the electrically active defects in the gap of the μc-Si:H material.

5.2. The dark conductivity of μc-Si:H

The measurement of the dark conductivity (σ_d) is probably the easiest experimental test to obtain a first information about a semiconductor layer (provided that ohmic contacts are available). Applying an electric field E to the sample, the free electrons and holes experience a force e·|E| and start to move. This transport of carriers under the influence of the electric field gives rise to a drift current density which can be measured:

$$j_{drift} = \sigma \cdot E, \tag{5.1}$$

where σ is the conductivity defined as:

$$\sigma = \left(\mu_n^0 n_f e + \mu_p^0 p_f e\right) \tag{5.2}$$

and where $\mu_n{}^0$ and $\mu_p{}^0$ are the band mobilities of electrons and holes, n_f and p_f the free carrier densities in the dark and e the elementary charge.

Experimentally, σ_d is measured as a function of temperature and often exhibits a single activated behaviour over the studied temperature range:

$$\sigma_d = \sigma_o \cdot exp\left(-\frac{E_{act}}{kT}\right) \tag{5.3}$$

where σ_0 is called "dark conductivity prefactor", E_{act} is the dark conductivity activation energy and kT is the thermal energy.

In polycrystalline silicon with unpassivated grain boundaries, the dark conductivity has its minimum value for undoped material where the defect-rich grain boundary regions pin the Fermi level down to midgap. If dopant atoms are added to the material, the conductivity starts to

rise, at first very gradually, but then showing suddenly a pronounced steep increase at a characteristic doping concentration (around 2×10^{18} cm^{-3} in [Seto 75]).

The situation is, however, different in μc-Si:H deposited by low-temperature processes, where hydrogen can indeed almost completely passivate the grain boundary defects (see fig. 4.5). As the Fermi level pinning is much less pronounced in these μc-Si:H layers, the dark conductivity becomes here a much more sensitive monitor for the impurity contamination level here. This is the reason why as-grown, undoped μc-Si:H exhibits a n-type character which is caused by incorporated oxygen impurities [Vepřek 83], [Torres 96]. To overcome this undesired n-type behaviour, small traces of diborane can be added to the gas phase in order to compensate this "oxygen doping" [Lucovsky 93], [Flückiger 95], [Meier 96]. This compensation is accompanied by a decrease in the room temperature dark conductivity, the latter reaching a minimum value in the lower 10^{-7} $(\Omega cm)^{-1}$ range and a maximum activation energy of ~ 0.54 eV for μc-Si:H layers deposited by the VHF-GD technique (see fig. 5.1. - data reprinted from [Meier 96]).

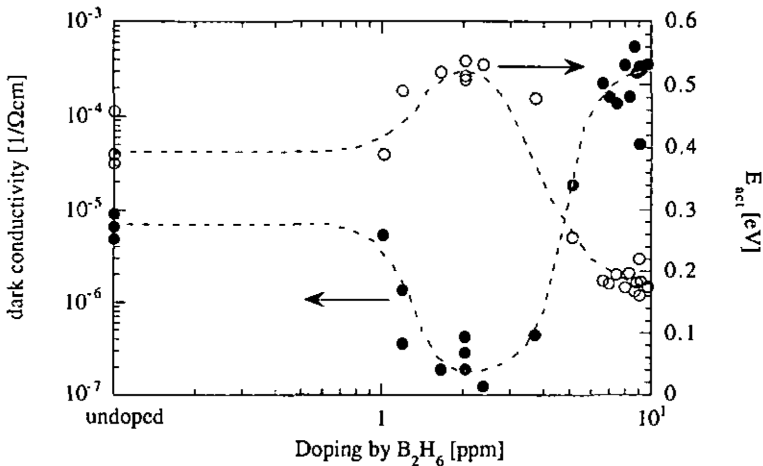

Fig. 5.1. Dark conductivity and corresponding activation energy as a function of boron doping for a series of VHF-GD μc-Si:H deposited at 110 MHz (data replotted from [Meier 96]): the as-grown n-type character of μc-Si:H can be compensated by the incorporation of small amounts of boron in the material.

The other approach to overcome the n-type character of μc-Si:H is to reduce the oxygen content in the material to an insignificant level. In c-Si the maximum solubility of oxygen is

about 2-3×10^{18} cm^{-3} [Möller 93]. For concentrations up to this value, oxygen atoms can occupy an interstitial position between two silicon atoms where they are electrically inactive. If the oxygen content exceeds this value, oxygen starts to replace silicon atoms in the lattice (creating thereby a donor level at E_C - 0.17 eV) and introduces various oxygen-vacancy complexes which give rise to electrically active defects in the gap of c-Si. The µc-Si:H material deposited by the VHF-GD technique typically contains around 1×10^{20} cm^{-3} of oxygen atoms (by SIMS). However, the installation of a gas purifier in the feed gas line can drastically reduce the oxygen contamination of the silane gas and thereby its incorporation into the growing µc-Si:H layer. Controlling at the same time the outgasing rate from the reactor walls, Torres et al. [Torres 96] have shown that the oxygen content can be reduced by this technique to about 3×10^{18} cm^{-3}, and that dark conductivity values as low as 2×10^{-7} 1/Ωcm, together with an activation energy of ~ 0.54 eV, can be achieved without any boron doping, this time (provided that the growth rate is high enough). It is, thus, the interplay of at least three components, namely the feed gas purification, the outgasing rate and the growth rate which determines the oxygen contamination of a grown µc-Si:H layer.

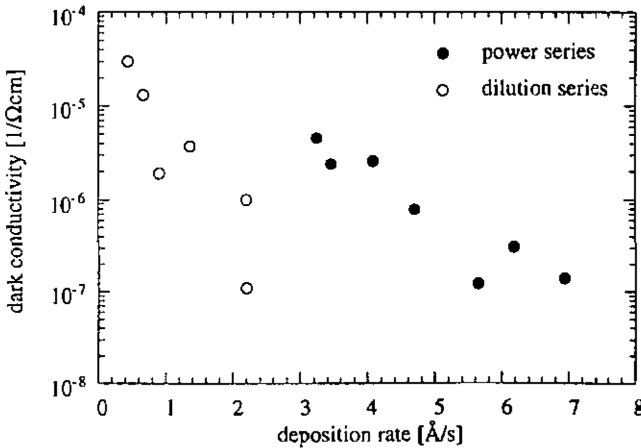

Fig. 5.2. Variation of the room temperature dark conductivity for two series (one with changing dilutions of silane into hydrogen, the other with different input powers) of purified µc-Si:H films as a function of the deposition rate: An increase in the deposition rate can help to further reduce the oxygen incorporation into the µc-Si:H layer.

The extent to which the deposition rate can influence the dark conductivity of µc-Si:H is illustrated in fig. 5.2, where we have plotted the measured dark conductivities of two series of µc-Si:H layers, both deposited with the help of a gas purifier, as a function of the deposition

rate. Even though the two series were deposited under quite different conditions (one by changing the dilution of silane into hydrogen [Beck 96-3], the other by changing the input power), they both show the value of σ_d to decrease significantly as the deposition rate is increased.

5.2.1. The grain boundary trapping model

The model most widely used to explain the variation in dark conductivity (and in Hall mobility) with doping for poly- and microcrystalline silicon with doping is the model introduced by Seto [Seto 75]. It claims that the transport properties of polycrystalline silicon films are governed by carrier trapping at the boundaries, leading to the creation of potential energy barriers at the grain boundaries which impede the motion of carriers from one grain to the other. For his calculations, Seto assumed identical grains of size γ, grain boundaries of negligible thickness with a number of traps (Q_T) and a uniform distribution of ionised impurity atoms N in the crystallites.

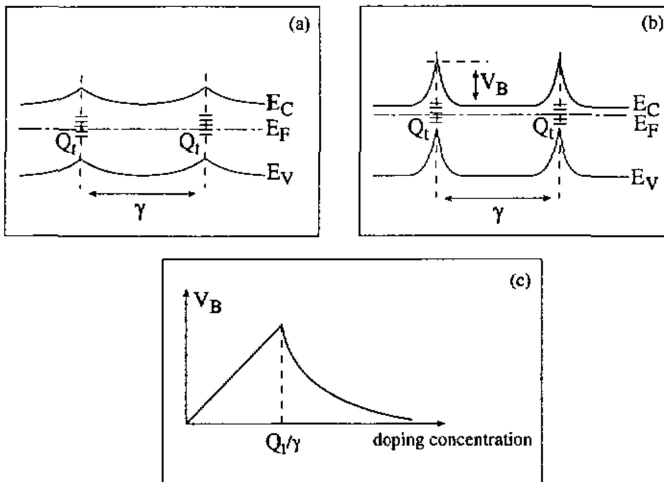

Fig.5.3. Schematical representation of the low-doping regime (a) and the high-doping regime (b) according to [Seto 75]. For low doping levels, the entire grain is depleted of carriers and the potential barrier between the grains increases linearly with doping. For doping levels higher than Q_T/γ the grains are only partially depleted and V_B decreases inversely proportional to the doping level. This variation of the grain boundary height with doping is shown in fig. (c).

The grain boundary traps Q_T are assumed to be initially neutral. They become, however, charged as free carriers from the crystallites are trapped, forming thereby depletion regions on both sides of the grain boundaries (see fig. 5.3). Depending on the available density of free carriers and the number of the grain boundary traps, the formed depletion regions become more or less pronounced. One can discern two main regimes (see fig. 5.3 (a) and (b)):

$\gamma N < Q_T$ (low doping - (a)): in undoped or slightly doped poly- or microcrystalline material the number of impurity atoms (and therefore also the free carrier density) in the crystallites is low. The number of available free carriers is, thus, not sufficient to completely fill the grain boundary defects Q_T. As a consequence, the depletion region built up around the grain boundaries will extend throughout the whole grain, depleting the latter almost completely from free carriers. The height of the potential barriers built up at the grain boundaries can be calculated using Poisson's equation, putting the depletion width W equal to $\gamma/2$:

$$V_B = e\gamma^2 N/8\varepsilon \tag{5.4}$$

where ε is the dielectric constant and e the elementary charge. The potential barrier V_B at the grain boundaries will, thus, grow linearly with the impurity (or doping) concentration. These potential barriers will more and more impede the transit of free carriers from one grain to an adjacent grain which results in a decrease of the effective free carrier mobility (μ_{eff}), given in this model by thermal emissions of free carriers over these potential barriers:

$$\mu_{eff} = \mu_o \exp\left(-\frac{eV_B}{kT}\right) \tag{5.5}$$

where e is the elementary charge, kT the thermal energy and μ_o a mobility prefactor which varies linearly with the grain size and which represents the mobility in the crystalline lattice.

The variation of the free carrier density $n_f(N)$, $\mu_{eff}(N)$ and the dark conductivity $\sigma_d(N)$ as a function of the doping (impurity) concentration N in this Seto-model is schematically shown in fig. 5.4. Note, that the experimental results presented by Seto [Seto 75] (assuming the measured Hall mobility to be equal to μ_{eff}) indeed reflect such behaviour.

$\gamma N > Q_T$ (high doping - (b)): doping further the poly- or microcrystalline material, a critical concentration N_{crit} is achieved and the number of available free carriers γN is equal to the grain boundary trap density Q_T:

$$N_{crit} = Q_T / \gamma \tag{5.6}$$

As all grain boundary traps will be completely filled now, a further increase of the doping concentration will sharply increase the free carrier density and the depletion region will become confined close to the grain boundary regions ($W \ll \gamma$) as illustrated in fig. 5.3 (b). The apparent

Fermi level in the crystalline phase will now be given by the doping concentration directly and the potential barriers between two grains will rapidly decrease according to:

$$V_B = eQ_T^2/8\varepsilon N \tag{5.7}$$

As a direct consequence, according to equation 5.5, the effective mobility μ_{eff} will overcome its minimum value and steeply increase again. The qualitative changes of $n_f(N)$, $\mu_{eff}(N)$ and the $\sigma_d(N)$ with doping are, again, plotted in fig. 5.4.

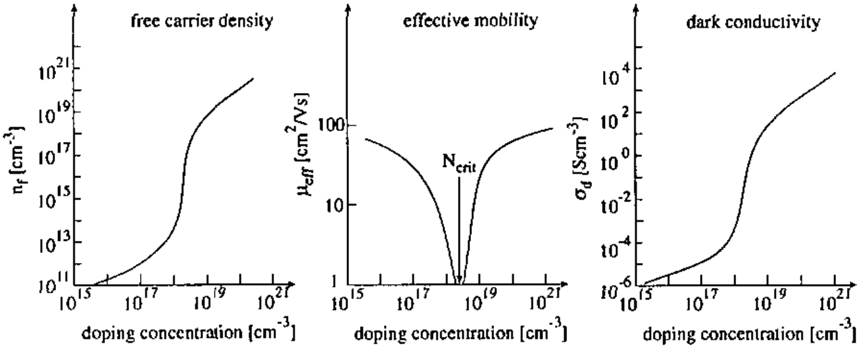

Fig. 5.4. Schematical representation of the changes of the free carrier density n_f, the effective mobility μ_{eff} and the dark conductivity σ_d as a function of the doping concentration in the grain boundary trapping model. For a critical doping concentration $N_{crit} = Q_T/\gamma$ the number of free carriers per grain equals the number of grain boundary traps and the effective mobility reaches its minimum value.

5.2.2. Critical reflections about the grain boundary trapping model

The application of the grain boundary trapping model to polycrystalline silicon [Seto 75], but also to glow-discharge μc-Si:H [LeComber 83] gave convincing results. We would, however, like to expose here some critical reflections on this model when applied to intrinsic μc-Si:H with small grains (some hundreds of Å).

The grain sizes of the material studied by Seto are, in fact, very similar to that of our VHF-GD μc-Si:H material, namely about 200 Å. The important difference resides, as already shown in ch. 4.2.2, in the **passivation** of the grain boundary defects. In Seto's poly-Si material, deposited at relatively high temperatures (650°C), the grain boundaries are unpassivated and present a high trap density of about 3×10^{12} cm^{-2}. Contrary to this, the low-temperature VHF-GD process (≤ 250°C) used for the deposition of our μc-Si:H material allows a very efficient passivation of the grain boundaries by

hydrogen and the defect density in the material can be reduced to about 5×10^{15} cm^{-3} [Beck 96-2]. To give a more palpable feeling about this value, let us make the following estimation, inspirited by Overhof et al. [Overhof 96]: for the sake of simplicity we will assume μc-Si:H material to be composed of identical cylindrical grains with a diameter of 200 Å, a length of 1 μm and a defect density of 5×10^{15} cm^{-3}. Assuming, furthermore, an atomic density of 5×10^{22} cm^{-3} (as for c-Si), we can estimate, that about 1.6×10^{7} atoms constitute a single grain and therefrom about 8.6×10^{5} atoms decorate the grain surface. From these values we can deduce that approximately one single atom per grain is forming a defect. Similar considerations can be made w.r.t. the contamination with impurities which is typically in the order of 2×10^{18} cm^{-3} for the case of oxygen. We deduce that about 600 impurity atoms "contaminate" each grain. In our opinion it is questionable for such small concentrations, to talk of "densities" as is the case for the grain boundary trapping model.

From this point of view doubt may also be risen about the mobility in the grain boundary trapping model where the mobility said to be mainly governed by the thermal activation over potential barriers at the grain boundaries. In the image we have, free carriers are in permanent interaction with grain boundaries due to their thermal movement. In a c-Si lattice, free carriers typically cover about 10^{-5} cm between two scattering events. This means that the mean free path is much longer than the grain size of our μc-Si:H material as illustrated in fig. 5.5. It is therefore conceivable that free electrons and holes travel through the crystalline phase without any impediment, but that they experience strong and frequent scattering, trapping and recombination processes when randomly brought in contact with the surrounding grain boundaries. In this model the mobility of the free carriers will be determined by the smallest dimension of the crystallites (i.e. by the 200 Å diameter for the case of our elongated cylindrical crystallites) which will limit the mean free path of the carriers.

Note, that the above reflections were developed particularly for our low-defect VHF-GD μc-Si:H. The situation is quite different for the original polycrystalline material as studied by Seto [Seto 75] as the unpassivated grain boundaries in his material present about 10^{4} times more defects. The grain surfaces in such materials will, thus, be decorated by much more defects than in our μc-Si:H material and the "Seto-model" may be correct here. On the other side, Seto studies the influence of boron doping on the transport parameters, starting from doping concentrations as low as 10^{16} cm^{-3}. Such concentrations are, however, far too small to supply each grain with at least one impurity atom. We thus have doubts about the correctness of the grain boundary trapping model applied to poly- and microcrystalline materials for such low impurity concentrations.

At the present state of the knowledge our critical reflections on the validity of the long-established "Seto model" are, however, purely speculative. Systematic experiments will be necessary in future to confirm or to reject one or the other model in the case of low-defect μc-Si:H material (such as studied in this thesis). These measurements are, however, outside of

the scope of the present work. A first step towards such systematic investigations consists in the "preparation of the necessary tools" and this was done in the present work. We will, therefore, retain from discussing our experimental results in the context of a given model; but we will rather restrict ourselves to the presentation of experimental data.

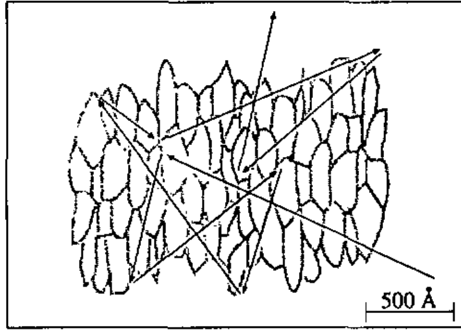

Fig. 5.5. Schematical illustration of the random thermal movement of free carriers in a crystalline silicon lattice (black arrows) in comparison to the dimension of the crystallites in μc-Si:H (drawn in grey).

5.3. Time of Flight measurements on μc-Si:H

We have, to our knowledge, for the first time applied the Time of Flight (TOF) measurement technique to μc-Si:H. Our work was thereby motivated by three advantages of this technique. First, it is possible to measure the electrical transport (in the dark) parallel to the growth direction, and, secondly, the transport can be studied for electrons and holes independently. Last but not least, the TOF measurements can in principle be performed on standard solar cells where only the top contact needs to be modified. This third point is of special importance, as there are justified presumptions that for identical deposition conditions the properties of μc-Si:H material strongly depends on the underlying substrate [Torres 95], [Kondo 96].

Note that a general introduction to the TOF measurement technique has already been given in ch. 1.4 and will thus not be repeated here. However, we will discuss briefly in the following chapter some of the experimental conditions which are difficult to be fulfilled for μc-Si:H.

5.3.1. Particularities of the TOF method applied to μc-Si:H

Before applying the TOF technique to our μc-Si:H material we checked some of the experimental conditions listed in ch. 1.4.1 such as the dielectric relaxation and the RC constant

of the system. The μc-Si:H thereby exhibited some particularities which will be discussed hereafter.

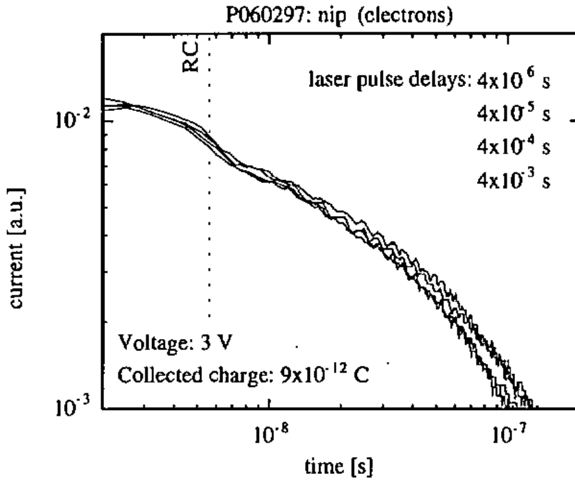

Fig. 5.6. Current transients of electrons for a 5.5 μm thick n-i-p cell (dark conductivity of a film produced under identical conditions: 5×10^{-8} 1/Ωcm). Even though the delay of the laser pulse after the application of the voltage to the sample was changed by 3 orders of magnitude, the changes in the transients keep within the experimental errors.

The dielectric relaxation time

In midgap μc-Si:H the dark conductivity is around 10^{-7} 1/Ωcm. According to equation 1.21 the corresponding dielectric relaxation time τ_{diel} is around 10^{-5} s and we expect the electric field in the sample to be screened out within this same time. In order to guarantee an unchanged electric field in the μc-Si:H sample during the whole experiment, the TOF measurement must thus be carried out within this time period τ_{diel}. As such short relaxation time may be critical, we wanted to check the fulfilment of this condition (1.21) experimentally. We increased the delay of the laser pulse after the application of the voltage to the sample from 4×10^{-6} s up to 4×10^{-3} s and recorded the current transients. The result is represented in fig. 5.6: the current transients are unchanged for all laser pulse delays and we do not observe any collapse of the current signal due to a screening of the electric field. This surprising fact is in clear contrast to the situation in a-Si:H and we will explain it later on in this chapter.

The RC "constant"

An approximate knowledge of the sample capacitance C_S is required for a correct measurement by the TOF technique. As shown in fig. 5.7, C_S forms, together with the shunt (and contact) resistor R, the RC_S constant of the system and determines (in the current mode of TOF) the time resolution of the experiment: for times shorter than RC_S, the electrical circuit is not able to replenish the charge on the electrodes of the sample capacitance. Consequently the current transients are distorted and become only relevant at times longer than RC_S.

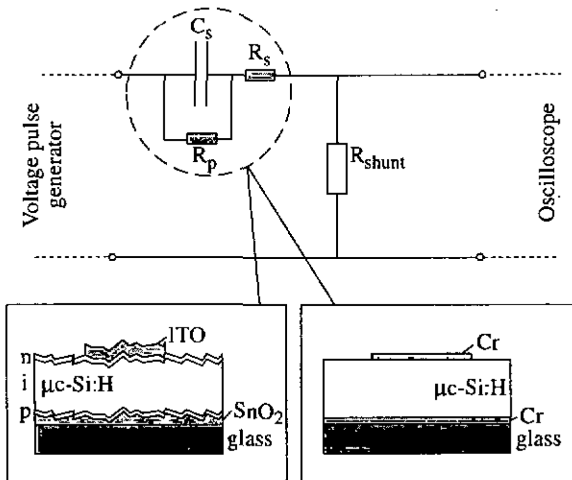

Fig. 5.7. Equivalent electrical circuit of the sample structures used for TOF measurements. The layer configuration (with two blocking Cr contacts) as well as the p-i-n solar cell structure (in reverse polarisation) can be represented as a capacitor with a parallel and series resistor R_p and R_s which form together with the shunt resistor R_{shunt} the RC constant of the system.

To estimate the sample capacitance we used two different techniques. On one side we determined the RC decay of the polarisation current after the application of the voltage pulse to the sample (for a known shunt resistor of typ. R = 10 kΩ). On the other side we measured C_S by a commercial impedance analyser (HP 4192A LF) with a bridge configuration that allows for a capacitance and conductance measurement in the frequency range between 10 Hz and 10 MHz. Using these techniques of capacitance measurement, we came accross two unexpected particularities of our μc-Si:H. In the case of a-Si:H the measured sample capacitance C_S is close to the calculated geometrical capacitance C_g:

$$C_s \approx C_g = \frac{A\varepsilon}{d}, \tag{5.8}$$

where A is the sample contact area, d the sample thickness and ε the dielectric relaxation constant ($\varepsilon \approx 12 \cdot \varepsilon_0 \approx 10^{-12}$ As/Vcm for c-Si). This, however, does not hold for our μc-Si:H layers where the sample capacitance is significantly higher than C_g. Furthermore, C_s is not a constant, but changes with the applied voltage, and, consequently, also the value of the RC-product (i.e. of the "time constant") becomes voltage dependent. This second fact is particularly "annoying" when performing TOF measurements as the RC signal may now easily be confused with a real carrier transit signal; therefore, special attention must be paid to this fact when measuring.

Field distribution in μc-Si:H samples

The above observations, namely the enhanced and voltage dependent capacitance as well as the absence of a screening effect, allows for two possible explanations.

The first one suggests a very quick screening within the sample and a concentration of the electric field to the interfaces at the bottom and the top of the sample as illustrated in fig. 5.8.a). For this case, the screening would be too quick to be observed by our experiment and the sample capacitance would be given by the two large junction capacitances formed by the space charges near the interfaces. As the width of these space charge regions is voltage dependent, a change of C_s with applied voltage can be expected.

The second possible explanation takes into account the heterogeneity of the μc-Si:H material which is composed of crystalline grains and grain boundary regions. We can conceive that an applied voltage is extremely quickly screened within the crystallites and becomes confined to the grain boundaries as shown in fig. 5.8.b). As a result the applied voltage drops in steps at the grain boundaries and regions of almost no field (grains) alternate with regions of high field. This confinement of the electric field to a small part of the sample thickness leads to many grain boundary capacitances C_{gb} connected in series. This results in an enhanced sample capacitance:

$$C_S = \frac{A\varepsilon}{d_{eff}} \tag{5.9}$$

where d_{eff} represents the fraction of the sample thickness with non-zero electric field.

To discriminate between these two possibilities we performed the following experiment: we measured C_s on two μc-Si:H p-i-n solar cells, produced in one and the same deposition run, but where one half of the substrate was temporarily shielded by a shutter during the growth of the i-layer. As a result, two high quality p-i-n cells of 1.1 μm and 2.8 μm thicknesses were obtained. If our first explanation was correct and therefore the electric field was concentrated to the interfaces, the sample capacitance should be the same for both cell thicknesses. In the

second situation, if the applied voltage drops in steps across the whole i-layer, C_S is expected to scale with the i-layer thickness.

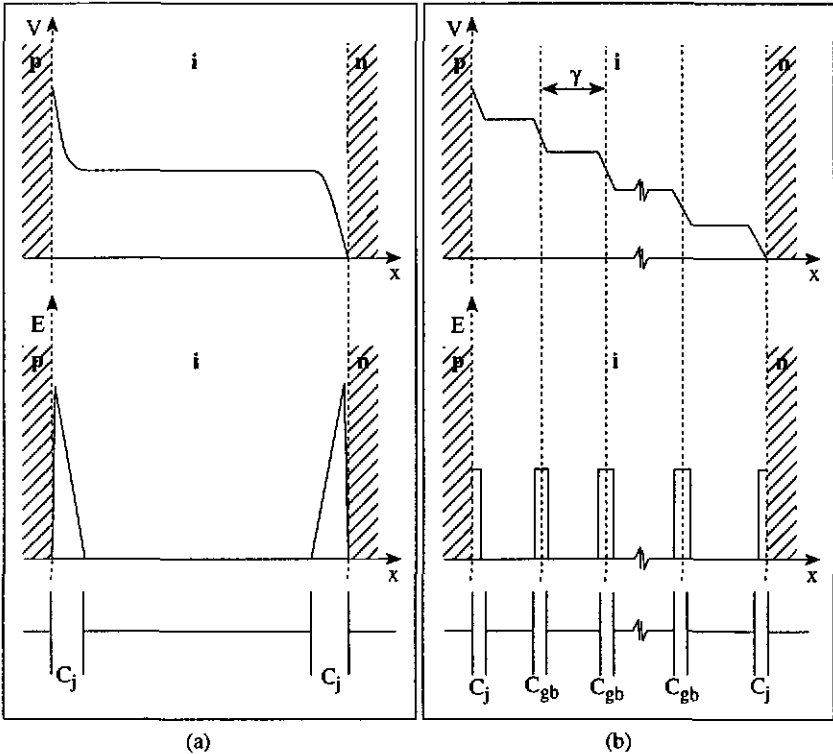

Fig. 5.8.Schematical representation of the two possible models proposed to explain the absence of screening and the enhanced capacitance in μc-Si:H samples: in both models the electric field E is concentrated in a small part of the i-layer thickness. In case (a) E is concentrated to the interfaces and in the case (b) the voltage drops in small steps over the grain boundaries.

The experimental results clearly support the second explanation. For applied voltages where the influence of the internal field becomes small, the sample capacitance of the thin cell is about twice C_S of the thick one (see fig. 5.9.a)). Compared to the calculated geometrical capacitances C_g, the measured C_S are about 5 times higher. This means that the electric field in these p-i-n cells is confined to about one fifth of the i-layer thickness (at the grain boundaries) whereas four fifths of the i-layer is field-free (crystallites). This fact has also consequences on the transport. As illustrated in fig. 5.10 free carriers will easily cross the field-free crystallites

by diffusion, whereas drift-assisted movement is restricted to the grain boundary regions. This means that the effective thickness of the i-layer to be covered by drift is only about one fifth (e.g. ~0.6 µm in the 2.8 µm thick cell) and this may be the reason that even in 4 µm thick p-i-n cells almost complete carrier collection is observed [Meier 96].

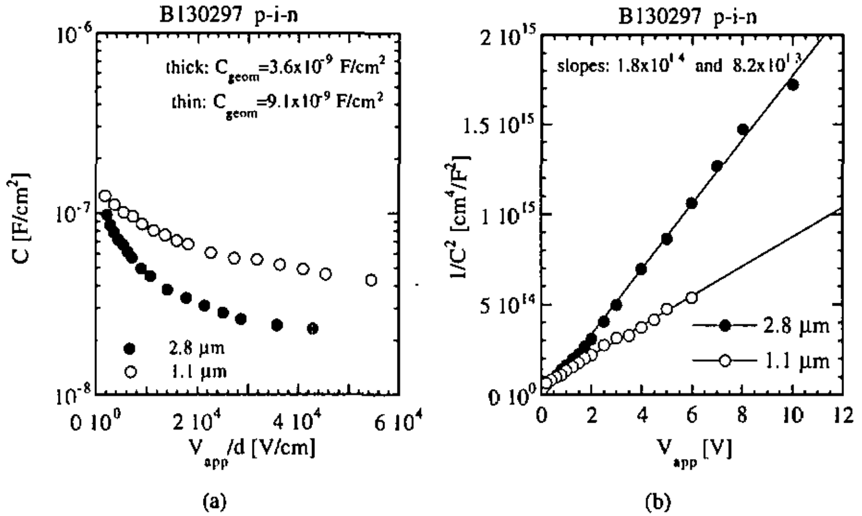

Fig. 5.9. Sample capacitances C_S measured on two µc-Si:H p-i-n solar cells with identical i-layer properties but with thicknesses 2.8 µm and 1.1 µm. C_S as well as the slope of the $1/C^2$ plot scale with the i-layer thickness, indicating, thus, that the sample capacitance is determined by the bulk material rather than by the interfaces.

Finally, also the change of the sample capacitance with the applied voltage can be reconciled with this model. In mono-crystalline silicon a voltage dependence of the capacitance is observed for metal-semiconductor contacts, and this dependence is used for the determination of the doping density N_D and the height of the formed barrier [e.g. Sze 85]. Thereby, the plot of $1/C^2$ as a function of the applied voltage gives a straight line whose slope is proportional to N_D and the intersection with the x-axis corresponds to the contact barrier height:

$$\frac{1}{C^2} = \frac{2 \cdot \left(V_{bi} - V_{app}\right)}{e\varepsilon N_D} \tag{5.10}$$

where V_{bi} is the built-in potential, V_{app} the applied voltage, e the elementary charge, ε the dielectric constant and N_D the doping density.

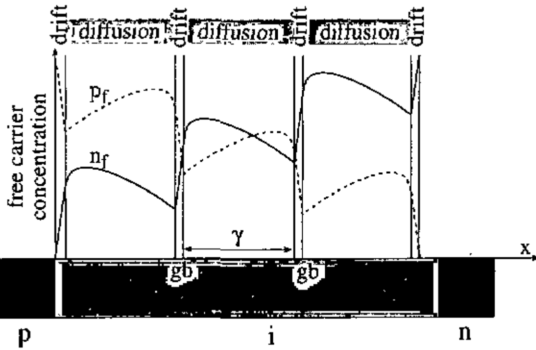

Fig. 5.10. Qualitative picture of the distribution of free carriers in the i-layer of a μc-Si:H p-i-n solar cell under homogeneous illumination (red light). According to the transport model introduced above, ***drift*** *is the driving force at the grain boundaries whereas free electrons and holes cross by* ***diffusion*** *the field-free crystalline grains.*

For both cells, i.e. the thin and the thick p-i-n cell, we obtain, similar to c-Si, a linear dependency between $1/C^2$ and the applied voltage (fig. 5.9.b)). However, contrary to the situation in crystalline semiconductors where one single metal-semiconductor junction is studied, we have to take into consideration here a whole sequence of grain boundary capacitances C_{gb}. As the slope of the $1/C^2$ plot can be shown to be proportional to the number of C_{gb} involved, an increase of the sample thickness, accompanied by an increase of the number of grain boundaries, will therefore proportionally increase the slope. This is exactly what we observe in the p-i-n cells studied here.

5.3.2. Drift mobilities in μc-Si:H

So far mobilities in CVD μc-Si:H materials were only determined by Hall measurements and the published data show large scattering of the values found for μ_H. Considering the variety of the μc-Si:H materials studied and the fact that most of the data was measured on doped μc-Si:H, such large variations are not surprising. High values of Hall mobilities were observed by Seto [Seto 1975] and by Podbielski and Möller [Podbielski 84] on series of undoped and p-doped polycrystalline silicon films prepared at temperatures around 650°C and with grain sizes of 200 Å. They both found mobility values as high as 50 cm²/Vs for highly doped materials together with a sharp mobility minimum at a doping concentration of about 2×10^{18} cm^{-3}. μc-Si:H materials prepared at lower temperatures generally exhibit lower mobilities. In the work by Le Comber et al. [LeComber 83], who performed Hall experiments on undoped and p-type glow discharge μc-Si:H (γ = 60 - 80 Å), the Hall mobilities did not exceed 5 cm²/Vs, even for doping levels as high as 10^{20} cm^{-3}. Similar results were also

obtained on n- and p-type μc-Si:H produced by the VHF-GD technique by Dubois et al. [Dubois 92]; they measured values between 0.6 and 5.3 cm^2/Vs. In more recent works, Deyan He et al. [Deyan He 94] found in p-type μc-Si:H deposited by a "layer-by-layer technique" (at 300 - 360°C) RT Hall mobilities between 5 and 18 cm^2/Vs, Middya et al. [Middya 96] measured values between 0.4 and 15 cm^2/Vs in p-type Hot-Wire μc-Si:H materials, and Hapke et al. [Hapke 96] obtained in their n-type PE-CVD μc-Si:H material ($\gamma = 50$ - 350 Å) Hall mobility values between 0.1 and 1.7 cm^2/Vs.

At present no Hall mobility data are available on our midgap VHF-GD μc-Si:H material as its very low dark conductivity turns Hall measurements into a difficult task. We thus applied the TOF technique to our μc-Si:H in order to measure the **drift mobilities** μ^D of electrons and holes separately. This approach was further encouraged by the rather low Hall mobilities (< 20 cm^2/Vs) observed by the above authors in low-temperature and small grain μc-Si:H as the TOF technique is especially appropriate for low mobility materials. Note, however, that it will not be possible to compare drift mobility with Hall mobility data: the drift mobility μ^D determined by TOF represents the ease of transport parallel to the growth direction. Its value, compared to the band mobility μ^o, is thereby lowered by the ratio of free carriers over trapped carriers [Spear 69]:

$$\mu_D = \mu^o \frac{n_f}{n_f + n_t} \tag{5.11}$$

On the other side, for the evaluation of the Hall mobility the free carrier density (obtained from the Hall experiment) and the dark conductivity (measured in coplanar configuration) are involved. The Hall mobility μ_H is related to the band mobility μ^o by a proportionality factor (for extrinsic material), which is, however, usually neglected.

Experimental

We performed TOF measurements on μc-Si:H samples prepared by the VHF-GD and used two different structures: μc-Si:H layers with two semitransparent chromium Schottky - contacts on both sides and p-i-n (or n-i-p) solar cells with ITO top contacts. Thereby, the main experimental problem resided in the enhanced sample capacitance of μc-Si:H (see ch. 5.3.1) which increased considerably the RC constant. This again greatly reduced the time resolution of the measurement and added an uncertainty in the time origin. To prevent this problem we took three measures which all reduce the RC constant: we reduced the sample contact area to an absolute minimum, we measured preferably thick samples (ideally $d > 3$ μm) and we paid special attention to low contact resistance. For the evaluation of μ_D we further checked the following points:

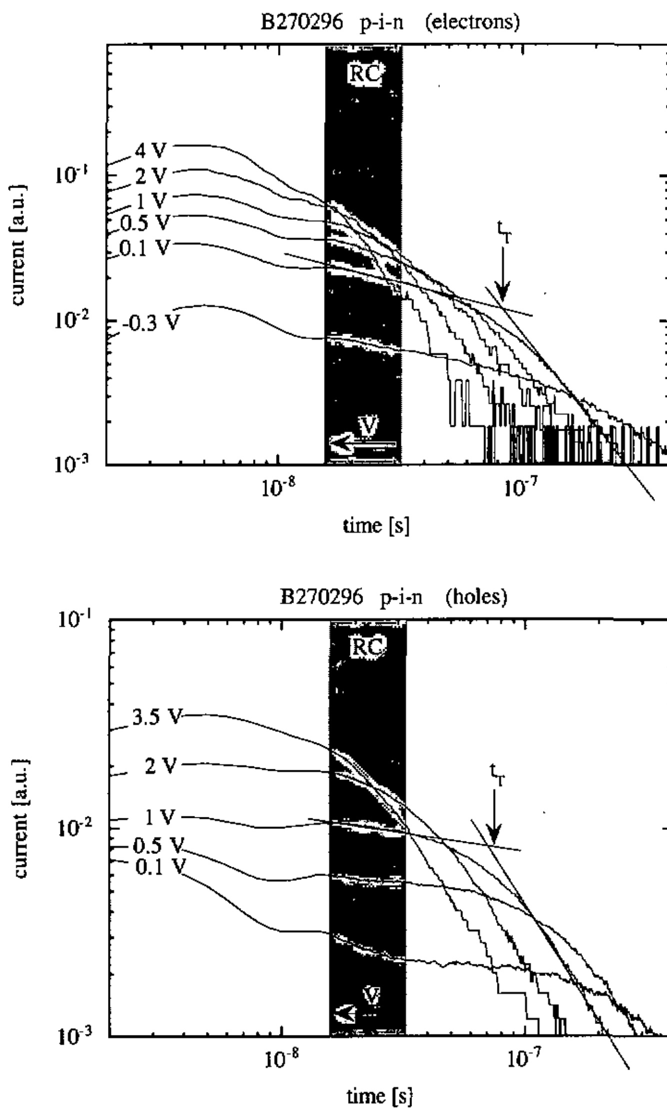

Fig. 5.11. Current transients obtained on a 3.7 μm thick μc-Si:H p-i-n cell. After an initial decrease of the signal due to the RC constant, we observe the characteristic current shape (scaling with voltage) of carrier transport and carrier extraction.

1. RC time constant must be clearly shorter than the transit time (note that RC in μc-Si:H can change with applied voltage).
2. The photogenerated charge must be (much) smaller than the charge on the electrodes (Small Signal TOF, see. ch. 1.4).
3. Clear crossing of the current transients must be observed with changing voltage (the transit time must scale with voltage).
4. Determination of μ_D at voltages where the charge collection is almost complete.

Results

A systematic examination of the drift mobilities of electrons and holes on a series of specific μc-Si:H materials (in order to correlate with e.g. the grain size, the doping level or the crystallinity) was unfortunately out of the scope of this work. As first results we will present here the drift mobility measurements on a μc-Si:H p-i-n cell of good quality and a series of four layers produced with different dilutions of silane into hydrogen (see also ch. 4.2.1).

The two current transient curves (for electrons and holes) obtained on a 3.7 μm thick μc-Si:H p-i-n cell (110 MHz, ~ 5% dilution, $T_{dep} \approx 200°C$, produced with the help of the purifying technique - see also [Meier 96]) with a conversion efficiency of 5.8 % are shown in fig. 5.11. For these measurements the cell was illuminated from p-side (for electron measurements) or from n-side (for hole measurements) with reverse voltages applied. The sample capacitance attenuated at about 52 pF for high voltages, the contact resistor ~330 Ω which resulted in $RC \approx 1.7 \times 10^{-8}$ s.

One can discern in this picture an initial current decay due to RC constant followed by a rather non-dispersive (constant) transit current and the subsequent "kink" at t_T due to carrier extraction. The carrier collection was more than 80% for all voltages. To extract the drift mobilities we used the simple definition:

$$\mu_D = \frac{d^2}{\left(V_{int} + V_{app}\right) \cdot t_T} \tag{5.12}$$

where V_{app} are the applied voltage and V_{int} the (unknown) internal voltage (built up by the doped layers), d the sample thickness and t_T the measured transit time. The latter has been determined by two slopes as indicated in fig. 5.12. To evaluate μ_e^D and μ_h^D we assumed in a first approximation μ_e^D and μ_h^D to be voltage-independent and plotted d^2/t_T as a function of V_{app} (fig. 5.12). Therefrom we extracted the slope which is about $\mu_e^D = 2.6$ cm²/Vs for electrons and $\mu_h^D = 1.6$ cm²/Vs for holes. For reverse voltages above 2 V, we observe, however, a deviation from the linear behaviour which can be attributed to the RC constant which already starts to influence here.

The drift mobilities obtained on this p-i-n sample correspond to typical values obtained on our purified μc-Si:H material. Furthermore, they show another characteristic feature of

μc-Si:H, namely that $\mu_e^D/\mu_h^D \approx 2$. This ratio is in clear contrast to a-Si:H, where the strongly asymmetric band tails lead to a ratio of $\mu_e^D/\mu_h^D \approx 100$. As the drift mobility is deduced from a multiple trapping transport mechanism and, thus, represents the mobility of the free and trapped carriers (see ch. 1.4.1), the large amount of trapped holes in the wide valence band tail strongly reduces the value of μ_h^D in the case of a-Si:H [i.e. Street 82]. Our observation in μc-Si:H admits, thus, two possible explanations. First, the transport in μc-Si:H material is governed by the crystallite phase and the mobility ratio of about 2 (similar to the situation in c-Si) can be associated to the different effective masses of electrons and holes in the silicon lattice. As a second explanation one can imagine a multiple trapping process, similar to that of a-Si:H, but where the shallow traps near the conduction and valence bands show a much smaller asymmetry. As at the present time we do not dispose of information about the existence and extension of bandtails or shallow traps in μc-Si:H material this issue remains open.

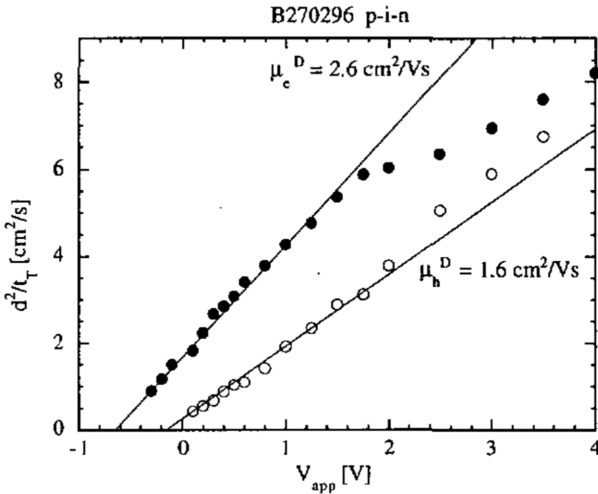

Fig. 5.12. Evaluation of the drift mobilities of the 3.7 μm thick μc-Si:H p-i-n cell from the measurements of fig. 5.11. From the slope of the plot d^2/t_T as a function of the applied voltage V_{app} the electron and hole drift mobilities $\mu_e^D = 2.6$ cm²/Vs and $\mu_h^D = 1.6$ cm²/Vs are deduced. For $V_{app} > 2$ V the RC constant starts to influence the measurement.

It can be conceived that the drift mobility of μc-Si:H material depends also on the grain size and/or the crystallinity. To follow up this question we measured the electron and hole drift mobilities on a series of μc-Si:H layers which were produced at 110 MHz by changing the

dilution of silane into hydrogen from 7.5% to 1.25% (see table III). Optical measurements ([Beck 96-3] and fig. 4.4) as well as structural investigations [Goerlitzer 97] clearly show a transition from a-Si:H (7.5% dil.) to highly microcrystalline material (5% → 1.25% dil.). The drift mobilities of electrons and holes measured on these samples are listed in table III and seem to confirm our expectations: the drift mobility of electrons steadily improves from 0.9 cm^2/Vs (in the a-Si:H layer) to 2.9 cm^2/Vs with increasing crystallinity. The hole drift mobility μ_h^D jumps to 0.4 cm2/Vs as soon as the material turns to be microcrystalline and from there on increases similarly to μ_e^D. Note, that the ratio of μ_e^D/μ_h^D is here again around 2 for all three μc-Si:H samples. However, in this series not only the crystallinity increases with dilution, but the μc-Si:H material becomes also more and more extrinsic as the deposition rate becomes very small for high dilutions (see fig. 5.2). As, so far, we cannot exclude that the Fermi level position or the contamination with impurities (i.e. with oxygen) also influence the drift mobility, it is premature to draw a final conclusions from our measurements.

$[SiH_4] / [SiH_4+H_2]$	μ_e^D [cm^2/Vs]	μ_h^D [cm^2/Vs]
7.5% (a-Si:H)	0.91	0.011
5% (μc-Si:H)	1.24	0.41
2.5% (μc-Si:H)	1.47	1.02
1.25% (μc-Si:H)	2.85	1.08

Table III. Drift mobilities of electrons and holes measured on a series of layers produced using different dilutions of silane into hydrogen. The sample produced at 7.5% dilution is amorphous, all the others show clearly microcrystalline features. The magnitude of μ_e^D and μ_h^D rises as the dilution (and thereby the crystallinity) is increased. The ratio of μ_e^D/μ_h^D is about 2 for all the μc-Si:H samples.

5.3.3. μτ products in μc-Si:H from charge collection measurements

In a-Si:H p-i-n solar cells the i-layer must be quite thin (typ. 0.5 μm) in order to achieve good collection of the photogenerated carriers. The limiting carriers are thereby holes due to their much lower mobility compared to electrons. In contrast to this, μc-Si:H p-i-n solar cells with thicknesses up to 4 μm were produced which still show almost complete carrier collection [Meier 96]. On one side the enhanced hole drift mobility in μc-Si:H may account for this, but on the other side, also the carrier lifetime τ is involved and, so far, we have no information about the value of this lifetime in μc-Si:H. This motivated us to perform TOF charge collection measurements in our μc-Si:H material in order to evaluate the mobility × carrier lifetime products (μτ) for electrons and holes according to Hecht formula (1.20).

Our $\mu\tau$ results on μc-Si:H are, again, rather preliminary and more measurements on a diversity of μc-Si:H samples will be necessary to deduce a general trend. Here, we will present TOF carrier collection measurements performed on two μc-Si:H samples, one layer deposited on chromium coated glass and one n-i-p solar cell (see table IV). Thereby, the film and the i-layer of the solar cell were produced using identical deposition parameters (110 MHz, 5% dilution, $T_{dep} \approx 220°C$, with gas purifier); the obtained layer (P300197B) was clearly midgap ($\sigma_d \approx 5\times10^{-8}$ 1/Ωcm, $E_{act} \approx 547$ mV) and the corresponding n-i-p cell (P060297G) had a conversion efficiency of $\eta = 5.1$ %.

sample	structure	thickness
P300197B	glass / SnO_2 / layer (μc-Si:H) / Cr (semitr.)	2.7 μm
P060297G	glass / SnO_2 / n-i-p (μc-Si:H) / ITO	5.5 μm

Table IV. Structure of the μc-Si:H layer and the corresponding n-i-p cell used for the carrier collection measurements (fig. 5.13). The intrinsic μc-Si:H material of both samples were deposited using the same deposition parameters.

The electron and hole collection curves of these two samples are represented in fig. 5.13. For the measurements we tried to photogenerate the approximately same number of electrons and holes in both, the layer and the cell. For the electron measurements the samples were illuminated through the front contact, for hole measurements through the bottom contact; the polarisation of the applied voltage was kept unchanged. Thereby, in the layer as well as in the cell configuration, the first interface in the growth sequence (SnO_2-μc-Si:H and n-i) turned out to be a defect rich region and we thus were obliged to use here a light which penetrates deeper into the structure (610 nm instead of the usual 550 nm) in order to prevent an important hole loss close to the interface [Wyrsch 92]. Another difference resided in the blocking properties of the chromium Schottky contacts used for the layers and the n-i-p structure in reverse polarisation: The leakage current through the chromium contact was slightly higher, leading, thus, to a less clear saturation in the carrier collection and therefore to an underestimation of the $\mu\tau$ products in the layer structure. However, this effect is not dramatic in this sample and the induced uncertainty is within the experimental error.

To evaluate the $\mu\tau$ product in the cell we used the simple Hecht formula (1.20) and we added to the applied external voltage an internal voltage which we set to 0.4 V. Changing this internal voltage values between 0.2 V and 0.6 V introduced variations of the fitted $\mu\tau$ products smaller than a factor of 2. Note, that this simple evaluation procedure is sufficient here as even for no applied voltage the collection of photogenerated carriers is high, indicating, thus, the internal field to extend through the whole layer thickness.

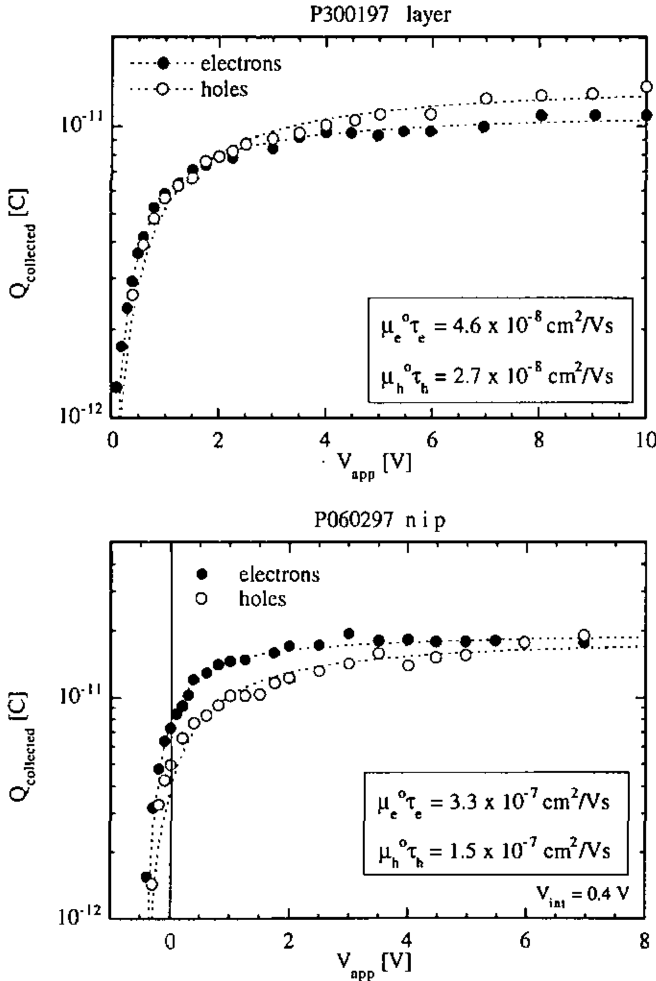

Fig. 5. 13. Carrier collection measurements on a μc-Si:H layer (on SnO_2 coated glass) and on the corresponding μc-Si:H n-i-p cell, fitted by the standard Hecht formula (1.20).

The results obtained on this μc-Si:H layer and the corresponding cell show an interesting fact: the collection is better and the μτ product evaluated in the n-i-p device is clearly higher than in the corresponding layer deposited on SnO_2 coated glass. The deduced μτ products, not significantly higher than in a-Si:H, thereby reflect typical values as obtained also on other μc-Si:H layers and cells. We also obtain, here again, a ratio between the hole μτ product and

electron $\mu\tau$ product which is close to 2 whereas it is usually around 10 in undoped and about 1.2 in midgap a-Si:H [Beck 96-1].

The observation of better transport properties in solar cell devices supports the presumptions that μc-Si:H material grown on SnO_2 (or chromium) has different characteristics than μc-Si:H grown on an underlying doped μc-Si:H layer. For future investigations of the properties of μc-Si:H material this also means, that one should give preference to characterisation methods which can be applied directly to μc-Si:H p-i-n (or n-i-p) devices rather than measuring on μc-Si:H layers deposited on glass.

5.3.4. Density of states in μc-Si:H from post-transient TOF

The post-transient TOF, which is an extension of the TOF flight experiment to a much longer time scale (up to 1 s) [Seynhave 89], gives information about the density of states (DOS) in the gap. In a-Si:H this method can be used for example to monitor the light-induced creation of defects [Zapletal 94]. Thereby, the electrons and holes which are deep-trapped during transit are thermally remitted after an exponentially longer time τ_{em}:

$$\tau_{em} = \omega_o^{-1} exp\left(\frac{E_T}{kT}\right) \quad (5.13),$$

where E_T is the trap level deepness, kT the thermal energy and ω_o the "attempt to escape frequency" which is around 10^{11} s^{-1} [Tiedje 84]. The collection of these carriers after remission becomes, thus, a direct fingerprint of the DOS.

The application of the post-transient TOF technique to our μc-Si:H material demonstrated some interesting features. In fig. 5.14. a) - d) we plotted the post-transient currents measured on the series of μc-Si:H layers which were produced using different dilutions (7.5% - 1.25%) of silane into hydrogen (see ch. 5.3.2 and [Beck 96-3]). Note that for this experiment we used a high illumination level (SCLC mode) in order to achieve an almost complete filling of the traps.

The post-transient currents from holes are featureless and no particular deep trap states can be inferred. On the other side, for electron transients, very pronounced detrapping at times around 10^{-4} - 10^{-3} s appears for low dilution samples, indicating, thus, the presence of efficient electron traps in the middle of the gap (0.4 - 0.5 eV deep). No similarly strong detrapping is observed in the highly diluted sample (1.25%). This difference, however, can be attributed to a Fermi level shift which occurred in this series of μc-Si:H samples. In fact, with increasing dilutions the measured dark conductivity activation energies decrease from about 0.49 eV (in the 5% dilution material) to 0.22 eV (1.25% dil.) which indicates a shift of the Fermi level position towards the conduction band with increasing dilution. This Fermi level shift may fill up the defect states with electrons and make them inactive for electrons trapping (and invisible for TOF) even though they remain present in the material.

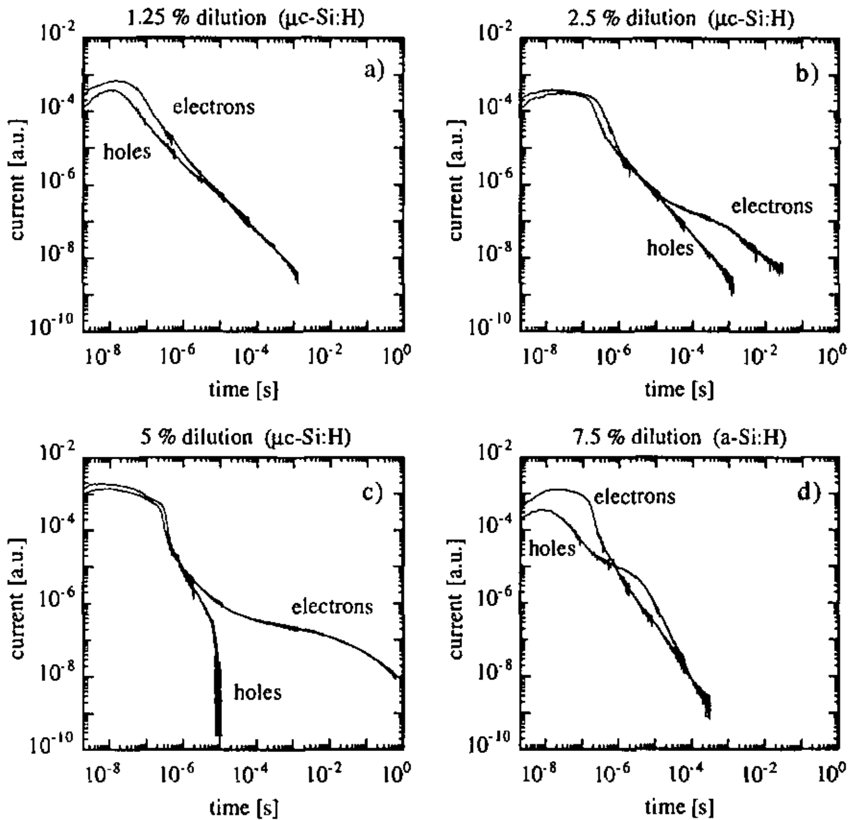

Fig. 5.14. Time of Flight post-transient currents (in SCLC mode) for electrons and holes: the low dilution microcrystalline samples (fig. c), but also b)) show a pronounced detrapping current for electrons, indicating the presence of a detrimental type of electron deep trap in this material.

The physical origin of this trap state is still subject of speculation. Transition metals are known to create sometimes detrimental defects near midgap in c-Si [Green 82]. For instance chromium, the metal we used for the Schottky barrier contacts, can introduce a donor level at E_C - 0.41 eV which was shown to become detrimental in c-Si solar cells for contamination levels higher than about 10^{15} cm^{-3} [Green 82]. As, however, we also observe similar post-transient behaviour in solar cell devices (which do not contain any chromium), we exclude this possibility. On the other side also oxygen, when present in concentrations higher than about 2×10^{18} cm^{-3}, can introduce (in addition to the donor level at E_C - 0.17 eV)

additional deep donor levels [Möller 93]. Even though a gas purifier was used for the deposition of these layers, some of the samples may be highly contaminated due to low deposition rates. We thus have no precise idea about the oxygen contamination of our μc-Si:H material and we cannot exclude, at present, oxygen to be the origin of the observed defect states. Finally, silicon dangling bonds at the surface of the crystallites certainly also introduce defect states in the gap of μc-Si:H material. We have, however, no information about how these dangling bonds are configured at the internal surfaces and which energetic position they take in the gap. More extensive work, also by other measurement techniques, will be necessary here to identify this and other defects in our μc-Si:H material.

5.5. Conclusions

First attempts to use the Time of Flight measurement technique for the characterisation of μc-Si:H showed promising preliminary results. However, the TOF technique cannot be applied straight forward to the new μc-Si:H material; some particularities of μc-Si:H made it necessary to re-examine first the experimental conditions of the technique.

One important finding is thereby that in μc-Si:H samples (cells and layers) the electric field does not extend over the whole sample thickness but is confined to the grain boundary regions. This leads to an enhanced capacitance of μc-Si:H samples which reduces the time resolution of the TOF experiments. As, furthermore, in μc-Si:H the sample capacitance is voltage dependent, special care must be taken to correctly discern the carrier transit signal from the RC signal.

By the TOF technique we measured the drift mobilities μ^D of electrons and holes. The obtained values range from 0.4 to 2.6 cm^2/Vs. The drift mobilities for electrons are comparable to that of a-Si:H whereas the one of holes are considerably enhanced (up to 1.6 cm^2/Vs). Another interesting feature is the ratio between electron and hole drift mobilities which is around 2 for all studied μc-Si:H samples. This ratio is significantly lower than in a-Si:H but close to c-Si where this ratio is given by the difference in the effective masses of electrons and holes in the crystalline lattice.

TOF carrier collection measurements on μc-Si:H layers lead to $\mu\tau$ products which are at best slightly enhanced compared to a-Si:H. However, the $\mu\tau$ products of μc-Si:H solar cells clearly surpass the $\mu\tau$ products measured on μc-Si:H layers produced under the same deposition conditions. This fact indicates that μc-Si:H material grows differently on chromium or TCO coated glass than on an underlying doped μc-Si:H layer in the sequence of a solar cell deposition.

Finally, post-transient TOF measurements on a series of μc-Si:H layers produced by different dilutions of silane into hydrogen reveal a detrimental electron trap in the middle of the gap of μc-Si:H. This trap becomes, however, visible for the TOF technique only in midgap

μc-Si:H. The physical origin of this trap is not clear yet and further investigations are necessary here.

To conclude this section we think that even though the TOF technique is difficult to perform on μc-Si:H material, it can be a powerful tool to obtain precious information about the material. The results presented here are preliminary and deeper investigations on a larger variety of samples are necessary in order to deduce the characteristic features of the electrical transport in μc-Si:H (mobilities, $\mu\tau$ products, defect states) and their dependencies on the material structure. We hope, however, that the presentation of these results can help to stimulate such future work.

FINAL CONCLUSION

If you are short in time or if you just would like to know if there is something new in this thesis, then the following lines might be what you are looking for: a brief collection of the highlights presented in this work.

In the field of a-Si:H, the research activities of many years have resulted in a quite detailed knowledge about the physics of this material. At the same time the conversion efficiencies of thin film p-i-n solar cells made of a-Si:H were considerably improved. However, these two activities more and more diverged, resulting in a lack of apparent correlation between the measured material properties and the corresponding solar cell performances. In this work we elaborated a solution to this problem. The answer comes in the form of a new parameter, the $\mu^o\tau^o$ product, which was defined and introduced in this work together with a simple procedure how $\mu^o\tau^o$ can be evaluated from simultaneously performing photoconductivity and SSPG measurements on a-Si:H layers deposited on glass. Unlike most other techniques currently used for characterising a-Si:H films, the $\mu^o\tau^o$ product provides relevant information about how the material will perform once incorporated in a p-i-n solar cell. The successful correlation between $\mu^o\tau^o$ (determined on a-Si:H layers) and the conversion efficiency η of the corresponding solar cells was demonstrated for two series of samples in the annealed and in the degraded state.

In recent years µc-Si:H p-i-n solar cells have reached remarkable efficiencies and the possibilities to increase them further are far from being exhausted. On the other side, the knowledge about the physical processes governing the optical absorption and the electrical transport in µc-Si:H material is still quite poor. This was the issue which pushed us to investigate in this material. We succeeded to almost entirely explain the enhanced optical absorption in VHF-GD material by taking into account a combination of absorption in crystalline grains and defective grain boundaries together with scattering effects. The latter were shown to essentially account for the enhanced near infrared absorption in VHF-GD material which is a strong asset for solar cell applications. We also introduced a new concept for the collection of the photogenerated free carriers in µc-Si:H solar cells. We presented experimental evidence for a confinement of the electric field to the grain boundaries which suggests a carrier collection in µc-Si:H solar cells driven by drift **and** diffusion. Such collection mechanism is in clear contrast to a-Si:H solar cells (drift alone), but also different from the operation of c-Si solar cells. Finally, we were to our knowledge the first who applied the Time of Flight technique to µc-Si:H material, allowing us to present first values of drift mobilities ($\mu^D(el.) \approx 2 \cdot \mu^D(h) \approx 3\ cm^2/Vs$) and to reveal a detrimental type of electron trap in the middle of the gap for VHF-GD µc-Si:H.

ACKNOWLEDGEMENTS

I would like to thank:

Professor A. Shah who was the initiator of my research activity. He has offered me the unique occasion to realise the present thesis in his research group; his advices and comments greatly helped me in bringing this work to a good end. During all these years I especially appreciated his open mind and confidence, allowing me to propose and develop also my own ideas.

All my colleagues and friends from the "amorphous and microcrystalline silicon" group. By their constant encouragement and availability for help and discussions they have to a large extent contributed to this work.

The all other members of the IMT who have contributed in one or another way.

The Swiss National Science Foundation that enabled me to visit during one year the Physical Institute of the Academy of Sciences of the Czech Republic in Prague.

Dr. M. Vaněček and Dr. J. Kočka who accepted me for one year in their research groups. Their kind reception, their experience and competence in many fields as well as the friendly and creative atmosphere in their groups turned my stay in Prague into an unforgettable experience. A special "Díky" goes to Dr. M. Vaněček's students for all the good days I spent in their company.

Prof. H. Beck, Prof. Ph. Renaud, Prof. E. Schiff, Dr. M. Vaněček and Dr. B. Rech who have spontaneously accepted to join the examination board and who have devoted their time to the lecture of this thesis.

My parents for their unending support and interest in all my undertakings even though my research activities sometimes seemed to have little bearing with every days life.

My friend Peter who has lived with me through all the good and bad periods that came along with this thesis work and who believed in my projects also at moments when I was in doubt.

REFERENCES

[Amato 91] G. Amato, G. Benedetto, L. Boarino, M. Maringelli, R. Spagnolo, Appl. Phys. **A52**, 280 (1991).

[Amato 92] G. Amato, G. Boero, F. Fizzotti, C. Manfredotti, M. Abbas, Proc. 11th EC PVSEC, Montreux 1992, p. 730.

[Anderson 58] P. W. Anderson, Phys. Rev. **109**, 1492 (1958).

[Antoniadis 90] H. Antoniadis and E. A. Schiff, MRS Proc. **192**, p. 293 (1990).

[Basore 94] P. A. Basore, Prog. in Photovoltaics: Research and Applications **2**, 177 (1994).

[Bass 95] *Handbook of Optics*, vol. 1, ed. M. Bass, McGraw-Hill, New York 1995.

[Beck 92] N. Beck, N. Wyrsch, E. Sauvain, and A. Shah, Proceedings of the 11th ECPVSEC, Montreux 1992, p. 625.

[Beck 93] N. Beck, N. Wyrsch, E. Sauvain, and A. Shah, MRS Proc. **297**, p. 479 (1993).

[Beck 94] N. Beck, A. Shah, and N. Wyrsch, Proceedings of the 1st WCPEC, Hawaii 1994, p. 625.

[Beck 96-1] N. Beck, N. Wyrsch, Ch. Hof, and A. Shah, J. Appl. Phys. **79**, 9361 (1996).

[Beck 96-2] N. Beck, J. Meier, J. Fric, Z. Remeš, A. Poruba, R. Flückiger, J. Pohl, A. Shah, and M. Vaněček, J. Non-Cryst. Sol. **198-200** (1996) 903.

[Beck 96-3] N. Beck, P. Torres, J. Fric, Z. Remeš, A. Poruba, Ha Stuchlíková, A. Fejfar, N. Wyrsch, M. Vaněček, J. Kočka, and A. Shah, MRS Proc. **452**, p. 761 (1996).

[Brandt 91] M. S. Brandt and M. Stutzmann, J. Non-Cryst. Solids **137&138**, 211 (1991).

[Chittik 69] R. C. Chittik, J. H. Alexander, and H. F. Sterling, J. Electrochemical Soc. **116**, 77 (1969).

[Cody 92] G. D. Cody, J. Non-Cryst. Solids **141**, 3 (1992).

[Crandall 84] R. S. Crandall, in *Semiconductors and Semimetals*, Vol. 21, *Hydrogenated Amorphous Silicon*, Part B, edited by J. I. Pankove, Academic Press (1984) p. 245.

[Crandall 91] R. S. Crandall and I. Balberg, Appl. Phys. Lett. **58**, 508 (1991).

[Curtins 87] H. Curtins, N. Wyrsch, M. Favre, and A. Shah, Plasma Chem. & Plasma Proc. **7**, 267 (1987).

[Deyan He 94] Deyan He, N. Okada, Ch. M. Fortmann, I. Shimizu, J. Appl. Phys. **76**, 4728 (1994).

[Dubois 92] J. M. Dubois, G. Willeke, K. Prasad, O. Blenk, A. Shah, and E. Bucher, Proc. of the 11th ECPVSEC, Montreux 1992, p. 718.

[Fahrenbruch 83] A. L. Fahrenbruch, R. H. Bube, *Fundamentals of Solar Cells* (Academic Press, New York, 1983), p. 335.

[Faraji 92] M. Faraji, S. Gokhale, S. M. Choudhari, M. G. Takwale, and S. V. Ghaisas, Appl. Phys. Lett. **60**, 3289 (1992).

[Favre 89] M. Favre, H. Curtins, and M. Vaněček, J. Non-Cryst. Sol. **114**, 405 (1989).

[Filínski 72] I. Filínski, phys. stat. sol. (b) 49, 577 (1972).

[Finger 94] F. Finger, P. Hapke, M. Luysberg, R. Carius, H. Wagner, Appl. Phys. Lett. **65**, 2588 (1994).

[Flückiger 92] R. Flückiger, J. Meier, H. Keppner, U. Kroll, A. Shah, O. Greim, M. Morris, J. Pohl, P. Hapke, and R. Carius, Proc. of 11th ECPVSEC, Montreux 1992, p. 617.

[Flückiger 93] R. Flückiger, J. Meier, H. Keppner, M. Götz, and A. Shah, Proc. of 23rd IEEE PVSEC 1993, p. 839.

[Flückiger 95] R.and A. Shah, J. Appl. Phys. **77**, 712 (1995).

[Goerlitzer 95] M. Goerlitzer, P. Pipoz, H. Beck, N. Wyrsch, and A. Shah, MRS Proc. **377**, p. 503 (1995).

[Goerlitzer 96] M. Goerlitzer, N. Beck, P. Torres, N. Wyrsch, A. Shah, J. Appl. Phys. **80**, 5111 (1996).

[Goerlitzer 97] M. Goerlitzer, N. Beck, P. Torres, U. Kroll, H. Keppner, J. Meier, J. Koehler, N. Wyrsch, and A. Shah, MRS Proc. (1997), to be published.

[Green 82] M. A. Green, *Solar Cells* (published by the University of New South Wales, Kensington, Australia, 1982), p. 122.

[Green 95] M. A. Green, M. J. Keevers, Prog. in Photovoltaics: Research and Applications **3** (1995) 189.

[Günes 94] M. Günes, R. W. Collins, and C.R. Wronski, MRS Proc. **336**, 413 (1994).

[Hapke 96] P. Hapke, U. Backenhausen, R. Carius, F. Finger, and S. Ray, MRS Proc. (1994), to be published.

[Hattori 91] K. Hattori, Y. Niwano, H. Okamoto, and Y. Hamakawa, J. Non-Cryst. Solids **137&138**, 363 (1991).

[Hecht 32] K. Hecht, Z. Phys. **77**, 235 (1932).

[Heintze 96] M. Heintze, R. Zedlitz, J. Non-Cryst. Sol. **198-200**, 1038 (1996).

[Hubin 92] J. Hubin, A. Shah, and E. Sauvain, Philos. Mag. Lett. **66**, 115 (1992).

[Iqbal 83] Z. Iqbal, F.-A. Sarott, and S. Veprek, J. Phys. C **16**, 2005 (1983).

[Jackson 82-1] W. B. Jackson, Solid State Commun. 44, 477 (1982).

[Jackson 82-2] W. B. Jackson, N. M. Amer, Phys. Rev. **B25**, 5559 (1982).

[Jackson 83] W. B. Jackson, N. M. Johnson, and D. K. Biegelsen, Appl. Phys. Lett. **43** (1983) 195.

[Karg 86] F. H. Karg, W. Krühler, M. Möller, and K. v. Klitzing, J. Appl. Phys. **60**, 2016 (1986).

[Keppner 96] H. Keppner et al., MRS Proc. **452**, p. 865 (1996).

[Kočka 91-1] J. Kočka, O. Klíma, J. Juška, M. Hoheisel, and R. Plättner, J. Non-Cryst. Solids **137&138**, 427 (1991).

[Kočka 91-2] J. Kočka, C. E. Nebel, and C. D. Abel, Phil. Mag. **B 63**, 221 (1991).

[Kočka 94] J. Kočka, M. Vaněček, P. Macháček, A. Fejfar, E. Šípek, Ho-The-Ha, I. Pelant, J. Fric, J. Rosa, Z. Remeš, A. Poruba, M. Konagai, and W. Kusian, Proc. of the 1st WCPVEC, Hawaii, p. 437 (1994).

[Kondo 96] M. Kondo, Y. Toyoshima, A. Matsuda, and K. Ikuta, J. Appl. Phys. **80**, 6061 (1996).

[Konuma 87] M. Konuma, H. Curtins, F.-A. Sarott, and S. Veprek, Phil. Mag. **B 55**, 377 (1987).

[Kroll 96] U. Kroll, J. Meier, A. Shah, S. Mikhailov, and J. Weber, J. Appl. Phys. **80** (1996) 4971.

[Lechner 89] P. Lechner, H. Rübel, and N. Kniffler, Proceedings of the 10th ECPVSEC, Lisbon 1989, p. 354.

[LeComber 70] P. G. LeComber and W. E. Spear, Phys. Rev. Lett. **25**, 509 (1970).

[LeComber 83] P. G. LeComber, G. Willeke, and W. E. Spear, J. of Non-Cryst. Solids **59&60**, 795 (1983).

[Li 93] Y.-M. Li, MRS Proc. **297**, p. 803 (1993).

[Liu 93] H. N. Liu, Y. L. He, F. Wang, S. Grebner, J. Non-Cryst. Sol. **164-166**, 1005 (1993).

[Lucovsky 93] G. Lucovsky, C. Wang, M. J. Williams, Y. L. Chen, and D. M. Maher, MRS Proc. **283**, p. 443 (1993).

[Mackenzie 87] K. D. Mackenzie and W. Paul, MRS Proc. **149**, 281 (1987).

[Meier 94] J. Meier, S. Dubail, R. Flückiger, D. Fischer, H. Keppner, and S. Shah, Proc. of the 1st WCPVEC, Hawaii 1994, p. 405.

[Meier 96] J. Meier, P. Torres, R. Platz, S. Dubail, U. Kroll, J. A. Anna Selvan, N. Pellaton Vaucher, Ch. Hof, D. Fischer, H. Keppner, A. Shah, K.-D. Ufert, P. Giannoulès, and J. Koehler, MRS Proc. **420**, p. 3 (1996).

[Mettler 94] A. Mettler, N. Wyrsch, M. Goetz, and A. Shah, Sol. Energy Mater. Sol. Cells **34**, 533 (1994).

[Middya 96] A. R. Middya, J. Guillet, J. E. Bouree, and J. Perrin, Sol. State. Phenom. **51-52**, 255 (1996).

[Möller 93] H. J. Möller, *Semiconductors for Solar Cells* (Artech House Inc, 1993), ISBN 0-89006-574-8.

[Mott 79] N. F. Mott and E. A. Davis, *Electronic Processes in Non-Crystalline Materials* (Oxford University Press, 1979).

[Nonomura 94] S. Nonomura, T. Nishiwaki, and S. Nitta, Phil. Mag. **B 69** (1994) 335.

[Orenstein 81] H. Orenstein and M. A. Kastner, Phys. Rev. Lett. **46**, 1421 (1981).

[Overhof 89] H. Overhof and P. *Thomas, Electric Transport in hydrogenated amorphous Semiconductors* (Springer Verlag, Berlin, 1989), p. 41.

[Overhof 96] H. Overhof and M. Otte, Proc. of Int. Symp. on Cond. Matter Physics (ISCMP '96), Varna (1996) in press.

[Paul 61] W. Paul, J. Appl. Phys. **32**, 2082 (1961).

[Pipoz 95] P. Pipoz, thèse de doctorat, Université de Neuchâtel (1995), ISBN 2-9510115-0-4.

[Podbielski 84] R. Podbielski, and H. J. Möller, *Poly-Micro-Crystalline and Amorphous Semiconductors* , edited by P. Pinard and S. Kalbitzer (les éditions de Physique, Les Ulis Cedex, France, 1984), p. 365.

[Poruba 97] A. Poruba, Z. Remeš, J. Fric, M. Vanecek, J. Meier, P. Torres, N. Beck, N. Wyrsch, and A. Shah, to be published in the Proceedings of the 14th ECPVSEC (Barcelona, 1997).

[Prasad 91] K. Prasad, U. Kroll, F. Finger, A. Shah, J.-L- Dorier, A. Howling, J. Baumann, and M. Schubert, MRS Proc. **219**, 469 (1991).

[Ritter 86] D. Ritter, E. Zeldov, and K. Weiser, Appl. Phys. Lett. **49**, 791 (1986)

[Ritter 87] D. Ritter, K. Weiser, and E. Zeldov, J. Appl. Phys. **62**, 4563 (1987).

[Ritter 88] D. Ritter, E. Zeldov, and K. Weiser, Phys. Rev. **B 38**, 8296 (1988).

[Rose 63] A. Rose, *Concepts in photoconductivity and allied problems* (Interscience Publishers, John Wiley & Sons, 1963).

[Sagnes 93] I. Sagnes, A. Halimaoui, G. Vincent, and P. A. Badoz, Appl. Phys. Lett. **62**, 1155 (1993).

[Saritas 87] M. Saritas and H. D. McKell, J. Appl. Phys. **61**, 4923 (1987).

[Sauvain 92] E. Sauvain, thèse de doctorat, Université de Neuchâtel (1992).

[Schiff 86] E. A. Schiff, Phil. Mag. Lett. **55**, 87 (1987).

[Schropp 93] R. E. I. Schropp, A. Sluiter, M. B. von der Linden, and J. Daey Ouwens, J. Non-Cryst. Solids **164-166**, 709 (1993).

[Seto 75] J. Y. W. Seto, J. Appl. Phys. **46**, 5247 (1975).

[Seynhave 89] G. F. Seynhave, R. P. Barclay, G. J. Adraenssens, and J. M. Marshall, Phys. Rev. **B 39**, 10196 (1989).

[Shah 96] A. Shah, J. Hubin, R. Platz, M. Goerlitzer, and N. Wyrsch, J. Non-Cryst. Solids **198-200**, 548 (1996).

[Shah 97] A. Shah, E. Sauvain, J. Hubin, P. Pipoz, and C. Hof, Phil. Mag. **B 75**, 925 (1997).

[Spear 69] W. E. Spear, J. Non-Cryst. Solids **1**, 197 (1969).

[Spear 75] W. E. Spear and P. G. LeComber, Solid State Commun. **17**, 1193 (1975).

[Staebler 77] D. L. Staebler and C. Wronski, Appl. Phys. Lett. **31**, 292 (1977).

[Street 82] R. A. Street, Appl. Phys. Lett. **41**, 1060 (1982).

[Street 83] R. A. Street, J. Zesch, and M. J. Thompson, Appl. Phys. Lett. **43**, 672 (1983).

[Street 91] R. A. Street, *Hydrogenated Amorphous Silicon* (Cambridge University Press, Cambridge, 1991), pp. 136 and 147.

[Stutzmann 87] M. Stutzmann, D. K. Biegelsen, and R. A. Street, Phys. Rev. **B 35**, 5666 (1987).

[Swanepoel 83] R. Swanepoel, J. Phys. **E 16**, 1214 (1983).

[Swanepoel 84] R. Swanepoel, J. Phys. **E 17**, 896 (1984).

[Sze 85] S. M. Sze, in *Semiconductor Devices - Physics and Technology* (John Wiley & Sons, New York, 1985).

[Taylor 72] G. W. Taylor and J. G. Simmons, J. Non-Cryst. Solids **B 10, 940 (1972).**

[Tiedje 81] T. Tiedje and A. Rose, Solid State Comm. **37**, 48 (1981).

[Tiedje 84] T. Tiedje, in: *Semiconductors and Semimetals*, Vol. 21, Part B (Academic Press Inc.,Orlando, USA, 1984), p. 207.

[Torres 95] P. Torres, R. Flückiger, J. Meier, U. Kroll, V. Shklover, and A. Shah, Proc. of the 13th EC-PVSEC, Nice 1995, p. 1638.

[Torres 96] P. Torres, J. Meier, R. Flückiger, U. Kroll, J. A. Anna Selvan, H. Keppner, A. Shah, S. D. Littlewood, I. E. Kelly, and P. Giannoulès, Appl. Phys. Lett. **69** (1996) 1373.

[Torres 97] P. Torres, J. Meier, U. Kroll, N. Beck, H. Keppner, A. Shah, to be published in the Proc. of 26th IEEE PVSEC 1997.

[Tserbak 95] C. Tserbak and G. Theodorou, Phys. Rev. **B 52**, 12'232 (1995).

[Usui 79] S. Usui and M. Kikuchi, J. Non-Cryst. Sol. **34**, 1 (1979).

[Vaillant 86] F. Vaillant and D. Jousse, Phys. Rev. B **34**, 4088 (1986).

[VandeHulst 57] H. C. Van de Hulst, *Light Scattering by Small Particles* (Wiley, New York, 1957).

[Vaněček 81] M. Vaněček, J. Kočka, J. Stuchlík, and A. Tříska, Sol. State. Commun. 39 (1981) 1199.

[Vaněček 90] M. Vaněček, D. Červinka, M. Favre, H. Curtins, and A. Shah, MRS Proc. 192, p. 639 (1990).

[Vaněček 95] M. Vaněček, J. Kočka, A. Poruba, A. Fejfar, J. Appl. Phys. **78** (1995) 6203.

[Vaněček 97] M. Vaněček, A. Poruba, Z. Remeš, N. Beck, M. Nesládek, to be published in the J. Non-Cryst. Solids.

[Vepřek 68] S. Vepřek, V. Mareček, Solid State Elec. **11**, 683 (1968).

[Vepřek 83] S. Vepřek, Z. Iqbal, R. O. Kühne, P. Capezzuto, F.-A. Sarrott, and J. K. Gimzewski, J. Phys. C: Solid State Phys. **16**, 6341 (1983).

[Wang 90] C. Wang and G. Lucovsky, Proc. of the 21st IEEE PVSC, Kissimee 1990, p. 1614.

[Wronski 93] C. Wronski, R. M. Dawson, M. Gunes, Y. M. Li, and R. W. Collins, MRS Proc. **297**, p. 443 (1993).

[Wyrsch 91-1] N. Wyrsch and A. Shah, Solid State Commun. **80**, 807 (1991).

[Wyrsch 91-2] N. Wyrsch and A. Shah, J. Non-Cryst. Solids **137&138**, **431** (1991).

[Wyrsch 92] N. Wyrsch, thèse de doctorat, Université de Neuchâtel (1992).

[Yang 89] L. Yang, A. Catalano, R. R. Arya, M. S. Bennett, and I. Balberg, MRS Proc. **149**, p. 563 (1989).

[Yang 94] J. Yang, X. Xu, and S. Guha, MRS Proc. **336**, p. 687 (1994).

[Zapletal 94] J. Zapletal, A. Fejfar, S. Fouad Abdel Hamied, E Šípek, I. Pelant, J. Kočka, G. Juška, T. Yokoi, M. Azuma, I. Shimizu, H. Mahan, and R. S. Crandall, Proceedings of the 12th ECPVSEC, Amsterdam 1994, p. 104.

[Zhou 92] J. H. Zhou and S. R. Elliott, Philos. Mag. **B 66**, 801 (1992).

[Zhou 94] J. H. Zhou and S. R. Elliott, Philos. Mag. **B 69**, 147 (1994).

[Zhu 86] M. Zhu and H. Fritzsche, Phil. Mag. **B 53**, 41 (1986).

Aktuelle in unserer Reihe erschienene Physiktitel

Band 306: Runge, Bernd-Uwe »Struktur und Magnetismus von Ag-Filmen an der Grenzfläche zu Fe(100)«
ISBN 3-930803-05-4, 74 Seiten, DM 74,–

Band 307: Steinke, Rainer »Beobachtung von UV-induzierten Vorgängen an Polymer/Metallgrenzflächen«
ISBN 3-930803-06-2, 112 Seiten, DM 80,–

Band 309: Sappelt, Dirk »Spinodale Entmischung mit glasiger Erstarrung einer Phase«
ISBN 3-930803-08-9, 162 Seiten, DM 85,–

Band 310: Müller-Seydlitz, Tim »Ultrakalte Argonatome in optischen Gittern«
ISBN 3-930803-09-7, 144 Seiten, DM 80,–

Band 311: Jacobs, Karin »Stabilität und Dynamik flüssiger Polymerfilme«
ISBN 3-930803-10-0, 80 Seiten, DM 80,–

Band 313: Bischof, Jörg »Metallische Dünnfilmschmelzen nach Pulslaser-Bestrahlung: Phasenumwandlungen und Instabilitäten«
ISBN 3-930803-12-7, 162 Seiten, DM 85,–

Band 314: Feß, Karsten »Neue thermoelektrische Materialien: Untersuchungen an Halbleitern und unkonventionellen Materialsystemen«
ISBN 3-930803-13-5, 124 Seiten, DM 89,–

Band 315: Kurtsiefer, Christian »Atomoptische Experimente zu nichtklassischen Zuständen der Bewegung von metastabilen Edelgasatomen und Atom-Photon-Paaren«
ISBN 3-930803-14-3, 168 Seiten, DM 89,–

Band 316: Mugele, Frieder »Stufenfluktuationen auf Ag(111): Zur Problematik des Spitzeneinflusses bei dynamischen Untersuchungen mit dem Rastertunnelmikroskop«
ISBN 3-930803-15-1, 122 Seiten, DM 86,–

Band 317: Henschel, Roderich »Eigenschaften von SIPOS und Optimierung damit hergestellter Siliziumsolarzellen«
ISBN 3-930803-16-X, 164 Seiten, DM 79,–

Band 318: Peter, Kristian »Schnell wachsende kristalline Silizium-Dünnfilme: Untersuchungen unter Verwendung der Flüssigphasenepitaxie (LPE)«
ISBN 3-930803-17-8, 114 Seiten, DM 79,–

Band 319: Conradt, Robert N. J. »Wasserstoffilme unterhalb des Tripelpunktes«
ISBN 3-930803-18-6, 148 Seiten, DM 78,–

Band 320: Drodofsky, Ulrich »Atom-Lithographie mit Lichtkräften«
ISBN 3-930803-19-4, 136 Seiten, DM 85,–

Band 324: Kohl, Udo »Wachstum, Struktur und Magnetismus dünner Kupfer-Filme auf Kobalt (100)-Oberflächen«
ISBN 3-930803-23-2, 88 Seiten, DM 80,–

Band 325: Häring, Jochen »Schwachstellen in epitaktischen $Y_1Ba_2Cu_3O_7$-Dünnschichten infolge mittelenergetischer Ionen- und Elektronenbestrahlung«
ISBN 3-930803-24-0, 144 Seiten, DM 89,–

Band 326: Fischer, Hans Peter »Zur Theorie der spinodalen Entmischung: Wandeffekte und Ordnungsbildung«
ISBN 3-930803-25-9, 122 Seiten, DM 98,–

UFO Atelier für Gestaltung & Verlag · E.-Mühlenweg-Str. 12 · 78476 Allensbach